Step-edge Josephson Junctions and High Temperature Superconducting Quantum Interference Device (SQUID) Gradiometers

Thesis submitted for the degree of Doctor of Philosophy in the University of Strathclyde, Glasgow, Scotland

Alasdair J. Millar, BSc.

Department of Physics and Applied Physics
University of Strathclyde

Submitted November 2001

Abstract

This thesis is concerned with the development of Superconducting Quantum Interference Device (SQUID) gradiometers based on the high temperature superconductor $YBa_2Cu_3O_{7-\delta}$ (YBCO). A step-edge Josephson junction fabrication process was developed to produce sufficiently steep ($> 60°$) step-edges such that junctions exhibited RSJ-like current-voltage characteristics. The mean $I_C R_N$ product of a sample of twenty step-edge junctions was $130\mu V$. Step-edge dc SQUIDs with inductances between 67pH and 114pH were fabricated. Generally the SQUIDs had an intrinsic white flux noise in the 10-30$\mu\Phi_0/\sqrt{Hz}$ range, with the best device, a 70pH SQUID, exhibiting a white flux noise of $5\mu\Phi_0/\sqrt{Hz}$. Different first-order SQUID gradiometer designs were fabricated from single layers of YBCO. Two single-layer gradiometer (SLG) designs were fabricated on $10 \times 10mm^2$ substrates. The best balance and lowest gradient sensitivity measured for these devices were 1/300 and $308fT/cm\sqrt{Hz}$ (at 1kHz) respectively. The larger baseline and larger flux capture area of the pick-up loops in a large area SLG design, fabricated on $30 \times 10mm^2$ substrates, resulted in significant improvements in the balance and gradient sensitivity with 1/1000 and $50fT/cm\sqrt{Hz}$ (at 1kHz) measured respectively. To reduce the uniform field effective area of SLGs and therefore reduce the direct pick-up of environmental field noise when operated unshielded, a novel gradiometric SQUID (G-SQUID) device was developed. Fabricated from a single layer of YBCO, the G-SQUIDs, with inductances of 67pH, had small uniform field effective areas of approximately $2\mu m^2$ - more than two orders of magnitude smaller than the uniform field effective areas of conventional narrow-linewidth SQUIDs of similar inductance. Two designs of G-SQUID SLGs were fabricated on $10 \times 10mm^2$ substrates. Due to their small effective areas, when cooled unshielded these devices showed no increase in their white flux noise. The best balance achieved for a G-SQUID SLG was approximately 1/5000 - an order of magnitude better than the balance of similar SLGs incorporating conventional narrow-linewidth SQUIDs.

Acknowledgements

I would like to thank Colin Pegrum who supervised this work, for his continuous encouragement, practical advice and for providing the resources that I needed for my research.

Ed Romans and Chris Carr have become good friends as well as providing considerable practical assistance. Thanks to Ed for growing the YBCO thin films, fabricating many of the bicrystal devices and for all the discussions related to ideas that were important to this work. Thanks to Chris for teaching me how to use the device characterisation equipment and for helping me test many devices.

Thanks to Alex Eulenburg for getting me started by suggesting I try and make some step-edges. I also acknowledge Alex for the design of the large area gradiometers.

I have had the pleasure of working with a great group of people over the past three years. Thanks to those mentioned above and to Pete, John, Gordon Donaldson, Ronnie, Derek, Emilio, Paul, Ratnakar, Gordon Henrici, Dave, Pedro, Uma, Neil and Alexey for making tea breaks, lunches, nights out and weekends away so enjoyable.

Thanks to all at CSIRO, Sydney, Australia, who made me feel so welcome during the month I spent there. Special thanks to Cathy Foley who assisted with the electron microscopy work.

Finally, a special thank you to my parents, who have given me continuous support and guidance. Mum and Dad I am forever grateful.

List of Symbols

The following symbols are used throughout this thesis. Other symbols have been used occasionally and are introduced as needed.

β_L	Reduced SQUID inductance
ΔV	Maximum peak-to-peak voltage modulation
Γ	Junction noise parameter
λ_L	London magnetic penetration depth
Φ	Magnetic flux
Φ_0	Magnetic flux quantum
A_{MAG}	Uniform field effective area of one gradiometer pick-up loop
A_{PAR}	Parasitic uniform field effective area
A_{SQ}	SQUID uniform field effective area
A_{LP}	Effective sensing area of a pick-up loop
b	Gradiometer balance
B	Magnetic field
f	Frequency
h	Step-edge height
I_C	Junction critical current
J_C	Junction critical current density
l	Gradiometer baseline
L_{LP}	Pick-up loop inductance
L_M	Mutual inductance coupling SQUID to pick-up loops
L_{SQ}	SQUID inductance
R_N	Junction normal state resistance
S_Φ	Flux spectral density

S_B Field spectral density

S_G Field gradient spectral density

t $YBa_2Cu_3O_{7-\delta}$ film thickness

T_C Critical temperature

V_Φ Flux to voltage transfer function at its steepest point

List of Acronyms

The following acronyms are used throughout this thesis. Other acronyms have been used occasionally and are introduced as needed.

ac	Alternating current
AFM	Atomic force microscopy
dc	Direct current
DCM	Directly coupled magnetometer
FLL	Flux-locked loop
GBJ	Grain boundary junction
G-SQUID	Gradiometric superconducting quantum interference device
HTS	High temperature superconductivity/superconductor
ICM	Inductively coupled magnetometer
I-V	Current vs. voltage
LTS	Low temperature superconductivity/superconductor
MCG	Magnetocardiography/magnetocardiogram
NDE	Non-destructive evaluation
PCB	Printed circuit board
PLD	Pulsed laser deposition
RSJ	Resistively shunted junction
SEM	Scanning electron microscopy
SLG	Single-layer gradiometer
SQUID	Superconducting quantum interference device
STO	$SrTiO_3$
UV	Ultraviolet
V-Φ	Voltage vs. flux
YBCO	$YBa_2Cu_3O_{7-\delta}$

Contents

Chapter 1

Introduction

The Superconducting Quantum Interference Device (SQUID) has been studied and applied as a sensor for 35 years - the first low temperature superconductor (LTS) SQUIDs, operating at 4.2K (the boiling point of liquid helium) were developed in the mid-1960's [1, 2, 3]. SQUIDs offer unrivaled magnetic flux sensitivity over a wide frequency range (from dc to GHz), and great versatility, capable of measuring any physical quantity that can be converted into a magnetic flux - examples include current, voltage, magnetic field or field gradient, gravitational field and magnetic susceptibility. The intensity of the research increased significantly in early 1987 after the discovery of superconductivity in ceramic oxides [4] such as $YBa_2Cu_3O_{7-\delta}$ (YBCO) [5] with a superconducting transition temperature T_C above 77.4K (the boiling point of liquid nitrogen). The prospect of high temperature superconductor (HTS) ceramic compound SQUIDs offering the performance levels of the LTS SQUIDs, without the need for liquid helium, offered great potential for commercial application in medical and engineering fields (see for example [6] and [7]). The main advantages over the LTS technology being that liquid nitrogen is more abundant and much cheaper than liquid helium, and that liquid nitrogen has a much slower boil off, for a given heat load, than liquid helium. Alternatively there is the option to cool HTS devices without the need for any liquid coolant by using a cyro-cooler [8], making SQUID sensors more easily portable and user friendly for potential commercial application.

With any sensor, three key criteria must be met if the device is to be successful in an application: (1) it must have adequate sensitivity to detect the signal to be measured; (2) it must have sufficient selectivity to discriminate against unwanted signals; and (3) it must have the stability to operate reliably over a sufficient period

of time in the environment in which the signal is to be measured. After nearly fifteen years of research, many of the challenges that faced HTS SQUIDs in meeting the first of these criteria have been overcome; more recently the challenges have been in meeting the latter two of the above requirements. The work presented in this thesis represents a small contribution in the worldwide effort to develop HTS SQUIDs.

The operation of the SQUID is based on two physical phenomena inherent to superconducting materials: flux quantisation and Josephson tunneling. The remainder of this chapter provides a background to the necessary theory to understand SQUIDs, their operation and their optimisation.

1.1 Superconductivity

Superconductivity, a phenomenon found in a wide range of materials, from metals to organic compounds, is characterised macroscopically by two physical phenomena which occur below the superconducting transition temperature T_C: (1) the loss of electrical resistance to dc current flow; and (2) the expulsion of magnetic flux from the body of the superconductor (the Meissner effect). The absence of electrical resistivity has been established within the limits of experimental detection from the lack of current decay in a superconducting loop. The Meissner effect occurs in all superconductors, though perfect flux exclusion will only occur in bulk samples satisfying the condition that the length of the sample parallel to the field is much greater than the other dimensions of the sample. In the presence of an external magnetic flux, circulating supercurrents flow within a depth λ_L of the surface of the superconductor generating a flux that opposes the external flux - λ_L is known as the London magnetic penetration depth. The net effect is the expulsion of magnetic flux from the bulk of the superconductor.

As a superconductor is cooled below its transition temperature, the electrons form Cooper pairs (Bosons) and condense into a single quantum mechanical state with each pair having the same phase and momentum - a single wavefunction

$\Psi(r) = |\Psi|e^{i\phi(r)}$ (where ϕ is the phase) represents the system of Cooper pair charge carriers with each pair exhibiting coherence over a distance ξ, the coherence length. The phase is constant for all the superconducting electron pairs provided there is no current flowing through the superconductor and there is no external magnetic flux, Φ. However when there is a current flowing or Φ is non-zero the phase between two points in the superconductor becomes in general non-zero.

1.1.1 Flux quantisation

SQUIDs combine two physical phenomena, Josephson tunneling (discussed below in Section 1.2) and flux quantisation. If one considers a closed loop of superconducting material enclosing a non-superconducting region, and that the wavefunction describing the Cooper pairs in the superconductor must be single valued, it is clear that the net change in phase on going once round the loop on any path must be zero or a multiple of 2π. For this condition to be satisfied in the presence of an applied magnetic flux, the screening currents, generated to depth λ_L in the loop, must act such that the flux threading the superconducting loop Φ is quantised where

$$\Phi = n\Phi_0, \tag{1.1}$$

where n is an integer and $\Phi_0 = h/2e = 2.07 \times 10^{-15}$Wb is the flux quantum. The property of flux quantisation was first demonstrated experimentally in 1961 [9, 10].

1.2 Josephson Junctions

1.2.1 The Josephson effects

The active element of the SQUID, the Josephson junction [11], consists of two weakly coupled superconducting electrodes, in practice realised by separating the two superconductors by a thin barrier. The barrier is typically formed from a normal conductor or an insulator, and in HTS also by a grain boundary in the ceramic.

Provided there is sufficient coupling between the two electrodes (*i.e.* there is sufficient overlap of the wavefunctions describing the superconducting state in each electrode), superconducting electron pairs can tunnel through the weak link barrier without energy loss up to the maximum supercurrent the junction can sustain - the critical current I_C. On tunneling through the barrier the wavefunction of the superconducting electron pairs undergoes a phase change δ that is dependent on the magnitude of the current flow I through the junction. This is known as the dc Josephson effect, represented by the following equation

$$I = I_C \sin\delta. \tag{1.2}$$

When the bias current is increased above I_C a voltage appears across the junction and δ varies with time as

$$\frac{d\delta}{dt} = \frac{2\pi V}{\Phi_0}, \tag{1.3}$$

where V is the time averaged voltage across the junctions and Φ_0 is the flux quantum. From Equations 1.2 and 1.3 it is clear that in the voltage state there is a current oscillating through the junction with a Josephson frequency of $\omega_J = 2\pi V/\Phi_0$. This is known as the ac Josephson effect.

1.2.2 The RSJ model

A typical LTS Josephson junction has hysteretic current-voltage (I-V) characteristics - the voltage across the junction switches abruptly to a non-zero state as the direct current bias is increased above I_C but returns to zero only when the bias is decreased well below I_C. For most practical applications, a shunt resistance R_N is connected in parallel with the LTS junction to suppress this hysteresis. The resistively shunted junction (RSJ) model which describes the characteristics of this shunted junction, was independently suggested by Stewart [12] and McCumber [13] and is shown schematically in Figure 1.1(a). The ideal junction element has a critical current I_C and is in parallel with the elements representing the junction's

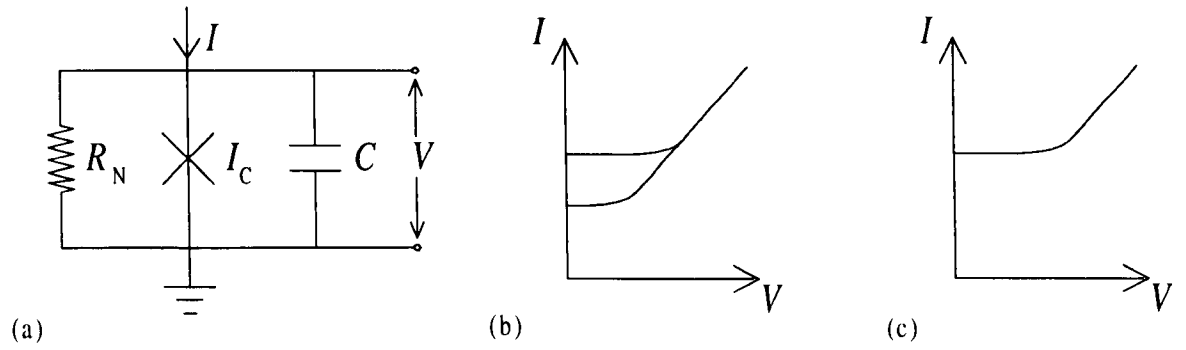

Figure 1.1: (a) The equivalent circuit of a resistively shunted Josephson junction. (b) Hysteretic and (c) non-hysteretic junction I-V characteristics.

self-capacitance C and the shunt resistance R_{N}. The current flow I through the circuit is given by

$$I = I_{\mathrm{C}}\sin\delta + \frac{V}{R_{\mathrm{N}}} + C\frac{\mathrm{d}V}{\mathrm{d}t}. \tag{1.4}$$

Using Equation 1.3 and the normalisation parameters $\tau = t(2\pi I_{\mathrm{C}}R_{\mathrm{N}}/\Phi_0)$ and $i = I/I_{\mathrm{C}}$ Equation 1.4 can be written as

$$i = \sin\delta + \frac{\mathrm{d}\delta}{\mathrm{d}\tau} + \beta_C\frac{\mathrm{d}^2\delta}{\mathrm{d}\tau^2}, \tag{1.5}$$

where β_C is the McCumber parameter given by

$$\beta_C = \frac{2\pi I_{\mathrm{C}}{R_{\mathrm{N}}}^2 C}{\Phi_0}. \tag{1.6}$$

For $\beta_C > 1$ the junction I-V characteristics will be hysteretic as shown in Figure 1.1(b), while for values of $\beta_C \leq 1$ this hysteresis is suppressed. In the limit of $\beta_C = 0$ Equation 1.5 can be solved exactly yielding $V = 0$ for $I < I_{\mathrm{C}}$, and

$$V = R_{\mathrm{N}}\sqrt{I^2 - {I_{\mathrm{C}}}^2}, \tag{1.7}$$

for $I > I_{\mathrm{C}}$ as shown schematically in Figure 1.1(c). HTS Josephson junctions are generally intrinsically shunted with β_C small enough such that the I-V characteristics are non-hysteretic - except at operating temperatures well below T_{C} where I_{C}

becomes large enough to obtain $\beta_C > 1$.

It should be noted that Equation 1.7 describes the ideal case where $\beta_C = 0$ and $T = 0$K. Operation at non-zero temperatures leads to significant noise rounding of the I-V curve due to Nyquist current noise originating in the shunt resistors. The influence of this thermal $k_B T$ noise (where k_B is Boltzmann's constant) is expressed by the noise parameter Γ:

$$\Gamma = \frac{2\pi k_B T}{I_C \Phi_0}, \tag{1.8}$$

where $I_C \Phi_0 / 2\pi$ is the Josephson coupling energy. At 77.4K the thermal energy becomes comparable with the Josephson coupling energy for junctions with $I_C \sim 3.3\mu$A. Simulations have shown [14] that for $\Gamma > 0.2$ the wavefunctions on either side of the barrier become decoupled. At an operating temperature of 77.4K this translates to the requirement that $I_C > 16\mu$A.

1.2.3 Practical Josephson junctions

For SQUID applications resistively-shunted non-hysteretic Josephson junctions are required. In LTS, such junctions are typically realised using a trilayer superconductor-insulator-superconductor (SIS) technology such as Nb-Al-AlO_x-Nb where the surface of the Al is oxidised to a thickness of 2-3nm, before deposition of the upper Nb layer, to form the junction. Such tunnel junctions are hysteretic and need to be shunted by an external resistor connected in parallel to the junction. With HTS materials such a trilayer technology, with a barrier acting as the tunnel region, is difficult to implement. The ceramic nature of HTS materials makes it difficult to maintain suitable thin film stoichiometry during the growth of multiple layers. In addition the supercurrent transport properties of HTS materials are highly anisotropic resulting in a rapid decay of the superconducting wavefunction in c-axis barriers (*i.e.* the barriers formed in trilayers). To realise suitable HTS junctions many alternative techniques have been employed. These can be categorised into three types: grain boundary junctions, barrier junctions and weakened junctions.

As with all of the HTS junction technologies developed, those discussed below most commonly incorporate YBCO thin films.

The relatively small coherence length of the charge carriers in HTS materials results in grain boundaries between neighbouring cells in a polycrystalline lattice acting as Josephson weak links. The first HTS junctions were such grain boundary junctions (GBJs), fabricated in granular films by patterning a narrow track in the film across the naturally occurring grains [15]. The quality of thin films has improved greatly and today controlled techniques are used to induce artificial grain boundaries in the film which can be patterned to form GBJs. The two most common types of GBJ used are the bicrystal junction and the step-edge junction.

The bicrystal junction [16, 17], shown schematically in Figure 1.2(a), uses a bicrystal substrate formed by fusing two pieces of single crystal together to form a grain boundary. Typically the chosen misorientation angle at the grain boundary is 24°, 30° or 36.8°. This grain boundary propagates through into the c-axis superconducting film grown on the bicrystal substrate. The junction is formed by patterning the film that crosses the grain boundary into a narrow track. Studies have shown that the grain boundary formed in the HTS film is composed of facets which results in the misorientation angle of the grain boundary in the film varying along the bicrystal line [18, 19]. Despite this, the junction I_C and R_N do have some relation to the misorientation angle of the bicrystal substrate used, and I_C can be tuned to some degree by appropriately setting the thickness and width of the track that crosses the grain boundary. On individual bicrystal substrates the reproducibility of junction's parameters can be relatively high. The $I_C R_N$ values of bicrystal junctions typically compare well with those achieved using alternative HTS junction technologies - the product $I_C R_N$ is regarded as a figure of merit for the quality of the junction. On a single chip yields of RSJ-like junctions up to 100% [20] and $I_C R_N$ products as high as 250μV [21, 22] can be achieved. However the chip-to-chip reproducibility is generally poor - a consequence of the difficulties in manufacturing reproducible bicrystal substrates. Other disadvantages of the bicrystal technology

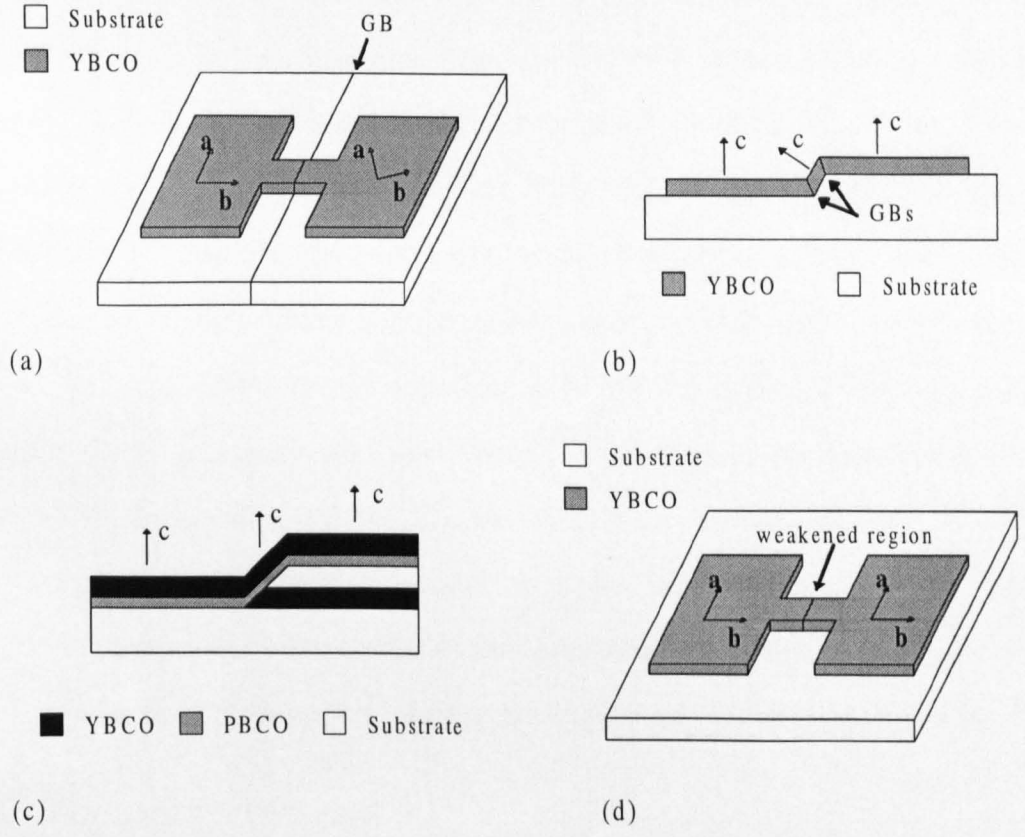

Figure 1.2: Schematic representations of various HTS Josephson junction technologies. (a) A bicrystal junction, with the axes showing the misorientation of the ab-planes either side of the grain boundary. (b) A side-view of a step-edge junction showing the orientation of the c-axis of the superconducting thin film and the associated grain boundaries. (c) A side-view of a ramp-edge junction where tunneling supercurrents flow through the non-superconducting (PBCO) region. Note that the c-axis growth of the upper electrode is normal to the plane of the substrate. (d) A weakened junction, formed by artificially damaging a patterned superconducting track.

are that the substrates are relatively expensive, and the device design is restricted, as all the junctions must be positioned along the straight line of the grain boundary in the substrate.

An alternative approach to fabricate a GBJ is the step-edge technology [23]. A step-edge junction, shown schematically in Figure 1.2(b), is formed by depositing an HTS thin film and patterning it into a narrow track over a step prepared on a single crystal substrate prior to film deposition. If the edge of the step has sufficient steepness, it is energetically favourable for the HTS film to grow with a different c-axis orientation on the sloping edge and typically two grain boundaries in series are formed, one at the top and one at the bottom edge of the step. Of the two

grain boundaries, the one with the lower I_C will dominate the junction's electrical characteristics - it is thus desirable that one of the boundaries has a significantly smaller critical current. The angle of the step, the ratio of the film thickness to the step height and the microstructure of the HTS film all strongly affect the junction properties I_C and R_N. Further discussion of the dependence of the junction properties on the step characteristics is given in Section 3.1.2. The single crystal substrates used for step-edge junctions are approximately five times cheaper (for $10 \times 10\text{mm}^2$ substrates) than bicrystals and also avoid the restrictions on junction placement associated with the bicrystal technology. A popular misconception is that reproducibility and $I_C R_N$ products are poorer for step-edges than bicrystals, however in Chapter 3 it will be demonstrated that this need not be the case, though establishing and maintaining a step-edge technology is considerably more labour intensive than using bicrystals.

Perhaps the most common technique used to fabricate HTS barrier type junctions is the ramp-edge technology [24]. Ramp-edge junctions are similar to LTS trilayer junctions in that a barrier material is used to form the weak link. However the ramp-edge technology avoids the problems associated with c-axis transport in trilayer junctions by allowing the tunneling supercurrent to flow in the ab-plane. Shown schematically in Figure 1.2(c), a ramp-type structure is formed by etching an epitaxial superconductor/insulator multilayer at a shallow angle to expose a region of the HTS film which forms the lower electrode of the junction. An epitaxial thin film tunnel barrier with a typical thickness of 5nm is deposited before deposition of a second superconducting film to form the upper electrode. The junction is then formed by patterning the multilayer structure into a narrow track. Typically YBCO will be used for the superconducting electrodes with materials such as $SrTiO_3$ and the normal conducting $PrBa_2Cu_3O_{7-\delta}$ (PBCO) used as the insulator and tunnel barrier respectively. To avoid grain boundaries in the upper superconducting electrode it is important that the etching of the superconductor/insulator layer results in a shallow angle of no more than 30°. This restriction results in an unavoidably

large contact area between the superconducting electrodes and the tunnel barrier. This combined with the low resistivities of all the normal conducting materials that grow epitaxially on YBCO (*e.g.* PBCO) results in junctions with small R_N values thus limiting the $I_C R_N$ products that can be achieved using the ramp-edge technology. Despite this ramp-edge junctions offer some promise for applications in magnetically unshielded environments with a distinct advantage over GBJs being that the top electrode shields the junction from perpendicular magnetic fields which can significantly perturb the junction critical current.

The final classification of HTS Josephson junctions are weakened junctions. A thin tunnel barrier is formed by artificially damaging a small region of the patterned narrow track in the HTS film, such that T_C in that region is suppressed (see Figure 1.2(d)). A highly focused beam is required to irradiate a sufficiently small region of the superconducting track to maintain sufficient coupling between the superconducting regions. Typically this is done using a focused ion-beam [25] or a beam of electrons [26]. While weakened junctions offer excellent junction reproducibility and freedom in junction placement, such techniques are not common practice due to the specialised and expensive equipment required.

1.3 dc SQUIDs

The devices described in this work are based on the dc SQUID which consists of two resistively shunted non-hysteretic Josephson junctions connected in parallel in a superconducting loop of inductance L, as shown schematically in Figure 1.3(a). Each junction has a critical current I_C, a shunt resistance R_N and a capacitance C. The magnetic flux threading the loop is no longer quantised as in the case of a closed superconducting ring. However an applied magnetic flux Φ alters the phase difference (δ_1 and δ_2) across each of the two junctions such that

$$\delta_1 - \delta_2 = 2\pi \frac{\Phi}{\Phi_0}. \tag{1.9}$$

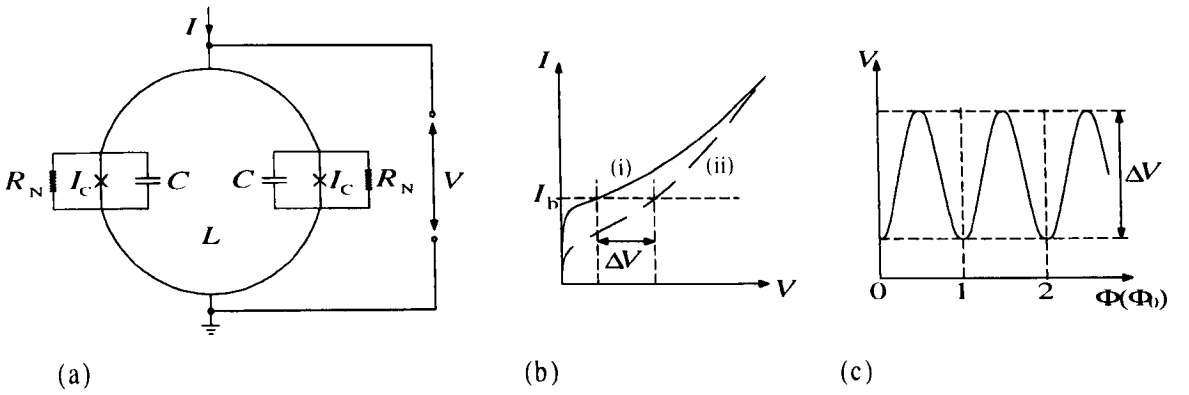

Figure 1.3: (a) Schematic of the dc SQUID. (b) The I-V characteristics of the dc SQUID for an applied flux of (i) $n\Phi_0$ and (ii) $(n + 1/2)\Phi_0$. (c) V-Φ characteristics when the SQUID is biased with current I_b.

From Equation 1.2 it follows that these phase changes, in turn, affect the maximum supercurrent that can flow through the two junctions of the SQUID. The maximum supercurrent that can flow through the SQUID (I_0) is thus a periodic function of the magnetic flux threading the loop given by:

$$I_0(\Phi) = 2I_C(0)\left|\cos\frac{\pi\Phi}{\Phi_0}\right|. \tag{1.10}$$

Equation 1.10 yields a maximum of $I_{0,max} = 2I_C$ for $\Phi = n\Phi_0$ and a minimum of $I_{0,min} = 0$ for $\Phi = (n+1/2)\Phi_0$. The dependence of the SQUID I-V characteristics on applied magnetic flux is shown in Figure 1.3(b). Note that when a flux of $(n+1/2)\Phi_0$ is applied the critical current is not fully suppressed to zero. This is a consequence of the current through the two junctions in the SQUID not being identical due to the additional circulating screening current $J = -\Phi/L$ induced in the loop by any applied flux $\Phi \neq n\Phi_0$. An expression for the critical current modulation depth $\Delta I_0 = I_{0,max} - I_{0,min}$ has been given by Tesche and Clarke [27]. For small values of Γ (< 0.2) they predict

$$\Delta I_0 = \frac{1}{1+\beta_L} I_{0,max}, \tag{1.11}$$

where β_L is the screening parameter given by

$$\beta_L = \frac{2I_C L}{\Phi_0}. \tag{1.12}$$

Hence we find that the modulation depth of I_0 decreases with increasing β_L.

As a consequence of the critical current modulation, the dc voltage across the SQUID, when biased with $I > 2I_C$, also has a periodical flux dependence as shown in Figure 1.3(c). In practice the bias current is adjusted to give the maximum peak-to-peak voltage modulation ΔV, which can be expressed as [28]

$$\Delta V = \frac{7}{\pi^2} \frac{I_C R_N}{1+\beta_L} \left(1 - 3.57 \frac{\sqrt{k_B T L}}{\Phi_0}\right). \tag{1.13}$$

1.3.1 The flux-locked loop

As can be seen from Figure 1.3(c), the output of the SQUID as a function of applied flux is non-linear. When operated in small-signal mode where the voltage across the SQUID is simply read as the output, the measurement is restricted to signals much smaller than a single flux quantum Φ_0. To increase the linearity, the SQUID is typically operated in a feedback loop mode called the flux-locked loop (FLL). Figure 1.4 is a schematic of the standard FLL readout scheme. Before locking the SQUID a bias current is applied such that the open loop transfer function of the SQUID $V_\Phi = |\partial V/\partial \Phi|$ is maximum. By applying a bias flux the operating point of the SQUID is then locked at a minimum in the V-Φ characteristics corresponding to $\Phi = n\Phi_0$. An additional high frequency modulating flux f_M (typically of order 100kHz) is applied as a square wave with a flux peak-to-peak amplitude of $\Phi_0/2$. The resulting ac voltage output across the SQUID is lock-in detected via a cooled step-up transformer and pre-amplifier. The lock-in signal, referenced to the modulation frequency, is integrated and fed-back through a resistor R_F to a feedback coil coupled to the SQUID with a mutual inductance M_F. Note that the feedback and the modulation signal are usually coupled to the SQUID using the same coil.

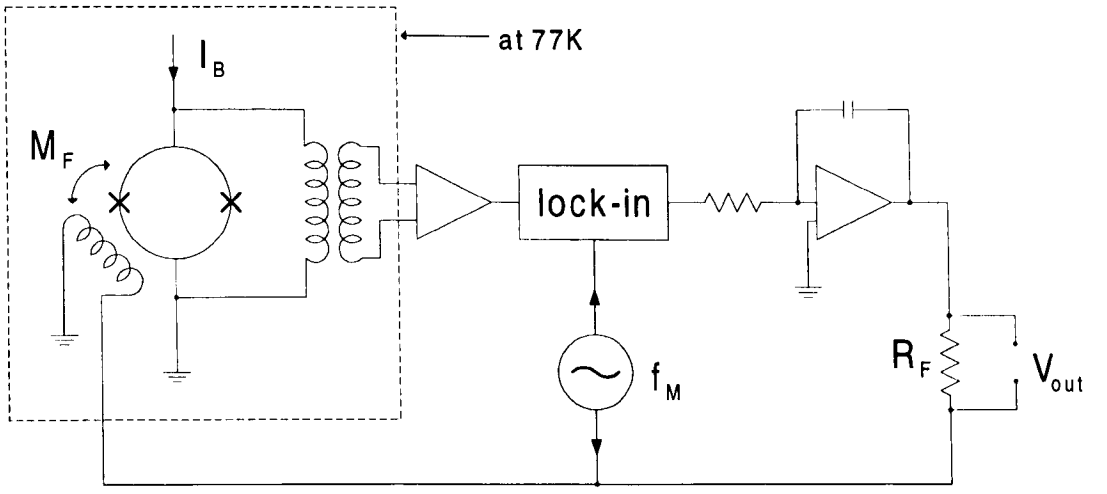

Figure 1.4: Schematic of the flux-locked loop electronics modulation scheme. M_F is the mutual inductance between the SQUID and the coil combining the feedback and modulation signals. R_F is the feedback resistor and f_M the modulation signal frequency.

A voltage change across the SQUID induced by a change in the quasistatic flux (to be measured) is linearly tracked by the lock-in and fed-back to the SQUID as an opposing flux. The output voltage V_{out} measured across R_F thus becomes a linear function of the quasistatic flux, increasing the dynamic range of the SQUID enabling the measurement of inputs equivalent to many flux quanta. Another major benefit of the FLL mode of operation is that the voltage output of the SQUID is effectively shifted to higher frequencies where the voltage noise of a good pre-amplifier becomes negligible compared with the transformer amplified voltage noise output of the SQUID. FLL operation thus enables the measurement of the intrinsic noise characteristics of the dc SQUID. Other read-out schemes and modulation techniques are described in [29].

1.3.2 Noise in dc SQUIDs

White noise

When operated in a FLL, the magnetic flux noise of the SQUID is directly associated with the measured voltage noise via the transfer function ($V_\Phi = |\partial V/\partial \Phi|$), where the voltage noise originates from Nyquist voltage fluctuations across the re-

sistive shunts. Computer simulations of SQUIDs operating at 4.2K by Tesche and Clarke [30] show that the flux noise performance is optimised for $\beta_L \sim 1$. For such a screening parameter Tesche and Clarke show that the maximum slope of the transfer function at optimum bias current is given by

$$V_\Phi \approx R_N/L, \tag{1.14}$$

and that the spectral density of the voltage noise is approximately $\sqrt{16k_BTR_N}$. The flux noise spectral density is thus given by

$$\sqrt{S_\Phi} \approx \frac{\sqrt{16k_BTR_N}}{V_\Phi}. \tag{1.15}$$

Equations 1.14 and 1.15 imply that this frequency independent (white) noise is reduced by decreasing the SQUID inductance and increasing the normal state resistance of the junctions. Note that these expressions are only valid in the regime of $\beta_L \sim 1$ and $\Gamma < 0.2$.

For HTS SQUIDs operating at 77K Equations 1.13, 1.14 and 1.15 do not accurately describe the SQUID's maximum voltage modulation depth, transfer function and flux noise. Koelle *et al.* [31] found experimentally that V_Φ scaled closer to $1/L^2$ for HTS SQUIDs. At such elevated operating temperatures Nyquist noise in the junctions leads to a significant thermally induced flux noise in the SQUID which results in considerable degradation of the V-Φ characteristics. Taking into account the effects of this thermal noise, Enpuku *et al.* [28] obtained the following analytical expression for the transfer function

$$V_\Phi = \frac{4I_CR_N}{\Phi_0(1+\beta_L)}\left(1-\sqrt{\frac{L}{L_T}}\right). \tag{1.16}$$

where $L_T = {\Phi_0}^2/4\pi k_BT$. At liquid helium temperatures, $L_T = 6$nH and for practical SQUID inductances such that $\beta_L \sim 1$, Equation 1.16 reduces to $V_\Phi \approx R_N/L$, but at 77K, $L_T = 321$pH. This places a significant constraint on the SQUID inductance -

for a 100pH SQUID V_Φ is reduced by 56%, and for a 150pH SQUID by 68%. This relatively small upper limit imposed on the inductance limits the effective area and field sensitivity of the SQUID (see discussion below in Section 1.3.3).

For LTS SQUIDs there is good agreement between the simulations and experiment, and the above expressions predict voltage modulation, flux noise and transfer function with reasonable accuracy for SQUIDs which meet the requirements of $\beta_L \sim 1$ and $\Gamma < 0.2$. This is not the case for HTS devices. The maximum voltage modulation depth ΔV measured for an HTS SQUID is generally found to be a fraction (typically 0.4-0.7) of that predicted by Equation 1.13 (*e.g.* [32, 33]). Whether V_Φ is calculated using Equation 1.16 or experimentally measured, the measured flux noise of the SQUID rarely compares well with that predicted by Equation 1.15. For instance consider a SQUID with parameters $I_C = 20\mu$A, $L = 50$pH (*i.e.* $\beta_L \approx 1$) and $R_N = 2\Omega$. Equation 1.16, yields $V_\Phi \approx 48\mu V/\Phi_0$ which, when substituted for the transfer function in Equation 1.15, predicts a white noise of $\sqrt{S_\Phi} \approx 3.8\mu\Phi_0/\sqrt{\text{Hz}}$. Although such low values of white noise have occasionally been achieved with an HTS SQUID (the lowest flux noise reported for a 50pH SQUID is $2.2\mu\Phi_0/\sqrt{\text{Hz}}$ [34]), in general the measured flux noise is much higher than that predicted by Equation 1.15. A recent study by Koelle *et al.* [35] compared the white flux noise values measured for a large sample of dc SQUIDs (fabricated by eight different research groups), with the values predicted by simulations - note that many of these SQUIDs satisfied the conditions that $\beta_L \sim 1$ and $\Gamma < 0.2$ (*i.e.* Equation 1.15 is valid). The measured flux noise was always considerably higher than that predicted by the simulations, typically an order of magnitude larger. In addition there was no clear trend when they compared the measured and calculated flux noise levels as a function of L, R_N, I_C and $I_C R_N$.

Although no theories or simulations seem to accurately predict the white flux noise of HTS SQUIDs, the results discussed in this section provide general rules of thumb to be followed when optimising the performance of dc SQUIDs. There should be sufficient Josephson coupling across the junctions such that $\Gamma < 0.2$, the

screening parameter β_L should be of order unity for optimum flux noise performance, and in general the flux noise is improved by maximising R_N and minimising L.

$1/f$ noise

In addition to the white flux noise discussed above, $1/f$ noise can degrade SQUID performance at low frequencies. There are two known sources of intrinsic noise in dc SQUIDs which have a $1/f$ dependence. The first source of $1/f$ noise arises from fluctuations in the critical current I_C of the junctions. These fluctuations are related to the trapping and releasing of charge carriers by defects in the barrier which raise and lower the barrier potential [36], in turn affecting the critical current of the junction [37]. The presence of a single trap causes the critical current of the junction to randomly switch between two values as charge carriers are trapped and released, producing a random telegraph signal, with the mean trapping time having a Lorentzian distribution. Generally the large number of trapping sites in the junction results in a broad distribution of mean trapping times, and it can be shown that the corresponding Lorentzians sum to give a $1/f$ power distribution [38]. Fortunately, this noise source can be substantially suppressed by using the ac-bias current modulation scheme developed by Koch *et al.* [36]. To implement this scheme the SQUID is operated in the usual FLL, flux modulated, with a peak-to-peak amplitude of $\Phi_0/2$. Synchronously with the flux modulation, an ac-bias current is modulated between positive and negative values $\pm I_B$ at a frequency less than the modulation frequency but greater than the onset frequency of the $1/f$ noise. This averages out the I_C fluctuations thus eliminating the effects of the trapping sites. An ac-flux square wave is applied to the SQUID at the same frequency and in phase with the ac-bias current to compensate the switching which would occur in the SQUIDs V-Φ characteristics, thus maintaining the SQUID in a steady flux state.

The second source of $1/f$ noise in SQUIDs arises from thermally activated hopping of flux vortices between pinning sites in the superconducting film. This was first investigated by Ferrari *et al.* [39, 40]. The distribution of the pinning

site activation energies follows a broad Lorentzian spectrum [41], which results in the hopping of vortices between pinning sites having a $1/f$ distribution. The flux motion due to vortex hopping couples to the SQUID as real flux, and is therefore not eliminated by the ac-bias modulation scheme described above. The contribution of vortex motion to $1/f$ noise is particularly apparent in HTS SQUIDs where the elevated operating temperatures and associated relatively weak pinning sites (characterised by the film's critical current density j_c), become a significant problem. Miklich *et al.* [42] found that even SQUIDs made from excellent YBCO films ($j_c \sim 5 \times 10^6 \mathrm{Acm}^{-2}$) exhibit a significant increase in $1/f$ noise when cooled in an ambient magnetic fields. The increase in flux noise at 1Hz was found to approximately scale with the magnitude of the applied ambient field in which the device was cooled. Typically the increase in flux noise was approximately one order of magnitude for a SQUID cooled in a field strength comparable to that of the earth (50μT), significantly limiting the application of SQUIDs to low noise measurements in an unshielded environment. More recently, Dantsker *et al.* [43] made significant progress in reducing vortex motion and the associated $1/f$ noise of SQUIDs cooled in ambient magnetic fields. They demonstrated that by restricting the linewidth of the SQUID it becomes energetically unfavourable for magnetic flux vortices to penetrate the SQUID's thin film when cooled in fields up to a critical magnitude. By restricting the maximum linewidth of the SQUID to approximately 4μm, Dantsker *et al.* subsequently demonstrated that there was no significant increase in $1/f$ noise up to a critical field strength of approximately 80μT [44].

1.3.3 Field sensitivity

The cumulative effect of the different noise sources discussed above gives rise to an effective root-mean-square (rms) flux noise spectral density $\sqrt{S_\Phi(f)}$, expressed in units of $\Phi_0/\sqrt{\mathrm{Hz}}$. The rms magnetic field sensitivity spectral density of a SQUID is given by

$$\sqrt{S_B(f)} = \frac{\sqrt{S_\Phi(f)}}{A_{SQ}} \tag{1.17}$$

where A_{SQ} is the effective sensing area of the SQUID, defined as the ratio of the flux coupled to the SQUID loop, to the applied magnetic field. To improve the field sensitivity of the SQUID A_{SQ} should be increased. However increasing A_{SQ} typically increases the SQUID inductance, resulting in a reduction in transfer function V_Φ (Equation 1.16) and a corresponding increase in the intrinsic SQUID flux noise (Equation 1.15). The relatively small upper limit placed on the SQUID inductance by Equation 1.16 significantly limits the SQUID effective area and the corresponding magnetic field sensitivity of an autonomous device.

1.4 Magnetometers and Gradiometers

To improve the sensitivity of a SQUID device and resolve the conflict that to minimise flux noise the inductance (and size) of the SQUID must be kept small, while to improve the field sensitivity the effective area (and size) of the SQUID should be made large, one typically couples the signal from a larger pick-up loop to the small loop of the SQUID. The simplest way to do this is to directly connect a large superconducting pick-up loop to the SQUID to form a directly-coupled magnetometer (DCM) as shown in Figure 1.5(a), with the equivalent circuit shown in Figure 1.5(b). For practical magnetometers, where $L_{LP} \gg L_M$, the effective area of the DCM can be approximated as

$$A_{DCM} \approx \frac{L_M}{L_{LP}} A_{LP} + A_{SQ} \tag{1.18}$$

where A_{LP} is the sensing area of the pick-up loop (related to its geometrical area and the degree of flux focusing in the loop), L_{LP} is inductance of the pick-up loop, A_{SQ} is the effective area of the SQUID and $L_M = L_{SQ} - L_J$ is the mutual inductance coupling the pick-up loop and the SQUID (where L_{SQ} is the total SQUID inductance and L_J is the inductance from the striplines incorporating the junctions to which the signal from the pick-up loop does not couple). Since $\sqrt{S_B} = \sqrt{S_\Phi}/A_{DCM}$, the magnetic field

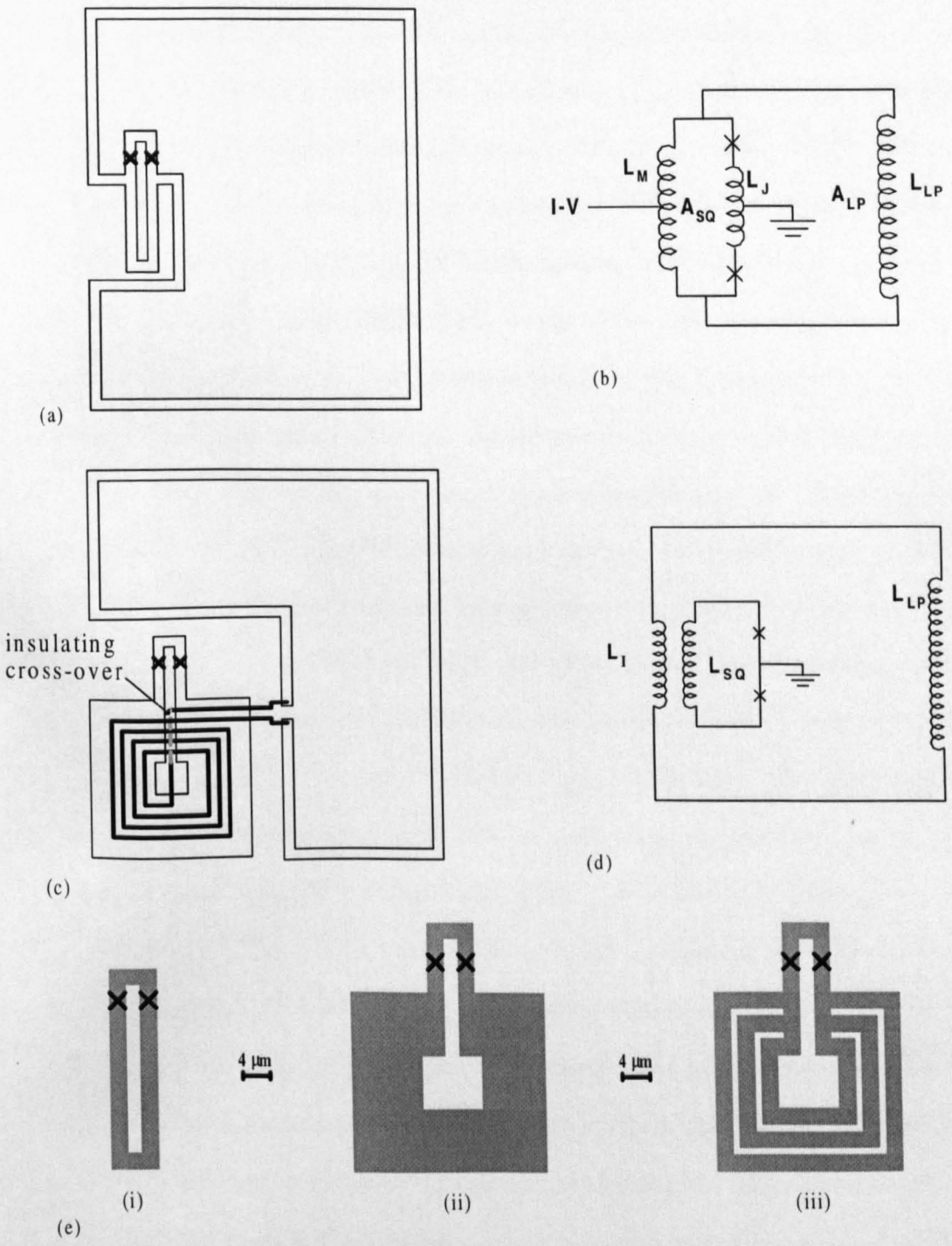

Figure 1.5: (a) Schematic representation of a directly-coupled magnetometer (DCM) and (b) the corresponding equivalent circuit showing the inductances and effective areas as defined in the main text. Note that the total SQUID inductance is $L_{\mathrm{SQ}} = L_{\mathrm{M}} + L_{\mathrm{J}}$. (c) Schematic representation of an inductively-coupled magnetometer (ICM), showing the multi-turn flux transformer (black) and insulating cross-over (grey), and (d) the corresponding equivalent circuit where L_{I} is the inductance of the multi-turn flux transformer and the other inductances are as defined in the main text. (e) Schematics of the various types of SQUIDs commonly incorporated into magnetometers: (i) a narrow-linewidth (4μm) SQUID typically used in DCMs, (ii) a solid washer SQUID typically used in ICMs to improve the mutual inductance with the flux transformer, and (iii) a slotted washer SQUID designed to maintain reasonable coupling with the flux transformer, while minimising $1/f$ noise in the SQUID by restricting the linewidth to approximately 4μm.

sensitivity of a DCM improves linearly with increasing effective area A_{DCM} provided the $1/f$ flux noise in the pick-up loop does not couple significantly to the SQUID. To maximise A_{DCM} the effective area of the pick-up loop A_{LP} should be increased while reducing the mismatch between inductances L_{LP} and L_{M}. Recently Koelle *et al.* [35] showed that the SQUID inductance for a directly coupled device is optimised for $L_{\mathrm{SQ}} \approx 100\mathrm{pH}$. In general A_{LP} is limited by the dimensions of the substrate and L_{LP} is minimised by maximising the width of the tracks of the pick-up loop. Note that the surface area of the substrate used is often restricted by the film growth process and the maximum area over which a stoichiometric and uniform thin film can be grown, thus limiting A_{LP}. The DCM, fabricated from a single layer of superconductor, is the most common HTS SQUID sensor and devices fabricated on $10 \times 10\mathrm{mm}^2$ substrates typically exhibit a magnetic field sensitivity of approximately $50\mathrm{fT}/\sqrt{\mathrm{Hz}}$ in the white noise region (*e.g.* [45, 46, 47]). Any increase in the intrinsic flux noise at low frequencies of such optimised DCMs, incorporating narrow-linewidth SQUIDs (with a maximum linewidth of approximately $4\mu\mathrm{m}$ to minimise flux hopping), can be almost completely suppressed using the ac-bias technique discussed above.

For devices grown on $10 \times 10\mathrm{mm}^2$ substrates, the inductance mismatch is typically of the order 1/100. The inductively-coupled magnetometer (ICM) (shown schematically Figure 1.5(c) with the corresponding equivalent circuit shown in Figure 1.5(d)) couples the signal from the pick-up loop to the SQUID more efficiently. An ICM consists of a large superconducting pick-up loop inductively coupled to the SQUID via a multi-turn superconducting flux transformer. The whole device can either be integrated on a single substrate, or on two separate substrates - the SQUID on one, the pick-up loop and flux transformer on the other coupled in a flip-chip configuration. For LTS devices, where materials processing is a less significant issue, integrated devices are easily fabricated on a single substrate. In LTS superconducting wire can also be used to form a pick-up loop. With the ceramic HTS materials the fabrication of low noise multilayers is difficult, though Dantsker *et al.* [49] have successfully fabricated a fully integrated device on a $10 \times 10\mathrm{mm}^2$ substrate which

exhibited a magnetic field sensitivity of $27\text{fT}/\sqrt{\text{Hz}}$ and $9\text{fT}/\sqrt{\text{Hz}}$ at 1Hz and 1kHz respectively. The flip-chip approach still requires multiple superconducting layers and an insulating layer to form the cross-over in the flux transformer. Successfully establishing a HTS multilayer technology is extremely labour intensive, with few groups worldwide successfully implementing such a thin film technology. In addition the required cross-overs and vias in multiple layer HTS films are a significant source of low frequency flux noise due to the presence of weak pinning sites.

The flip-chip technique has yielded devices with better magnetic field sensitivities than the best fully integrated magnetometers - the multiple thin film layers over the SQUID in a fully integrated magnetometer result in the device having a relatively high intrinsic flux noise. Dantsker *et al.* achieve a better magnetic field sensitivity for their flip-chip magnetometers (where both substrates are $10 \times 10\text{mm}^2$) than for their integrated device discussed above. For their flip-chip magnetometer they measured a magnetic field sensitivity of $8.5\text{fT}/\sqrt{\text{Hz}}$ at 1kHz [50]. Although significant progress has been made in the fabrication of multilayers [51], even the best flux transformers couple significant $1/f$ noise into the SQUID [50]. As a result multilayer magnetometers with sensitivities of better than $50\text{fT}/\sqrt{\text{Hz}}$ at 1Hz remain exceptional. For low frequency applications, any gain achieved in effective area from the improved coupling of the ICM, is offset by the increase in low frequency noise.

The magnetic field sensitivity of an optimised magnetometer is nearly always several orders of magnitude lower than the magnitude of the Earth's magnetic field and other sources of electromagnetic interference (*e.g.* moving car traffic, power transmission lines and electrical equipment). To attenuate the response of the SQUID sensor to such signals, two oppositely wound pick-up loops can be coupled to the SQUID to form a gradiometer. The two pick-up loops can be coupled to the SQUID via a flux transformer to form an inductively coupled gradiometer. Note that for HTS devices, such an inductively coupled gradiometer design is restricted to a planar configuration fabricated from thin films as shown in the Figure 1.6(a) (for LTS devices axial gradiometers and other configurations are easily obtained using

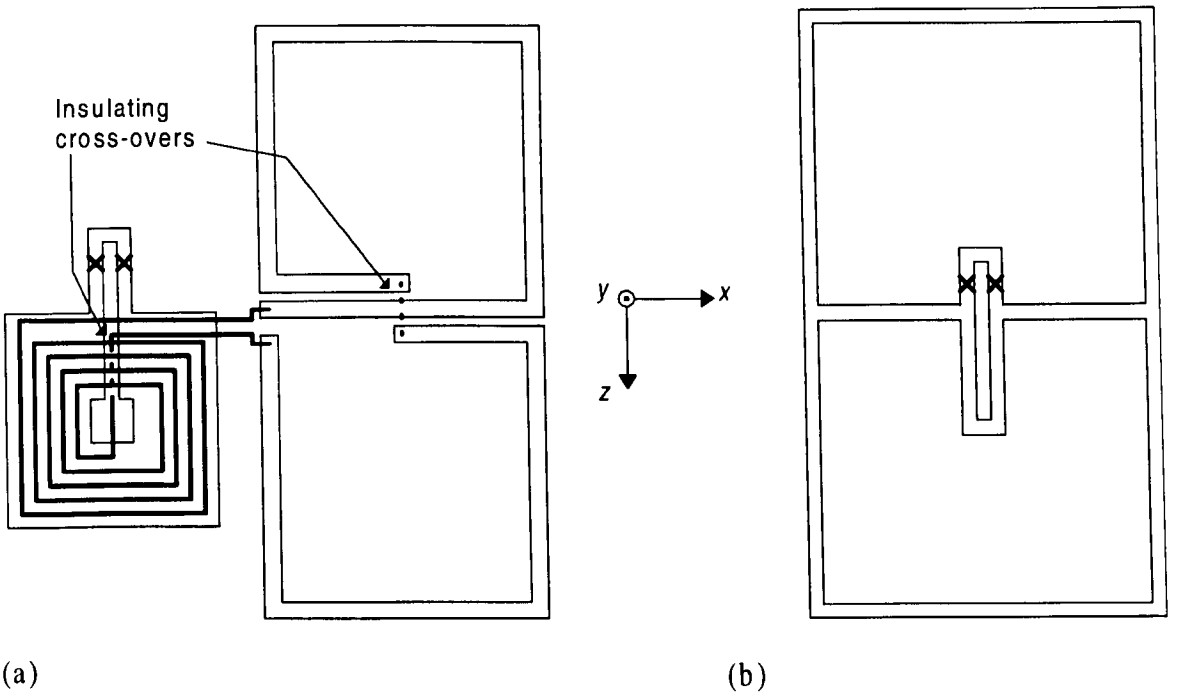

Figure 1.6: Schematic representations of planar gradiometers: (a) an inductively-coupled gradiometer, and (b) a directly-coupled single-layer gradiometer.

superconducting wire). As with an ICM the device can either be fully integrated or flip-chip coupled. A uniform magnetic field couples an identical flux to both of the pick-up loops and, because they flow in opposite directions, the screening currents generated in each pick-up loop cancel and thus couple zero net flux into the SQUID. Magnetic fields generated from distant sources of magnetic interference are approximately uniform at the gradiometer, provided the source is sufficiently far away, and therefore are rejected. Magnetic signals generated in close proximity to the gradiometer have a significant first order gradient, $\partial B_y/\partial z$, resulting in more magnetic flux being present in the loop closer to the source and therefore a net signal being coupled to the SQUID. This enables the gradiometer to measure signals many times smaller than the local environmental noise. Second and higher order gradiometers can be fabricated consisting of three or more loops, extending the rejection of environmental noise, though at the expense of reducing the sensing area for the actual signal to be measured. In practice, the optimum gradiometer order depends on the nature of the signal to be measured as well as the level of magnetic interference.

Inductively coupled gradiometers generally require multiple layers of superconductor to form the multi-turn flux transformer to couple the flux to the SQUID. As with magnetometers, such a technology is difficult to implement and the multiple superconducting layers become a significant source of $1/f$ noise. Alternatively, two single layer films can be flip-chipped together to form an inductively coupled gradiometer [52]. However a problem associated with the flip-chipping technique for gradiometers is that slight errors in alignment of the two chips significantly effect the device balance (see discussion below). To overcome the problems with multilayers and the difficulties associated with alignment when flip-chipping, it is common to fabricate a directly-coupled gradiometer which requires only a single chip with one superconducting layer. Such a first order single-layer gradiometer (SLG) [53] is shown schematically in Figure 1.6(b). Each pick-up loop, directly connected to the SQUID in the centre, couples flux to the SQUID with an inductance mismatch $L_{\mathrm{M}}/L_{\mathrm{LP}}$, where L_{M} is the mutual inductance between the pick-up loops and the SQUID and L_{LP} is the inductance of each of the pick-up loops. Uniform fields generate screening currents of equal magnitude which flow through the central bar in opposite directions and cancel. For an ideal gradiometer, a uniform field results in no current being injected into the SQUID and net zero flux is measured. The gradient fields of small sources in close proximity generate a larger screening current in the loop nearest the source resulting in a net current flowing through the central bar which couples a flux to the SQUID. SLGs are generally always first-order gradiometers, though Lee *et al.* [56] have demonstrated that a second-order gradiometer can be fabricated from a single layer of superconductor.

The gradient field sensitivity of a first-order gradiometer is given by

$$\sqrt{S_{\mathrm{G}}} = \frac{\sqrt{S_{\Phi}}}{lA_{\mathrm{MAG}}}, \tag{1.19}$$

where l is the baseline, defined as the distance between the centre points of the two

pick-up loops, and

$$A_{\mathrm{MAG}} = \frac{L_{\mathrm{M}}}{L_{\mathrm{LP}}} A_{\mathrm{LP}} \pm A_{\mathrm{SQ}} \approx \frac{L_{\mathrm{M}}}{L_{\mathrm{LP}}} A_{\mathrm{LP}} \tag{1.20}$$

is the effective area of the device with one of the pick-up loops removed (*i.e.* operating as a magnetometer) where A_{LP} is the sensing area of one of the pick-up loops. The sign of A_{SQ} is dependent on which pick-up loop is removed. As with magnetometers it is desirable to maximise the effective sensing area of the device while minimising the inductance mismatch. In addition the gradient sensitivity improves linearly with increasing l. Typically, the gradient sensitivities of SLGs incorporating the best low noise SQUIDs, fabricated on $10 \times 10\mathrm{mm}^2$ substrates are in the range 300-500fT/cm$\sqrt{\mathrm{Hz}}$ (*e.g.* [53, 54, 55]).

The gradient sensitivity figures quoted above were measured in a shielded environment. An important figure of merit, which characterises the gradiometer's ability to reject uniform fields and operate in an unshielded environment is the device balance. The balance of a gradiometer can be defined as

$$b = \frac{A_{\mathrm{PAR}}}{A_{\mathrm{MAG}}} \tag{1.21}$$

where A_{PAR} is the parasitic effective area of the gradiometer to uniform fields. While an ideal gradiometer is completely insensitive to uniform fields, in practice A_{PAR} is non-zero due to inevitable variations in the sizes of the two pick-up loops and more significantly the uniform field response of the SQUID itself. Any significant uniform field response degrades the gradient sensitivity of the device when it is operated in an unshielded environment. The balance of gradiometers fabricated on $10 \times 10\mathrm{mm}^2$ substrates is typically of the order of 1/100.

1.5 SQUID Applications

The excellent sensitivity and large dynamic range (when operated using a read-out scheme such as the FLL) make SQUIDs applicable to a wide range of practical measurements. Articles by various authors in *SQUID Sensors: Fundamentals, Fabrication and Applications* (edited by H. Weinstock) [6] and an article by Donaldson *et al.* [7] cover most of the applications that are currently of interest to the scientific community, including several with the potential for commercial exploitation. The Strathclyde group focuses on several applications, the two which are most significant with regards to the device development work described in this thesis are biomagnetism and non-destructive evaluation.

In biomagnetism the SQUID is used to measure the weak magnetic signals generated by biological activity in the human body. SQUID sensors have been used to measure magnetic signals from the heart, brain, nerves, muscles and various other organs. The application of SQUID devices to biomagnetic measurements is challenging in terms of SQUID development, as the weak signals to be measured are comparable to the intrinsic sensitivity of typical SQUIDs. However SQUIDs are the only magnetic sensors capable of such measurements. LTS SQUIDs can be applied to measure brain and nerve signals, though a more realistic application for HTS SQUIDs is the measurement of the stronger magnetic signals generated by the adult heart (magnetocardiography). Biomagnetic measurements are generally performed in heavily shielded environments, typically mu-metal shielded rooms which are expensive and impractical for widespread application in magnetocardiography. For this reason Strathclyde have focused on developing gradiometer devices with improved characteristics for operation in unshielded environments, aiming to develop sensors that can be used for magnetocardiography but require at most only moderate shielding.

The second major application that is of interest at Strathclyde is non-destructive evaluation (NDE), where SQUID sensors are used to detect defects and flaws, typi-

cally in metallic structures. Typically the SQUIDs are scanned over the surface of the sample to map the magnetic field, produced either due to permanent magnetisation in the sample or by inducing eddy currents with an excitation coil. Generally the aim is to detect sub-surface defects or corrosion, ultimately with systems being employed to test building structures and aircraft for fatigue. The sensors must be capable of operating in industrial environments where there are high levels of electromagnetic interference and at Strathclyde we focus on the development of gradiometers for such applications. It should be noted that a major advantage of HTS SQUIDs over LTS devices in this field is the enhanced portability and increased operating time when operating the sensors at 77K rather than 4.2K.

1.6 Aims of this thesis

The work described in this thesis had two main objectives: (1) to develop a reliable step-edge Josephson junction technology as an alternative to the use of bicrystal substrates, and (2) to develop SQUID based sensors with improved performance with particular emphasis on improving the characteristics of devices for unshielded operation. Meeting the latter of these is of particular importance if SQUIDs are to be successfully employed in many applications such as those described in Section 1.5 above. For SQUID sensors to be commercially viable they must be capable of operating in electromagnetically unshielded environments and have the ability to discriminate against unwanted sources. In addition if SQUIDs are to be commercially successful in such applications, the potential benefits of improved performance over competing technologies must not be outweighed by a significant increase in cost. Step-edge junctions only require the use of single crystal substrates, representing significant cost savings over the use of bicrystals.

The thin film deposition system and basic techniques used to fabricate devices are described in Chapter 2. Prior to the outset of this work all the SQUIDs and other multi-junction devices fabricated at Strathclyde incorporated bicrystal junc-

tions. Chapter 3 details the alternative step-edge fabrication procedure that was developed and describes the characterisation and performance of step-edge Josephson junctions. A comparison between the characteristics and performance of junctions produced using the new step-edge technology with that of the bicrystal junctions is included. After successfully establishing the step-edge technology, SQUIDs incorporating step-edges were fabricated and tested. The step-edge SQUIDs are described in Chapter 4, which includes a comparison with the performance of bicrystal SQUIDs. For unshielded SQUID applications a gradiometer is generally required. Various single-layer gradiometer designs incorporating either step-edge or bicrystal junctions have been fabricated and characterised throughout the course of this work, and are described in Chapter 5. Although this thesis is primarily concerned with device development, some discussion describing the practical application of these devices has been included. A novel SQUID device (the gradiometric SQUID) has been developed which, when incorporated into a single-layer gradiometer significantly improves the characteristics of the device for unshielded operation. The gradiometric SQUID devices are described in Chapter 6. Finally Chapter 7 provides a summary of this work and suggests directions for future work.

References

[1] R.C. Jaklevic, J. Lambe, A.H. Silver and J.E. Mercereau, Phys. Rev. Lett. 12, p.159 (1964).

[2] A.H. Silver, R.C. Jaklevic and J. Lambe, Phys. Rev. 141, p.367 (1966).

[3] A.H. Silver and J.E. Zimmerman, Phys. Rev. 157, p.317 (1967).

[4] J.G. Bednorz and K.A. Müller, Z. Phys. B 64, p.189 (1986).

[5] M.K. Wu, J.R. Ashburn, C.J. Torng, P.H. Hor, R.L. Meng, L. Gao, N.Z. Huang, Y.Q. Wang and C.W. Chu, Phys. Rev. Lett. 58, p.908 (1987).

[6] *SQUID Sensors: Fundamentals, Fabrication and Applications*, H. Weinstock (Ed.), Kluwer Academic Publishers, Dordrecht, (1996).

[7] G.B. Donaldson, A. Cochran and R.M. Bowman in *The New Superconducting Electronics*, H. Weinstock (Ed.), Kluwer Academic Publishers, Dordrecht, p.181 (1994).

[8] H.J.M. ter Brake in *Applications of Superconductivity*, H. Weinstock (Ed.), Kluwer Academic Publishers, Dordrecht, p.561 (2000).

[9] B.S Deaver and W.M. Fairbank, Phys. Rev. Lett. 7, p.43 (1961).

[10] R. Doll and M. Näbauer, Phys. Rev. Lett. 7, p.51 (1961).

[11] B.D. Josephson, Phys. Lett. 1, p.201 (1962).

[12] W.C. Stewart, Appl. Phys. Lett. 12, p.277 (1968).

[13] D.E. McCumber, J. Appl. Phys. 39, p.3113 (1968).

[14] J. Clarke and R.H. Koch, Science 242, p.217 (1988).

[15] R.H. Koch, C.P. Umbach, G.J. Clark, P. Chaudhari and R.B. Laibowitz, Appl. Phys. Lett. 51, p.200 (1987).

[16] D. Dimos, P. Chaudhari, J. Manhart and F.K. LeGoues, Phys. Rev. Lett. 61, p.219 (1988).

[17] R. Gross in *Interfaces in High-T_C Superconducting Systems*, S.L Shinde and D. Rudmen (Eds.), Springer Verlag, New York, p.176 (1994).

[18] H. Hilgenkamp, J. Mannhart and B. Mayer, Phys. Rev. B 53, p.14586 (1996).

[19] N.D. Browning, J.P. Buban, P.D. Nellist, D.P. Norton, M.F. Chisholm and S.J. Pennycook, Physica C 294, p.183 (1998).

[20] S. Krey, O. Brugmann and M. Schilling, Appl. Phys. Lett. 74, p.293 (1999).

[21] T. Minotani, S. Kawakami, T. Kiss and K. Enpuku, Jpn. J. Appl. Phys. 36, p.L1062 (1997).

[22] J. Beyer, D. Drung, F. Ludwig, T. Minotani and K. Enpuku, Appl. Phys. Lett. 72, p.203 (1998).

[23] R.W. Simon, J.B. Bulman, J.F. Burch, S.B. Coons, K.P. Daly, W.D. Dozier, R. Hu, A.E. Lee, J.A. Luine, C.E. Platt, S.M. Schwarzbek, M.S. Wire and M.J. Zani, IEEE Trans. Magn. MAG-27, p.3209 (1991).

[24] J. Gao, W.A.M. Aarnink, G.J. Gerritsma, D. Velduis and H. Rogalla, IEEE Trans. Magn. MAG-27, p.3062 (1991).

[25] M.J. Zani, J.A. Luine, R.W. Simon and R.A. Davidheiser, Appl. Phys. Lett. 59, p.234 (1991).

[26] A.J. Pauza, W.E. Booij, K. Hermann, D.F. Moore, M.G. Blamire, D.A. Rudman and L.R. Vale, J. Appl. Phys. 82, p.5612 (1997).

[27] C.D. Tesche and J. Clarke, J. Low. Temp. Phys. 29, p.310 (1977).

[28] K. Enpuku, Y. Shimomura and T. Kisu J. Appl. Phys. 73, p.7929 (1993).

[29] D. Drung in *SQUID Sensors: Fundamentals, Fabrication and Applications*, H. Weinstock (Ed.), Kluwer Academic Publishers, Dordrecht, p.63 (1996).

[30] C.D. Tesche and J. Clarke, J. Low. Temp. Phys. 37, p.397 (1979).

[31] D. Koelle, A.H. Miklich, F. Ludwig, E. Dantsker, D.T. Nemeth and J. Clarke, Appl. Phys. Lett. 63, p.2271 (1993).

[32] E.J. Romans, T.G. Henrici, C. Carr, J.C. Macfarlane, C.M. Pegrum and G.B. Donaldson, IEEE Trans. Appl. Supercond. 7, p.2530 (1997).

[33] K. Enpuku, T. Minotani, F. Shiraishi, A. Kandori and S. Kawakami, IEEE Trans. Appl. Supercond. 9, p.3109 (1999).

[34] R. Cantor, L.P. Lee, M. Teepe, V. Vinetskiy and J. Longo, IEEE Trans. Appl. Supercond. 5, p.2927 (1995).

[35] D. Koelle, R. Kleiner, F. Ludwig, E. Dantsker and J. Clarke, Rev. Mod. Phys. 71, p.631, (1999).

[36] R.H. Koch, J. Clarke, W.M. Goubau, J.M. Martinis, C.M. Pegrum and D.J. Van Harlingen, J. Low. Temp. Phys. 51, p.207, (1983).

[37] C.T. Rogers and R.A. Buhrman, Phys. Rev. Lett. 53, p.1272, (1984).

[38] P. Dutta and P.M. Horn, Rev. Mod. Phys. 53, p.497 (1981).

[39] M.J. Ferrari, M. Johnson, F.C. Wellstood, J. Clarke, P.A. Rosenthal, R.H. Hammond and M.R. Beasley, Appl. Phys. Lett. 53, p.695 (1988).

[40] M.J. Ferrari, M. Johnson. F.C. Wellstood, J. Clarke, A. Inam, X.D. Wu, L. Nazar and T. Venkatesan, Nature 341, p.723 (1989).

[41] M.J. Ferrari, M. Johnson. F.C. Wellstood, J. Clarke, J. Mitzi, P.A. Rosenthal, C.B. Eom, T.H. Geballe, A. Kapitulnik and M.R. Beasley, Phys. Rev. Lett. 64, p.72 (1990).

[42] A.H. Miklich, D. Koelle, T.J. Shaw, F. Ludwig, D.T. Nemeth, E. Dantsker, J. Clarke, N.McN. Alford and T.W. Button, Appl. Phys. Lett. 64, p.3494 (1994).

[43] E. Dantsker, S. Tanaka, P.A. Nilsson, R. Kleiner and J. Clarke, Appl. Phys. Lett. 69, p.4099 (1996).

[44] E. Dantsker, S. Tanaka and J. Clarke, Appl. Phys. Lett. 70, p.2037 (1997).

[45] S. Krey, H.J. Barthelmess and M. Schilling, J. Appl. Phys. 86, p.6602 (1999).

[46] F. Ludwig and D. Drung, Appl. Phys. Lett. 75, p.2821 (1999).

[47] R. Cantor in *SQUID Sensors: Fundamentals, Fabrication and Applications*, H. Weinstock (Ed.), Kluwer Academic Publishers, Dordrecht, p.179 (1996).

[48] B. Oh, R.H. Koch, W.J. Gallagher, P.R. Robertazzi and W. Eidelloth, Appl. Phys. Lett. 59, p.123 (1991).

[49] E. Dantsker, F. Ludwig, R. Kleiner, J. Clarke, M. Teepe, L.P. Lee, N. McN. Alford and T.W. Button, Appl. Phys. Lett. 67, p.725 (1995).

[50] E. Dantsker, PhD Thesis, University of California, Berkeley, (1997).

[51] F. Ludwig, D. Koelle, E. Dantsker, D. T. Nemeth, A. H. Miklich, J. Clarke and R.E. Thomson, Appl. Phys. Lett. 66, p.373 (1995).

[52] L.R. Bär, G.M. Daalmans, K.H. Barthel, L. Ferchland, M. Kühnl and D. Uhl, Supercond. Sci Technol. 9, p.A87 (1996).

[53] S. Knappe, D. Drung, T. Schurig, H. Koch, M. Klinger and J. Hinken, Cryogenics 32, p.881 (1992).

[54] S. Wunderlich, F. Schmidl, H. Specht, L. Dörrer, H. Schneidwind, U. Hübber and P. Seidel, Supercond. Sci. Technol. 11, p.315 (1998).

[55] V. Schultze, R. Stolz, R. Ijsselsteijn, V. Zakosarenko, L. Fritzch, F. Thrum, E. Il'ichev and H.G. Meyer, IEEE Trans. Appl. Supercond. 7, p.3473 (1997).

[56] S.G. Lee, Y. Hwang and B.C. Nam, Appl. Phys. Lett. 73, p.2345 (1998).

Chapter 2

Fabrication

This chapter describes the standard equipment and processes used to prepare the samples discussed in later chapters. Most of the fabrication processes and apparatus discussed in this chapter were established by other past and current members of the group who shall be credited where appropriate - note that the step-edge fabrication process was established by myself, the description of which is devoted a section in a later chapter. Included in this chapter are descriptions of the pulsed laser deposition system used to grow YBCO thin films, the gold and silicon dioxide deposition systems, the photolithography apparatus and procedures, and finally the ion-mill system used to dry etch the YBCO and gold structures of devices.

2.1 YBCO Film Growth

2.1.1 Introduction

YBCO with a critical temperature of 92K, was the first material discovered to be superconducting above the boiling point of liquid nitrogen [1]. This prompted considerable scientific research on the material. Even after the discovery of other compounds with considerably higher critical temperatures (*e.g.* $HgBa_2Ca_2Cu_3O_{8+\delta}$ with a critical temperature of 150K under pressure [2]), YBCO remains the material of choice for thin film applications at 77K. YBCO thin films grown *in-situ* with the *c*-axis normal to the substrate plane have strong flux pinning characteristics resulting in high critical current densities in the *ab*-plane and a low magnetic flux noise.

High quality *c*-axis thin films can be grown on a variety of substrates using several different growth techniques - typically magnetron sputtering (*e.g.* [3, 4]), thermal co-evaporation (*e.g.* [5]) and pulsed laser deposition (*e.g.* [6, 7]). In mag-

netron sputtering the ions of a low pressure ionised gas are accelerated towards a bulk YBCO target cathode. The collision between the ions and the surface of the target ejects the target material which is then deposited onto an appropriately positioned substrate. Thermal co-evaporation involves individually evaporating each of the elements that make up the HTS compound depositing the film layer-by-layer. In pulsed laser deposition (PLD) a pulsed, high energy laser beam ablates material from a bulk YBCO target, forming a plasma plume of material that is transfered stoichiometrically to the positioned substrate. PLD is the chosen technique at Strathclyde and the system and methods used will be described in more detail in Section 2.1.2.

For SQUID fabrication one generally chooses a substrate that has a good lattice match with *c*-axis oriented thin film YBCO; typically commercially available, epitaxially-polished $SrTiO_3$ (STO), $LaAlO_3$ or $NdGaO_3$ substrates are used and sometimes the poorer lattice matched MgO due to its inexpensiveness and suitable characteristics for high frequency applications such as the rf SQUID. Detailed overviews of the properties of YBCO thin films, the various growth techniques and the different substrate materials used can be found in [8, 9, 10].

2.1.2 The Strathclyde PLD system

The Strathclyde PLD system was established by R.M. Bowman and J.H. Clark; a detailed description is given in [11, 12]. Initially the PLD system exclusively used MgO as the substrate material for HTS device applications. Later A. Eulenburg and E.J. Romans optimised the system parameters for YBCO growth on STO substrates [13]. The switch from MgO to STO, with its improved lattice match to YBCO, ultimately resulted in thin films with higher critical current densities, higher critical temperatures and improved reproducibility. Detailed descriptions of the optimisation of the parameters for growth on STO and the methods used to characterise the Strathclyde films are included in [14].

A schematic diagram of the PLD system is shown in Figure 2.1(a). A KrF excimer laser with a wavelength of 248nm is used to ablate material from a bulk

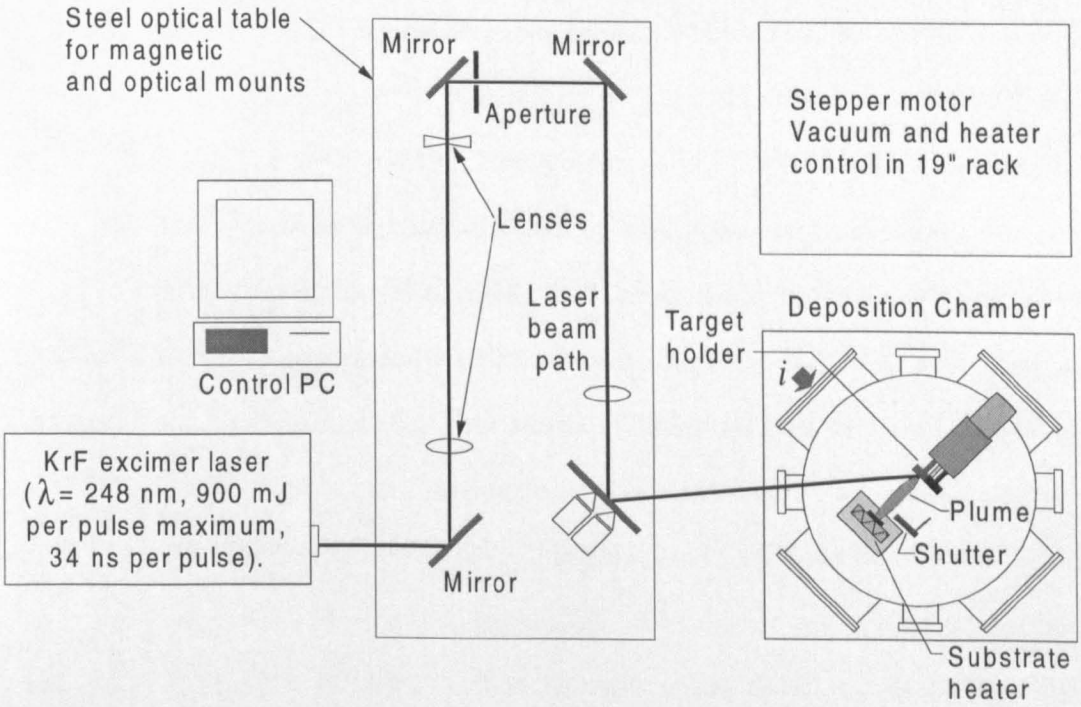

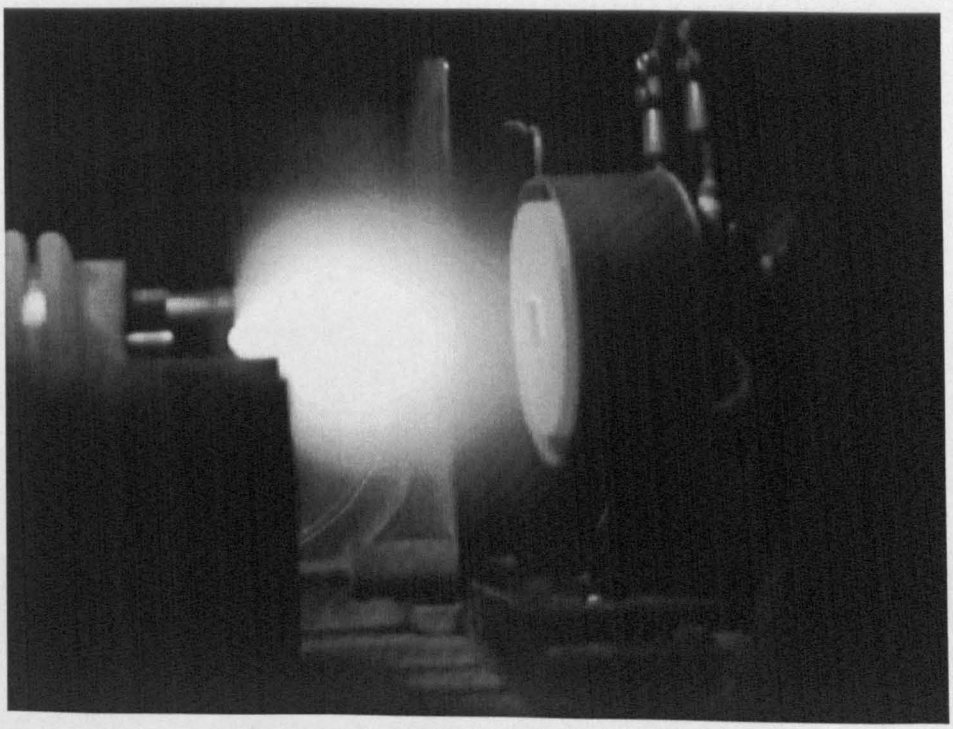

Figure 2.1: (a) Schematic diagram of the Strathclyde pulsed laser deposition system. The arrow marked i indicates the location from which the photograph of the plume shown in (b) was taken.

polycrystalline target. The laser generates pulses of length (full width - half maximum) 34ns at a repetition frequency that is typically set to 10Hz. The laser beam is focused by a series of lenses and mirrors to enter the chamber through a quartz window and strike the target with a spot size of approximately $10 \times 0.5\text{mm}^2$ and a corresponding laser energy density of approximately 1.2Jcm^{-2}. The commercially obtained targets [15] rotate during ablation to minimise target erosion and are attached to a multi-target carousel allowing the target material to be changed *in-situ* for multilayer thin film deposition - although only single layer YBCO thin films were deposited by the PLD system for this work. The substrates are stuck down with silver paint to a heater which has its temperature measured by a thermocouple connected to the centre of the heater block. The temperature of the heater is controlled with a Eurotherm 818 temperature controller. The target-substrate separation is variable up to a distance of 100mm. The vacuum chamber is evacuated by a turbo pump, which is backed by a rotary pump, to a base pressure of 1×10^{-6}Torr with the oxygen pressure during deposition set by a mass flow controller. The PLD system is fully automated - all components are controlled by a PC with simple batch files used to set the parameters for film deposition or other tasks such as annealing of films and devices. Figure 2.1(b) is a photograph taken during the growth of a YBCO film on a $10 \times 10\text{mm}^2$ STO substrate. For this standard deposition procedure a deposition temperature of 820°C (note that corresponds to the temperature in the centre of the heater block as measured by the thermocouple), an oxygen pressure of 0.15mbar and a target-substrate distance of 60mm are used. After deposition the film is annealed in an oxygen pressure of 800mbar while the heater is allowed to cool from 820°C to room temperature.

2.2 Metal and Insulator Deposition

The devices fabricated during the course of this work incorporate gold thin films, deposited on top of the YBCO layer and patterned as contact pads. The gradiometric SQUID devices discussed in Chapter 6 also use gold films as cross-over structures patterned over SiO_2 insulating layers. This section details the deposition of these materials.

2.2.1 Gold deposition

Strathclyde gold thin films are deposited using a conventional dc magnetron sputtering system. The system is pumped down by a diffusion pump backed by a roughing pump to a base pressure of approximately 4×10^{-6}mbar. A needle valve controls argon flow into the chamber, and the sputtering pressure is set manually to 5.3×10^{-3}mbar. The discharge power is set to 50W resulting in a deposition rate of approximately 100nm/min. A pre-sputter time, with the shutter closed, of two minutes is employed to allow the plasma to stabilise and to clean off the surface layers of the target which may have been contaminated.

If a low contact resistance between the gold and YBCO layers is required the sample is annealled in the PLD system for 1hr at a temperature of 475°C in an oxygen pressure of 800mbar to improve the interface between the two materials. Devices are generally designed with large contact pads such that annealling after gold film deposition is unnecessary. The exception to this is the gradiometric SQUID devices which have gold films with small contact areas ($\approx 100\mu m^2$) to the YBCO layer. The fabrication of these devices is detailed in Chapter 6.

2.2.2 SiO_2 deposition

Magnetron sputtering of SiO_2 requires rf power in common with the sputtering of all insulating materials. The system used for this work was originally developed for the LTS niobium technology used at Strathclyde [16]. A stainless steel substrate

holder was made to replace the LTS 3" wafer holders, with copper clips to hold the $10 \times 10\text{mm}^2$ samples in place. Vacuum grease was used to thermally couple the substrate to the sample holder. This prevents scorching of the photoresist on the sample used for lift-off of the SiO_2 film (see Section 2.3 for discussion of the lift-off procedure). The SiO_2 sputter gun is housed in an UHV chamber along with niobium, aluminium and molybdenum sputter guns that are used for LTS device fabrication. The system is pumped by a cryopump and incorporates a load-lock which allows samples to be taken in and out of the chamber while maintaining a base pressure of approximately 1×10^{-9}Torr. A mass-flow controller sets the argon pressure to 3mTorr and the SiO_2 film is deposited at an rf power of 200W resulting in a rate of approximately 50nm/min. As with gold deposition, the SiO_2 is pre-sputtered with the shutter closed for two minutes to allow the plasma to stabilise.

2.3 Device Preparation

All of the devices discussed in this thesis were fabricated in the research group's class 1000 cleanroom, dedicated to the patterning of HTS and LTS devices. For HTS fabrication this facility is used primarily for photolithographic patterning and argon ion milling.

2.3.1 Photolithography

The YBCO and gold layers of the HTS devices are patterned by standard photolithography and argon ion milling. Lift-off photolithography is used to pattern the SiO_2 layers. These procedures shall now be described.

Standard photolithography

To fabricate a structure from a thin film by argon ion milling, or indeed any etching technique, the conventional approach is to use a photoresist mask patterned by image transfer. The photoresist is spun onto the sample and baked, then patterned by partial UV light exposure into a mask to protect the structure to be etched

into the thin film. At Strathclyde, positive photoresist (Shipley S1818) is used and patterned by UV exposure in a Karl Süss MJB3 contact printer (power per unit area approximately 10mW/cm^2) using a chrome mask to protect the regions of the photoresist not to be exposed. The exposed regions of the resist become soluble and are removed in a 1:1 solution of Microposit developer and ultra high purity (UHP) water. The standard procedure used involves two exposure and two develop stages. The first removes the thick photoresist which builds up at the edges and corners of the substrate as the resist is spun. This allows close contact to be made between the chrome photomask and the centre of the photoresist-coated substrate. The second expose and develop patterns the photoresist into the mask to protect the thin film structure to be retained during argon ion milling. The following standard photolithography procedure is used to pattern thin films with a minimum feature size of approximately 1μm achievable: (1) clean the substrate in an ultrasonic bath of acetone and rinse with isopropanol then UHP water, then dry with N_2 gas; (2) spin on photoresist at 6000rpm for 30s to obtain a thickness of approximately 1.6μm; (3) edge removal of the resist - expose for 30s and develop for approximately 40s; (4) pattern the photoresist mask for etching using a 9s expose and develop for about a minute; (5) rinse the sample for approximately 30s in UHP water and dry using N_2 gas.

Argon ion milling

The most common method for etching YBCO thin films is argon ion milling - this method is also used to pattern gold films. The Strathclyde system uses a water cooled Kaufman ion source to generate a beam of neutralised argon ions which bombard the sample and physically remove the material by a collision process. The etching is non-selective - the photoresist mask will be etched as well as the thin film, though clearly one aims to remove all of the unwanted material before etching through the photoresist. The Kaufman source cathode filament thermionically emits electrons which collide with injected Ar atoms, generating Ar^+ ions, on their way

Parameter	Value
Cathode Current	2-4mA
Discharge Voltage	45V
Discharge Current	0.3mA
Accelerator Voltage	300V
Accelerator Current	< 1mA
Beam Voltage	500V
Beam Current	15mA
Neutraliser Current	19mA

Table 2.1: Typical ion gun settings for standard ion mill.

to the anode. A grid system extracts ions from the plasma and accelerates them towards the sample stage. A second (neutraliser) filament at the front of the gun, emits electrons to combine with and neutralise the ions before they strike the sample. Table 2.1 shows the typical settings used to generate a suitable ion beam. The key parameters are the beam voltage and the beam current. A beam voltage of 500V is sufficient to ensure that incident neutralised ions have enough energy (500eV) to eject material from the sample, but without inducing significant damage to the crystal structure of the surface of the sample. The beam current is set to give a reasonable mill rate, without over-heating the sample. The sample is attached with vacuum grease, to a water cooled rotating stage (to improve etching uniformity) inside the vacuum chamber which is pumped to a base pressure of 10^{-5}mbar before being filled with argon gas (using a mass-flow controller) to a milling pressure of 2×10^{-4}mbar. The films are milled with the ion beam perpendicular to the plane of the substrate. The sample stage is grounded to reduce the charging of the sample from ions that fail to be neutralised. A window enables the user to see when the etching of a particular layer is complete. Typical mill times are 6-8 minutes for a 200nm gold film and approximately 45 minutes for a 200nm YBCO film.

Although chemical *wet* etching processes can be used to pattern YBCO and gold thin films, with argon ion milling one can easily achieve a much higher patterning resolution (approximately 1μm). Another advantage of ion milling for etching YBCO is that it is a *dry* process thus avoiding the risk of chemically contaminating the thin film and avoiding contact with water (a typical YBCO chemical etch

solution is a 1:1000 mix of orthophosphoric acid to water). Advantages of the chemical etching process are speed (to wet etch a 200nm film takes approximately two minutes) and that it is the only technique available for etching large wafers (YBCO films on 30 × 10mm substrates have been patterned using ion milling [17], though milling larger substrates would be difficult due to positional variations in the ion beam and the corresponding etch rate).

Lift-off photolithography

Argon ion milling of SiO_2 thin films is difficult as such highly insulating materials are prone to charging effects and thus have variable milling rates. For this reason a lift-off procedure is used to pattern the SiO_2 films. Lift-off involves depositing the thin film over a photolithographically patterned aperture mask then removing the regions deposited directly on top of the photoresist in an acetone ultrasonic bath. The procedure used for HTS is closely related to that used in LTS fabrication at Strathclyde. The sample is prepared with a 1.6μm thick layer of S1818 photoresist which is baked on a hotplate for 3 minutes at 75°C. The edge of the photoresist is removed using a 30s UV exposure and a 40s develop. The second photolithography stage then removes the photoresist from where the SiO_2 is to be patterned into the device structure, using a 10s exposure and 1 minute develop. The sample is then soaked in chlorobenzene for 5 minutes - this allows the resist to be removed cleanly in the acetone. The sample is dried with N_2 gas and then baked for a further 1 minute at 75°C to remove the chlorobenzene. A SiO_2 film is then deposited over the patterned resist mask as described in Section 2.2.2 and then patterned by soaking for 1 hour in acetone before ultrasonic bathing in fresh acetone for about 5 minutes. This dissolves the photoresist lifting off the film on top, leaving only SiO_2 in the regions where the resist was removed by photolithography.

2.4 Summary

This chapter described the standard procedures used for the fabrication of HTS devices at Strathclyde. The PLD system, photolithography and ion milling procedures, were used to grow and pattern all the YBCO devices described in this thesis. The same patterning procedures were used to form contact pads from the gold films deposited using the sputtering system described above. The ion-milling and photolithography procedures are the basis of the step-edge fabrication procedure which is described in depth in the next chapter. The SiO_2 deposition system and lift-off photolithography processes were used to fabricate insulating layers in the gradiometric SQUID devices described in Chapter 6.

References

[1] M.K. Wu, J.R. Ashburn, C.J. Torng, P.H. Hor, R.L. Meng, L. Gao, N.Z. Huang, Y.Q. Wang and C.W. Chu, Phys. Rev. Lett. 58, p.908 (1987).

[2] C.W. Chu, L. Gao, F. Chen, Z.J. Huang, R.L. Meng and Y. Y. Xue, Nature 365, p.323 (1993).

[3] X.X. Xi, J. Geerk, G. Liuker, Q. Li and O. Meyer, Appl. Phys. Lett. 54, p.2367 (1989).

[4] P.K. Srivastava, Ph. Fluckiger, Ch. Leemann and P. Martionoli, in *High T_c Superconductor Thin Films*, L. Correra (Ed.), Elsevier, New York, p.377 (1992).

[5] P. Berberich, B. Utz, W. Prusseit and H. Kinder, Physica C 219, p.497 (1994).

[6] B. Roas, L. Schultz and G. Endres, Appl. Phys. Lett. 53, p.1557 (1988).

[7] G. Koren, A. Gupta, R.J. Baseman, M.I. Lutwyche and R.B. Laibowitz, Appl. Phys. Lett. 55, p.2450 (1989).

[8] J. Phillips, in *The New Superconducting Electronics* H. Weinstock (Ed.), Kluwer Academic Publishers, Dordrecht, p.59 (1994).

[9] F.C. Wellstood, J.J. Kingston and J. Clarke, J. Appl. Phys. 75, p.683 (1994).

[10] D. Koelle, R. Kleiner, F. Ludwig, E. Dantsker and J. Clarke, Rev. Mod. Phys. 71, p.631 (1999).

[11] J. Clark, *Pulsed Laser Deposition of* $YBa_2Cu_3O_{7-\delta}$ *Thin Films and Multilayers for Superconducting Devices*, PhD thesis, University of Strathclyde, (1995).

[12] J. H. Clark, G.B. Donaldson and R.M. Bowman, IEEE Trans. Appl. Supercond. 5, p.1661 (1995).

[13] A. Eulenburg, E.J. Romans, Y.C. Fan and C.M. Pegrum, Physica C 312, p.91 (1999).

[14] A. Eulenburg, *High Temperature Superconducting Thin Films and Quantum Interference Devices (SQUIDs) for Gradiometers*, PhD thesis, University of Strathclyde, (1999).

[15] Praxair Speciality Ceramics, 16130 Wood-Red Road No. 7, Woodinville, WA 98072, USA.

[16] D. Hutson, *The Design, Construction and Operation of Practical Thin Film Superconducting Quantum interference Devices (SQUIDs)*, PhD thesis, University of Strathclyde, (1987).

[17] A. Eulenburg, E.J. Romans, C. Carr, A.J. Millar, G.B. Donaldson and C.M. Pegrum, Appl. Phys. Lett. 75, p.2301 (1999).

Chapter 3

Step-edge Junctions

This chapter describes the fabrication, characterisation and performance of HTS step-edge junctions. The motivation for this work, and a brief review of the literature on the microstructure of step-edge junctions, are given in the first section. The following section describes the fabrication process, including how it is maintained and monitored. The next section details the instrumentation and methods used to measure the properties of the junctions. The final section discusses the electrical characteristics of the step-edges, and includes a comparison between the properties of the step-edge and bicrystal junctions fabricated at Strathclyde.

3.1 Introduction

3.1.1 Motivation

Prior to the work presented in this thesis, the dc SQUIDs and multi-junction devices fabricated at Strathclyde exclusively incorporated bicrystal junctions. The motivation for the work discussed in this chapter was to establish a reliable fabrication process to produce high quality, RSJ-like step-edge junctions as an alternative to the bicrystal technology.

Step-edges have several advantages over the use of bicrystal substrates. The topological limitation imposed by a straight, single grain boundary across the centre of the bicrystal substrate presents an inconvenience in device design. With step-edges, junctions can be placed anywhere on the substrate and superconducting tracks can cross the centre of the substrate without crossing a grain boundary. (In Chapter 6 the gradiometric SQUID is introduced, a device which requires the layout freedom of step-edge junctions.) The other major advantage of step-edges is the

saving in terms of substrate costs compared to bicrystals: a single crystal substrate is approximately 5 times less expensive. A common misconception is that the performance of junctions and SQUIDs incorporating step-edge junctions is generally poorer than that of bicrystal devices. In this and the following chapter, it will be demonstrated that this need not be the case. The only significant disadvantage of the step-edge technology is that it is more labour intensive, with considerable effort required to establish and maintain a reliable fabrication process.

3.1.2 Microstructural properties

The development, analysis and optimisation of step-edge junctions has been reported extensively in the literature, and only a brief review of the microstructure of step-edge junctions will be given here. An extensive review can be found in [1].

The electrical properties of the junction are closely related to the detailed microstructure of the film grown over the step [2]. The key parameters that determine the junction properties are the step-angle θ and the ratio of the film thickness t to step height h. In addition, the nature of the film growth over the step depends on the substrate material, the edge morphology of the step and the film growth technique [3, 4].

In the present work (100) STO substrates were used with YBCO thin films grown by pulsed laser deposition as described in Chapter 2. For such materials, the dependence of the film microstucture on the step-angle θ has been reported in the literature [5]. For $\theta > 45°$, the film grows with a different c-axis orientation on the step, with two approximately 90° tilt grain boundaries at the top and bottom of the step. For $\theta \sim 45°$ the grain boundaries are similar and the junction behaves as two weak links in series. For steeper steps ($\theta \geq 60°$), the two grain boundaries become dissimilar such that the lower is likely to have a smaller critical current and dominate the junction's electrical characteristics. For SQUID use a dominant grain boundary is advantageous since only a single weak link in each junction defines the SQUID characteristics. The relationship between the film microstructure and

step-angle is strongly dependent on the choice of substrate material. For example, YBCO films on MgO substrates have an entirely different dependence, with grain boundaries reported to occur for step-angles as low as $\theta \sim 20°$ [6].

Obtaining low-noise, RSJ-like junctions is highly dependent on the ratio t/h. The optimum value of t/h depends on the choice of substrate material. For MgO substrates RSJ-like junctions have been fabricated over the range of $0.4 \leq t/h \leq 1.1$ [6]. For STO substrates, RSJ- like behaviour is usually observed over a narrower range (*e.g.* $0.62 \leq t/h \leq 0.78$ in [7]). However, for any type of substrate material, the exact range depends on the step fabrication process and on the film growth technique.

Junctions that have t/h values outside the RSJ-like range tend to exhibit resistive or flux-flow I-V characteristics. When the film thickness is considerably smaller than the step height, resistive characteristics are observed due to a discontinuity in the superconducting pathway over the step. For film thicknesses significantly larger than the step height, flux- flow behaviour is observed, as a result of superconducting shorts, due to outgrowths in the film over the step.

3.2 Fabrication

3.2.1 Introduction

Many different techniques and materials have been reported in the literature for the fabrication of step-edges. Wet-etching [8] and lift-off techniques [9] have been used to define the step, but the most common method is to dry-etch the step by ion-milling a masked substrate. Niobium [10] and diamond-structure thin-film carbon masks [11] have been used. However the simplest approach, and the one adopted here, is to use a photoresist mask.

Obtaining a steep edge on insulating materials such as STO is more difficult than obtaining steep edges on materials such as YBCO. This is due to the slower mill rate of STO as well as charging effects and sensitivity to beam neutralisation when

ion milling insulating materials. As the morphology of the step-edge determines the junction properties, a straight well-defined and sufficiently steep (*i.e.* $\theta \geq 60°$) step-edge is desirable. In addition, to obtain a step of suitable height, the milling time is considerably longer than the milling time for a typical YBCO thin film. Because of these factors, great care must be taken to ensure that a high quality, well-defined photoresist edge is patterned on the substrate before milling. The right photolithography parameters are crucial for obtaining a resist mask of sufficient quality to produce a good step-edge.

The standard photolithography and milling procedures, using the same chemicals and equipment as described in Chapter 2, are the basis of the step-edge fabrication process.

3.2.2 Photoresist mask preparation

For successful step-edge production the photoresist mask must develop cleanly, be straight and well defined, and be of a sufficient steepness and thickness. The thickness of the resist is set by the spin speed when coating the substrate. To make a step-edge of suitable height (typically 300nm), a resist thickness of 1.6μm was found to be sufficient. This was obtained from a spin speed of 6000rpm, as specified by the resist manufacturer. (The thickness of the resist was also checked using a Dektak profilometer to confirm the manufacturer's data.)

As discussed above, to produce step-edge Josephson junctions on STO substrates with suitable electrical characteristics for use in SQUIDs, the steps must be steep with an angle greater than 60°. To achieve such an angle by argon ion-milling, the angle of the photoresist should be as steep as possible ($\geq 80°$). The resist mask must also have a straight edge to produce a straight step-edge for low noise junction fabrication [12]. Such requirements necessitate a controlled photolithography process, that takes place in suitable environment for photoresist processing. The chemistry of the photoresist is dependent on air temperature and humidity, and for this reason the controlled environment of a clean room is required to produce

suitable masks for step-edge fabrication. The conditions recommended by the photoresist manufacturer are an air temperature of approximately 20°C and humidity of 45-55%. During the course of this work, the clean room air conditioning system failed and was replaced. With no environmental control, the humidity was typically less than 20% and the temperature varied between 20°C and 30°C. During this period all of the step-edges fabricated had angles of less than 40°.

Given the correct environmental conditions, producing a resist mask requires a precise exposure time and to a certain extent a controlled develop time. If the mask is under-exposed, the resist requires an excessive develop time and will not develop cleanly. Small deposits of resist may remain on the substrate, and the edge will be poorly defined. If over-exposed, a steep and straight edge will not be defined in the resist when developed. The pre- expose bake conditions are also crucial. The amount of PhotoActive Compound (PAC) present in the resist, prior to exposure, is determined by the temperature and duration of the pre-expose bake. The dissolution rate of the resist in the developer is a function of the amount of PAC converted by the UV exposure. The application of heat destroys PAC, thus an excessive bake time and/or temperature will result in all the PAC in the resist being destroyed and the resist will not develop. In contrast no pre-expose bake would leave the resist too soft to be developed successfully. The bake conditions should be set to find the right balance between these two extremes. Suitable exposure and bake times should allow the resist to be completely developed in a time of 30-50s. Too long a develop time is undesirable as undercutting of the resist becomes a problem, a consequence of the developer attacking the resist at the interface with the substrate.

After patterning, the resist masks were examined using an optical microscope. Figure 3.1 shows photographs of two resist edges, highlighting some of the effects discussed above. The steepness of the edge of resist can be very roughly approximated through optical inspection by examining the thickness of the optical fringe at the resist edge. The sample shown in Figure 3.1(a) clearly has a rougher edge and a wide fringe and therefore shallower angle than the sample shown in (b).

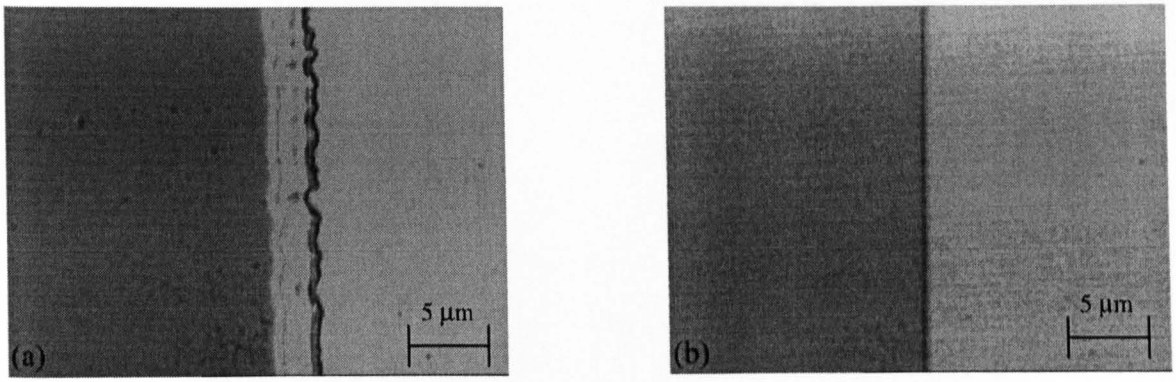

Figure 3.1: Optical micrographs of photoresist edges: (a) an over-exposed resist edge with a rough edge morphology and shallow angle, and (b) a resist edge suitable for step-edge fabrication produced using the optimised recipe as detailed in Table 3.1

The initial optimised photolithography procedure developed for step fabrication, has been monitored and adjusted to try to maintain a high yield of suitable step-edges. Some time after the process was established, the initial high yields began to drop and the fabrication parameters required adjustment. Table 3.1 illustrates how the optimised conditions have changed, showing the current parameters used to produce the resist mask, and the ranges over which these settings have varied during the course of this work.

3.2.3 Step etching

Once the photoresist has been prepared, the samples are ready to be etched. Conventional Ar^+ milling, as described in Chapter 2, is used to etch the step. The sample is mounted on a water-cooled, rotating stage (to improve step uniformity)

Process	Current Value	Range of Values
Pre-bake temperature	95°C	95°C
Pre bake time	95s	80-110s
Edge removal expose	30s	30s
Edge removal develop	30-40s	30-40s
Step mask expose	8.5s	7-10s
Step mask develop	30-40s	30-90s

Table 3.1: Photolithography settings for step-edge fabrication. The table shows the current values of the fabrication parameters and the range over which they have varied during the course of this work.

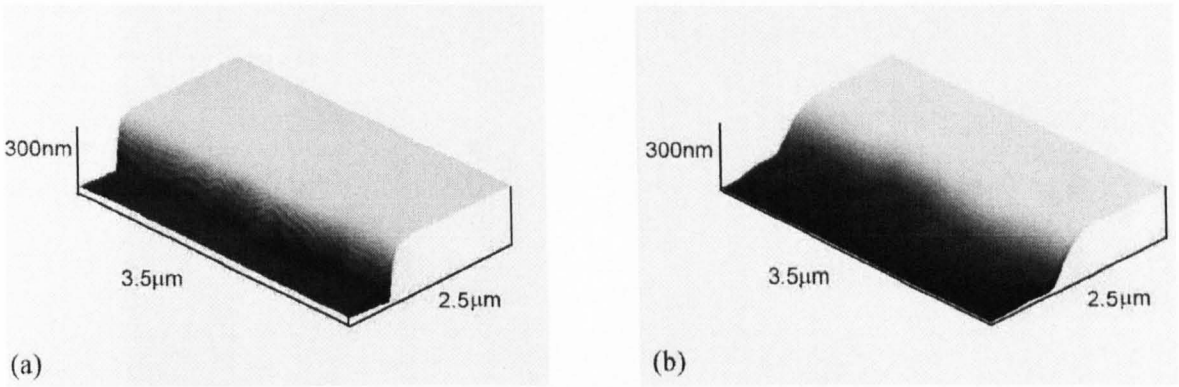

Figure 3.2: Atomic force microscope (AFM) images of step-edges. (a) An AFM image of a step-edge produced with the optimised fabrication process. The step height $h \approx 300$nm and step-angle $\theta \sim 70°$. (b) An AFM image of a step-edge with a shallow angle of $\theta \sim 40°$.

and milled with the beam incident at 90° to the substrate plane. Deviations from a 90° milling angle were found to reduce the angle of the step-edge significantly. Samples are milled for a controlled time to produce a step with approximately the desired height. After milling, the samples are cleaned and inspected with the optical microscope, to examine the straightness of the edge, and with the Dektak profilometer, to measure the height of the step.

Prior to film deposition, each step-edge was examined using an atomic force microscope (AFM) to measure the angle of the step and inspect the morphology of the edge. When the photoresist mask preparation and milling procedure were fully optimised, the step-angle (θ) was in the range 60° to 70°, and the step height varied by less than 5% across the substrate. Figure 3.2(a) shows an AFM image of a typical step produced from the optimised fabrication procedure, and Figure 3.2(b) shows a step produced when there were problems with the fabrication process.

3.2.4 Junction patterning

After the step has been etched, YBCO thin films are grown by pulsed laser deposition, and patterned into the junction structure using standard photolithography and Ar^+ milling as described in Chapter 2. A gold layer is sputtered over the sample and patterned to form electrical contacts. A scanning electron microscope

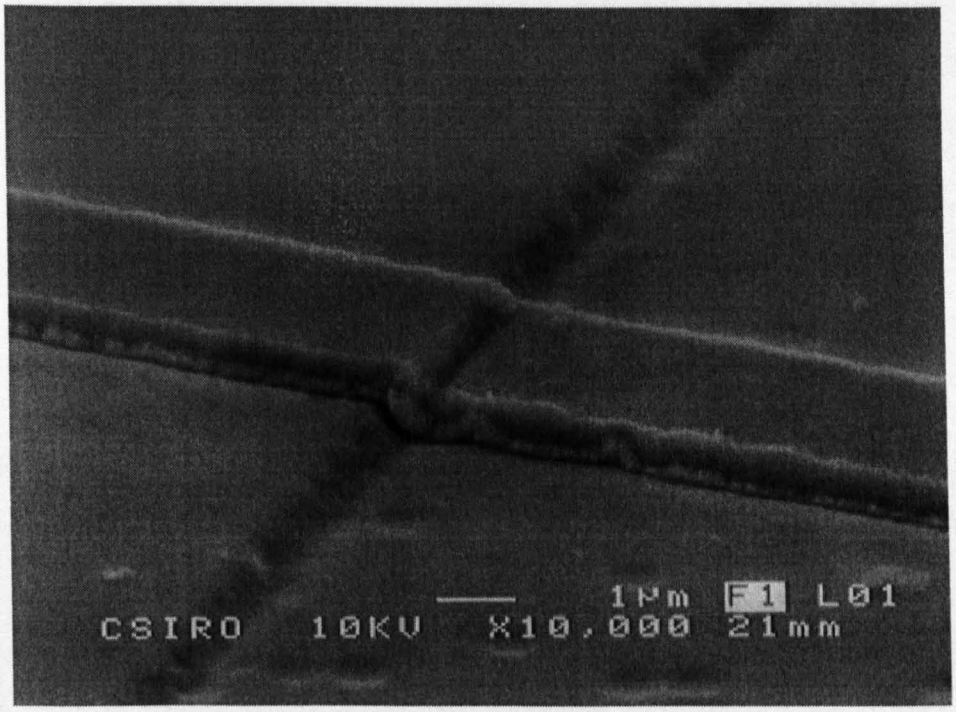

Figure 3.3: A scanning electron microscope image of a completed step-edge junction. This image was taken at CSIRO with assistance from Dr Cathy Foley.

(SEM) image of a completed junction is shown in Figure 3.3.

Finally, the junction chips are mounted onto printed circuit board (PCB) chip carriers with the gold contact pads connected to the copper of the PCB by ultrasonically bonded aluminium wire.

3.3 Experimental Details

3.3.1 Introduction

I-V curves were measured for all the step-edge junctions fabricated throughout this work. A numerical fitting procedure was used to extract the junction properties from the measured *I-V* curves. The modulation of the junction critical current with applied magnetic field, $I_C(B)$, was measured for some of the junctions.

Before discussing the different techniques used to characterise the junctions, a few details that are general to all the experimental measurements performed should be mentioned. All the junctions were tested at 77K in a liquid nitrogen bath. The

junctions were cooled inside a single layer of mu-metal, to provide shielding from the Earth's field and low frequency interference. The electrical characteristics of the junctions were always measured in a four terminal configuration using a rf-noise-filtered probe. An EG&G pre-amplifier was used to provide additional low-pass filtering of the voltage signal with a 3dB cut-off at 30Hz to reduce mains interference.

3.3.2 Data acquisition

The measurement of the I-V curve is computer controlled using in-house software developed by J. Kuznik [13]. An HP-3245A current source is driven by the control software to sweep a designated range of bias currents through the sample. The voltage across the sample is amplified by a factor of 1000 by the EG&G preamplifier and measured by an HP-3458A multimeter for every value of bias current applied by the source. The data is fed back into the control software and the voltage across the junction is recorded as a function of the bias current. For junctions exhibiting RSJ-like characteristics, estimates of the junction critical current I_C and normal state resistance R_N can be made. While R_N can be measured with reasonable accuracy from the recorded curve by measuring the gradient of the curve at currents much larger than I_C, an accurate measure of I_C for junctions with small critical currents is difficult due to thermal noise rounding of the I-V curve (see Section 3.3.3 and discussion in Chapter 1). A numerical fitting procedure used to extract an accurate value for I_C from the I-V curve is described in below.

The measurement probe has an integrated, calibrated coil, to enable the measurement of junction characteristics in the presence of an applied magnetic field. In-house software (developed by P. Tavares [14]) drives an additional HP-3245A source to bias the probe coil with a constant current and uses the Kuznik program to measure the I-V curve in the presence of the magnetic field generated by the coil. The Tavares program extracts the current ($\approx I_C$) from the Kuznik I-V data corresponding to a non-zero voltage using a 1μV criterion. The software repeats this process over a designated range of coil currents to obtain an $I_C(B)$ curve.

3.3.3 RSJ curve fitting

The I-V characteristics measured for an HTS Josephson junction at 77K will have deviations from the ideal RSJ model. Superconducting channels may be present in parallel with the actual Josephson junction resulting in excess supercurrent flow though the junction. The current at which the junction switches to the voltage state will be $I_C + I_{ex}$ where I_{ex} is the excess supercurrent. A straight line fit to the asymptote of the measured I-V characteristics is measured will correspond to a summation of the junctions critical current I_C and the excess current associated with charge carrier transport through the superconducting channels. Noise rounding is present in the I-V curve due to thermal (Nyquist) noise in the junction of spectral density $S_I = 4k_BT/R_N$. As a result the junction may enter the resistive state for bias currents below I_C. The measured I-V curve records a time averaged voltage and as a result will deviate from ideal RSJ characteristics. While R_N can be measured reasonably accurately from the recorded I-V curve by linearly fitting the resistive part of the data where $I \gg I_C$, it is difficult to accurately measure I_C due to the effect of noise rounding.

A programme was written by A. Eulenburg [15] to calculate the I-V characteristics given by the RSJ model at non-zero temperature, based on the work of M. Colclough [16]. The programme numerically fits a theoretical noise-rounded RSJ curve (at 77K) to the measured I-V characteristic, for varying parameters I_C and R_N. The optimum data fit yields a best estimate of the junction properties I_C and R_N. Note that an excess current could potentially comprimise the quality of the RSJ fit, as no excess current term is included in the programme's fitting procedure. However, in general their is little evidence of any excess current in the I-V characteristics of a good junction at currents much greater than I_C, and consequently any pertubations in the fitted values of I_C and R_N arising from excess currents are considered negligable.

To illustrate the need for this fitting procedure to accurately obtain I_C, examples of the numerically fitted I-V curves for two step- edge junctions are shown in

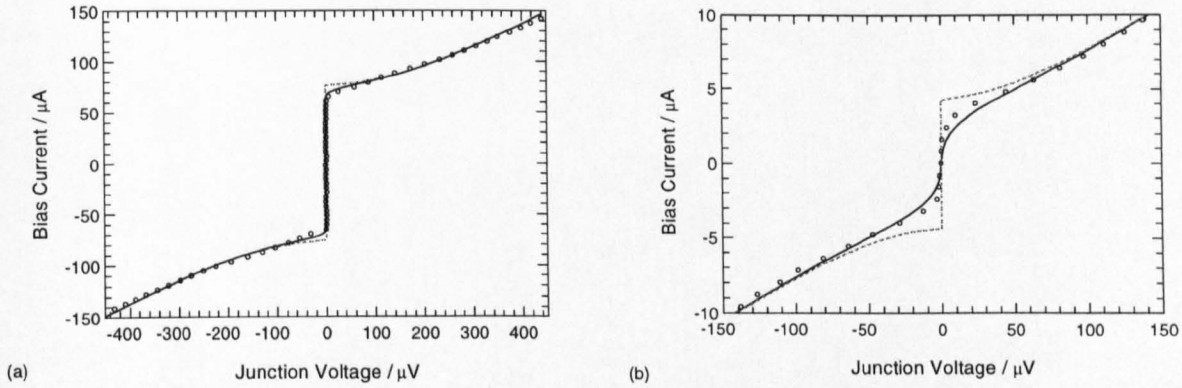

Figure 3.4: I-V curves for two step-edge junctions measured at 77K (ooo) with RSJ fits including noise rounding (—) and the ideal RSJ curves for the junctions at $T = 0$K for the fitted I_C and R_N values (---) calculated using Equation 1.7. The junctions shown have fitted parameters (a) $I_C = 76\mu$A and $R_N = 3.52\Omega$; and (b) $I_C = 4.1\mu$A and $R_N = 15.8\Omega$.

Figure 3.4. A junction with a relatively large $I_C = 76\mu$A is shown in Figure 3.4(a), and a second junction with a small $I_C = 4.1\mu$A is shown in Figure 3.4(b). For both junctions the figure shows the measured data taken at $T = 77$K, the RSJ fit to that data and the ideal RSJ curve at $T = 0$K given by Equation 1.7 using the fitted values of I_C and R_N. For both junctions there is a discrepancy between the data at $T = 77$K and $T = 0$K. However this discrepancy is more significant for the junction with the smaller critical current, as the thermal energy becomes comparable with the Josephson coupling energy for junctions with $I_C \sim 3.3\mu$A [17] (as discussed in Chapter 1). For junctions with large critical currents a reasonable estimate of I_C can be made by taking the smallest current for which a non-zero voltage appears across the junction, but for smaller critical currents this method becomes more inaccurate and one can significantly underestimate I_C. Unless otherwise stated all values of I_C and R_N quoted in this thesis were obtained using this fitting procedure.

3.4 Junction Electrical Properties

This section describes the properties of the step-edge junctions fabricated during the course of this work. Detailed discussions of the dependence of the junction properties (J_C, ρ_N and $I_C R_N$) on the ratio of film thickness to step height (t/h),

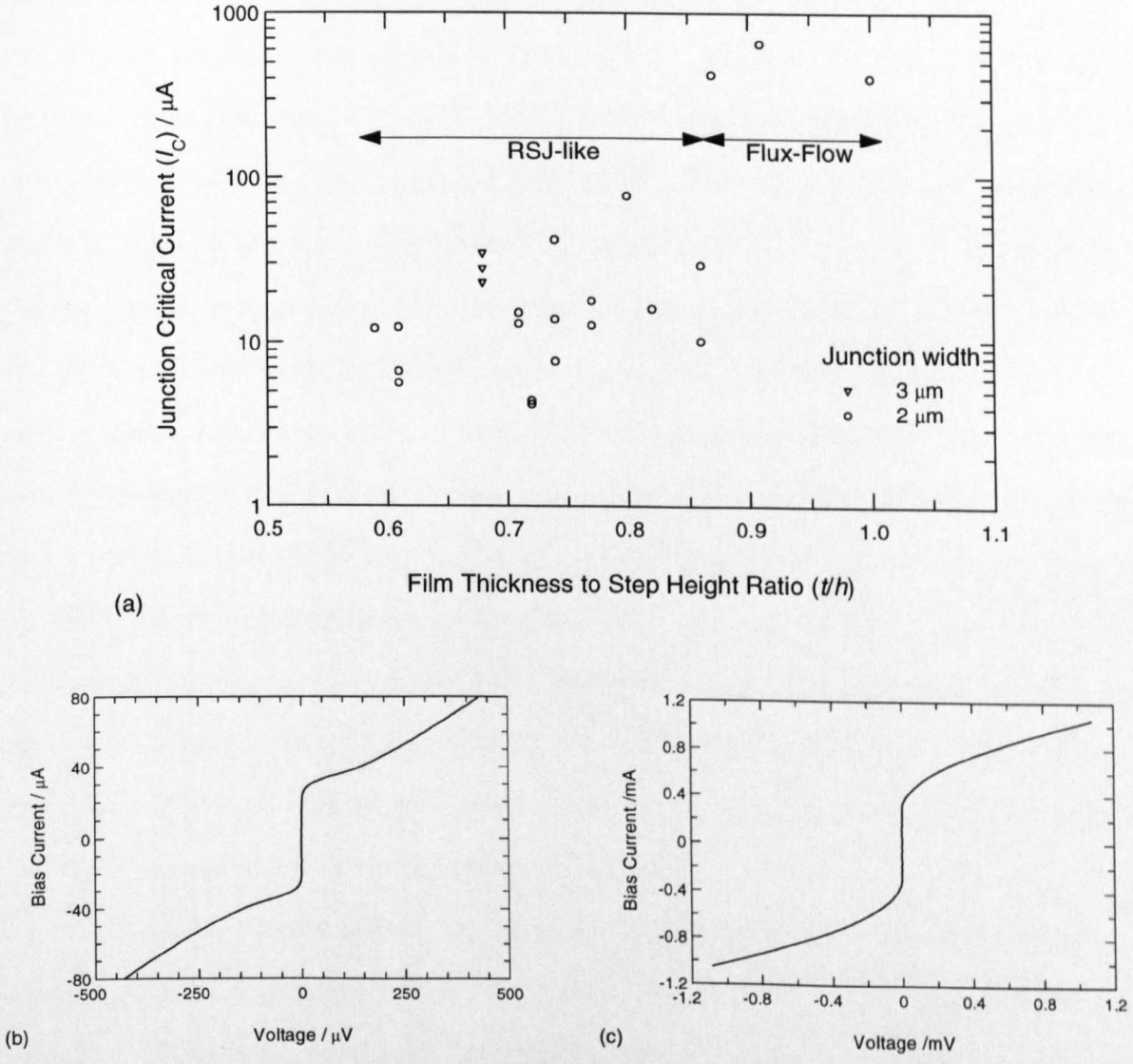

Figure 3.5: (a) The variation in junction critical current I_C as a function of the ratio of film thickness to step height t/h. (b) A typical RSJ-like I-V curve obtained at 77K. (c) An example of a flux-flow I-V curve obtained at 77K.

the behaviour of the junctions in applied magnetic fields and a comparison with the properties of Strathclyde bicrystal junctions are included.

3.4.1 t/h dependence

To study the dependence of the junction characteristics on the t/h ratio, the film thickness was kept constant at $t = 200$nm and tracks of width $w = 2$ or 3μm were patterned on steps of various heights. Note that all the junctions discussed in this section were fabricated on optimised steps (*i.e.* $\theta \geq 60°$).

The variation in measured critical current I_C with t/h for devices fabricated

on 6 different chips is shown in Figure 3.5(a). I_C for RSJ-like junctions was measured using the fitting procedure discussed above; for flux-flow like behaviour I_C was estimated from the I-V curve. RSJ-like I-V characteristics were observed for $0.59 \leq t/h \leq 0.86$. In this regime the yield of RSJ-like junctions was good, approximately 85%. There was no evidence of multijunction behaviour: no additional "kinks" in the voltage state were observed for any of the RSJ-like junctions up to the maximum bias currents applied (typically $\approx 5I_C$). For $t/h < 0.59$ the junctions were resistive, whereas for $t/h > 0.86$ they exhibited flux-flow behaviour. Examples of measured RSJ-like and flux-flow characteristics are shown in Figure 3.5(b) and Figure 3.5(c) respectively. In the RSJ-like regime there was a reasonably large ($> 100\%$) chip-to-chip variation in I_C. On a single chip the spread was smaller, with an average on-chip spread in I_C of 55% for the 6 chips, and a spread of approximately 10% on the best chip on which 4 junctions were tested. These findings are in broad agreement with reports from other groups who fabricate junctions using the same materials and a similar process [7, 18, 19].

The critical current density J_C of each of the RSJ-like junctions is plotted on a linear scale as a function of t/h in Figure 3.6(a), with Figure 3.6(b) showing the variation in the junction normal state resistivity ρ_N with t/h. The large scatter in the two figures makes it difficult to identify any significant dependence of J_C or ρ_N on t/h, though the data suggests there may be an increase in J_C and a corresponding decrease in ρ_N with an increasing t/h. A similar trend was reported in [18], where J_C was found to increase with increasing t/h for a fixed film thickness. The normal state resistance R_N values measured for the junctions are shown in Figure 3.6(c), plotted versus t/h. Figure ??(d) shows the spread in $I_C R_N$ product for RSJ-like junctions. The junctions have a mean $I_C R_N$ of 130μV with a standard deviation of 60μV. The $I_C R_N$ product appears to be largely independent of t/h in the RSJ-like regime. This is beneficial as it is difficult to control h exactly during ion-milling - a consequence of the charging effects when milling insulating materials, as discussed earlier in this chapter.

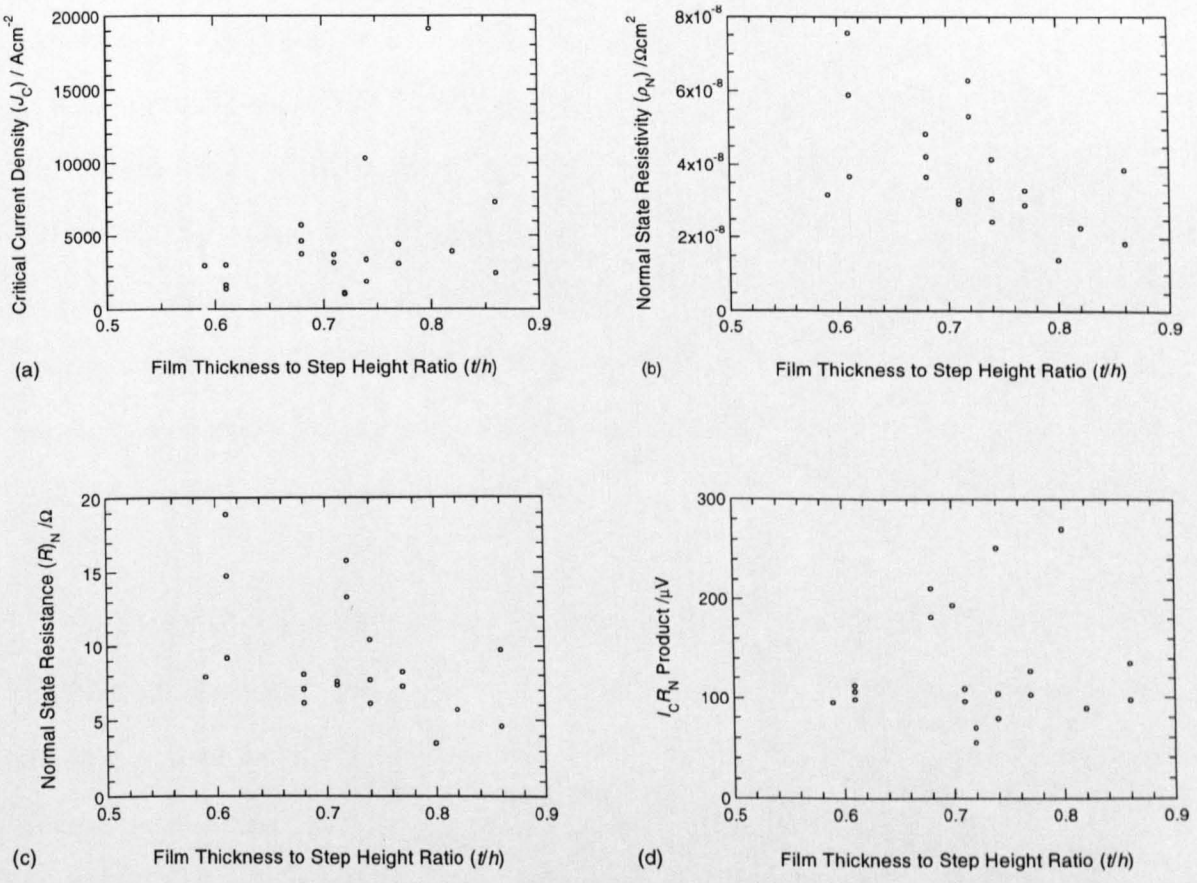

Figure 3.6: (a) Variation in junction critical current density J_C for the RSJ-like junctions as a function of the ratio of film thickness to step height t/h. (b) Variation in junction resistivity ρ_N as a function of t/h. (c) Variation in the junction normal state resistance R_N as a function of t/h. (d) Variation in junction I_CR_N product as a function of t/h.

3.4.2 $I_C R_N$ scaling with J_C

The scaling relationship between the $I_C R_N$ product and the junction critical current density J_C provides important information about the nature of the supercurrent and normal current transport across the grain boundary [20]. The transport mechanisms present in HTS Josephson junctions are not yet clearly understood, but the physics is evidently different from that of the LTS superconductor-insulator- superconductor (SIS) junctions; for LTS SIS junctions $I_C R_N$ is largely independent of J_C and approximately equal to Δ/e, where Δ is the energy gap of the LTS material. For a wide range of HTS grain boundary junctions, there are reports that $I_C R_N$ varies with ${J_C}^n$ where $n \approx 0.5 \pm 0.1$ (*e.g.* [21]-[24]). This scaling behaviour has also been observed in other types of HTS junctions: in ramp-edge junctions [25] and also trilayer junctions [26]. This implies that a similar physical mechanism determines the scaling relation for both grain boundary and other HTS junction types. Comprehensive discussions on this scaling relation can be found in references [20] and [27].

The step-edge junctions discussed here show scaling relations in agreement with the findings discussed above. For the RSJ-like step-edge junctions a straight line fit yields $n = 0.49$ as shown in Figure 3.7. Note that J_C is estimated by assuming the critical current distribution is uniform across the junction and taking the product of the film thickness and the junction width ($t \times w$) as an estimate of the cross-sectional area of the junction.

3.4.3 Junction behaviour in a magnetic field

The behaviour of I_C in an applied magnetic field B can provide important information about the junction uniformity and the stability of the junction for SQUID applications in an unshielded environment. For an ideal Josephson junction, one would expect the junction's critical current to show Fraunhofer-like modulation [29]

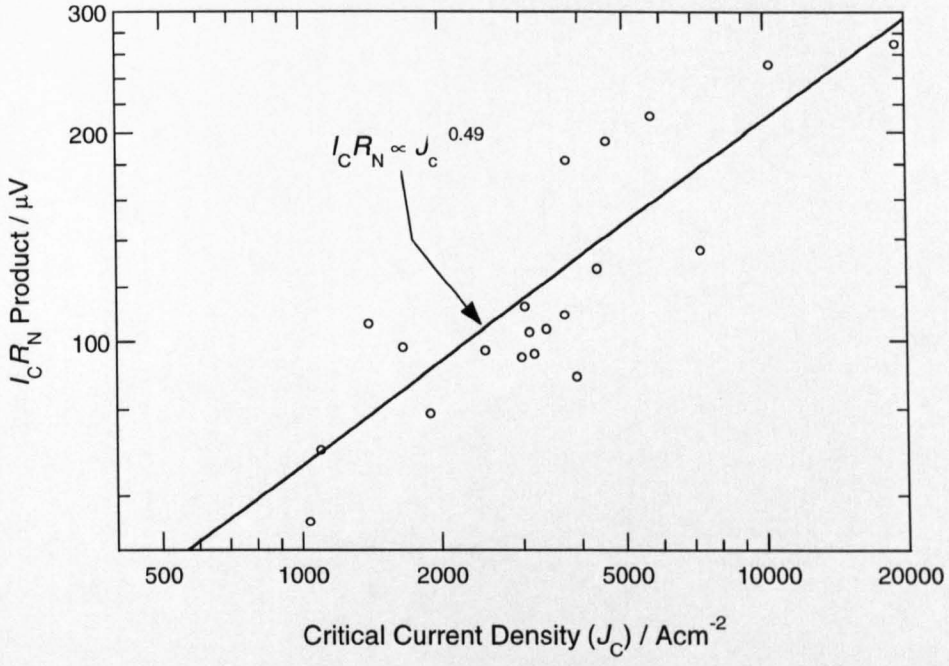

Figure 3.7: Scaling of the $I_C R_N$ product with critical current density J_C for the RSJ- like step-edge junctions. The best fit line to the data points is also shown.

with

$$I_C(B) = I_C(0) \left| \frac{\sin(\pi B/\Delta B)}{\pi B/\Delta B} \right| \tag{3.1}$$

where ΔB is the field corresponding to the first minimum in I_C.

The $I_C(B)$ dependence obtained for a 3μm-wide step-edge junction at 77K is shown in Figure 3.8. The curve resembles an ideal Fraunhofer pattern with almost complete suppression of I_C at the first minimum (the non-zero value is an indication of slight non- uniformities in the critical current distribution in the plane of the grain boundary). The ratio of the height of the central peak to that of the side peaks is smaller than one would obtain for an ideal Fraunhofer pattern. This again suggests non-uniformities in the critical current distribution, for instance the critical current could be larger at the edges of the superconducting track [30]. $I_C(B)$ curves reported in the literature are often poorer than Figure 3.8, indicating a greater degree of non-uniformity in the distribution of I_C. The curve presented here compares well with the best reported in the literature for step-edge junctions.

From Figure 3.8, ΔB was measured to be approximately 220μT. For pla-

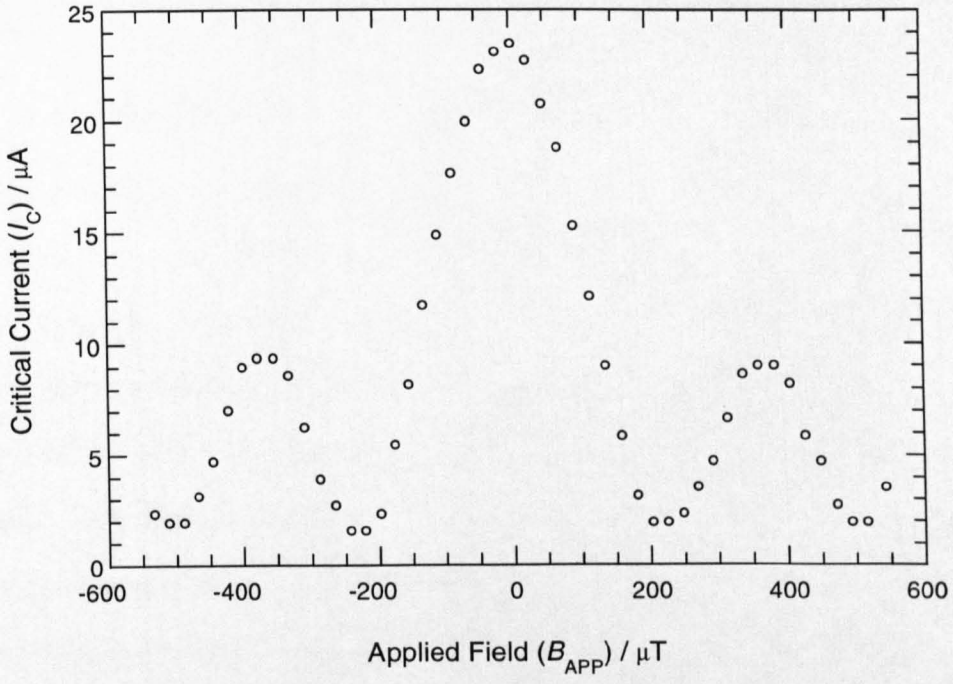

Figure 3.8: The magnetic field dependence of the critical current for a 3μm-wide RSJ-like step-edge junction at 77K.

nar, grain boundary Josephson junctions, with superconducting films of sufficient thickness such that $wt \gg {\lambda_L}^2$ where λ_L is the London penetration depth, Rosenthal *et al* predict a periodicity of $\Delta B \approx \Phi_0 t/2\alpha\lambda_L w^2$ [31] where α is a constant relating to the degree of flux-focusing of the field through the junction. Taking λ_L as $\lambda_L(T) = \lambda_L(0)/\sqrt{1-(T/T_C)^4}$ and estimating $\lambda_L(0) = 140$nm [33] gives $\lambda_L(77) = 214$nm and yields $\alpha \approx 0.51$ for the junction shown in Figure 3.8. This agrees reasonably well with the experimental work of Rosenthal *et al* reported in [31] where they measured $\alpha \approx 0.4$ for a biepitaxial junction. For Strathclyde bicrystal junctions values have been measured of $\alpha \approx 0.39$ [32] and $\alpha \approx 0.26$ [34]. All these measurements are in reasonable agreement, however factors such as the uncertainty in the estimate of λ_L, unwanted deviations from a normal orientation of the applied field relative to the plane of the grain boundary [5] and that the step-edge is a non-planar structure will affect any strict comparison.

No flux jumps [35] were observed in the $I_C(B)$ characteristics up to an applied field of 500μT. Since this is well in excess of the Earth's magnetic field, this suggests

the junctions are stable for use in SQUIDs operating in an unshielded environment.

3.4.4 Comparison with bicrystal junctions

In this section a comparison will be given between the RSJ-like step-edge junctions discussed in this chapter, and the YBCO/STO bicrystal junctions fabricated at Strathclyde [32]. The data discussed for the bicrystals comes from a sample of 67 devices fabricated on 17 different chips (12 of the substrates had a misorientation angle of 24° and the other 5 had a misorientation angle of 30°). The bicrystal chips were tested during and prior to the work presented in this thesis, with all the bicrystal junctions having widths of 2 or 3μm. Many of the bicrystal chips discussed here were fabricated and tested by C. Carr, A. Eulenburg and E.J. Romans.

For the Strathclyde bicrystals the yield of junctions showing RSJ-like characteristics is approximately 95%. This is moderately better than the yield of 85% obtained for the step-edges discussed above. Clearly for SQUID applications a high yield of junctions is desirable where one must have two working junctions to obtain a working SQUID. If it is assumed that junction failure is random, the yield figures discussed above translate to SQUID yields of 72% for step-edges and 90% for bicrystal SQUIDs. The slightly poorer yield for step-edges is not unacceptable if one considers the savings in substrate costs compared with bicrystals.

Figure 3.9 shows the measured junction parameters for the bicrystal and step-edge devices. The step-edge junctions had a mean $I_C R_N$ of 130μV with a standard deviation of 60μV. This is better than for the bicrystal junctions which have a mean $I_C R_N \approx 100\mu$V with a standard deviation of 50μV. Although a better mean $I_C R_N$ product is achieved for the step-edges, the spread in $I_C R_N$ is slightly worse. The on-chip spreads in I_C and $I_C R_N$ are also slightly poorer for the step-edges, with an average on-chip standard deviation in $I_C R_N$ of approximately 35% for the 3 step-edge chips on which 4 or more junctions were tested; for the bicrystals an average on-chip standard deviation of 24% was achieved [15]. The chip-to-chip spreads are larger than one would expect to arise from the tolerances of the fabrication techniques used;

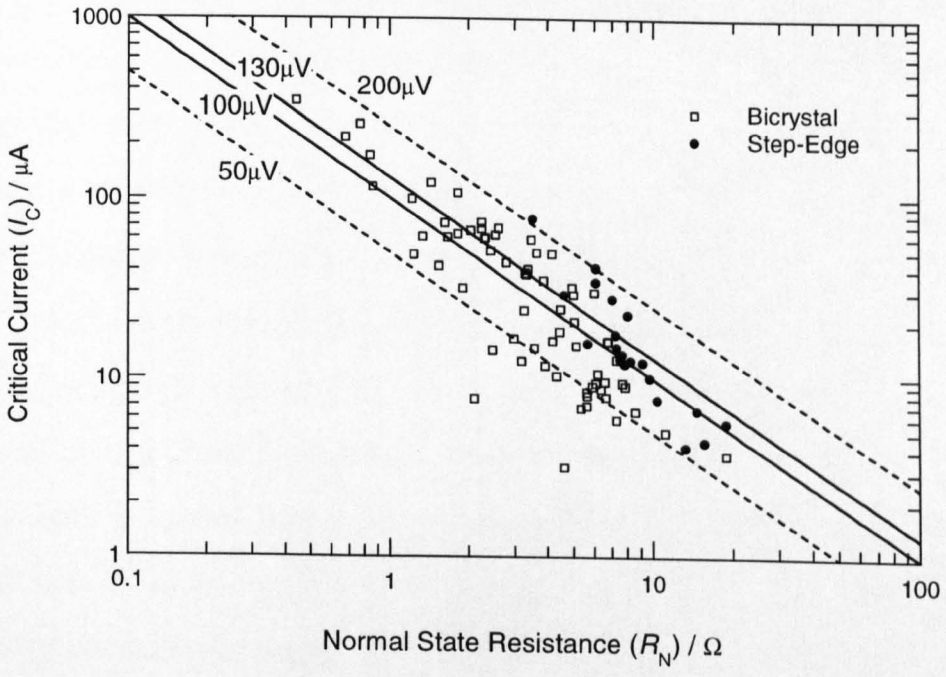

Figure 3.9: Plot showing the spreads in the junction properties I_C and R_N for the step-edge junctions (•) and the bicrystals (□). The solid lines plotted on the graph indicate the mean $I_C R_N$ products for the step-edges and bicrystals of 130μV and 100μV respectively. The two dashed lines indicate $I_C R_N$ products of 50μV and 200μV to give an idea of the spread observed for both types of junction.

both the junction width and the film thickness should vary by less than ±25% from the desired values of 2μm or 3μm and 200nm respectively. Although the spreads are larger than one might expect, they are typical of those observed by other groups for both step-edges (*e.g.* [5, 7, 36]) and bicrystals (*e.g.* [33, 37]).

3.5 Summary

As an alternative to the bicrystal junctions used at Strathclyde, a step-edge junction technology has been established and characterised.

The dependence of the junction I-V characteristics on the ratio of the film thickness to step height ratio (t/h) was studied to determine the range of step heights for which RSJ-like junctions could be obtained for 200nm thick YBCO thin films. Of the junctions fabricated on step- edges with t/h in the range of $0.59 \leq t/h \leq 0.86$, 85% of them exhibited RSJ-like I-V characteristics. These junctions had a mean

$I_C R_N$ product of 130μV with $I_C R_N$ independent of t/h. Although the spreads in $I_C R_N$ were slightly poorer for the step-edges the average $I_C R_N$ was better than that of the Strathclyde bicrystal junctions.

This scaling behaviour of the step-edge junction $I_C R_N$ product with the critical current density J_C was investigated. $I_C R_N$ was found to scale with $J_C{}^n$ where $n = 0.49$. This agrees well with many other groups who have studied the scaling relation for many types of HTS Josephson junction.

Measurements of the dependence of the junction critical current on an applied magnetic field, produced high quality Fraunhofer-like curves. The measurements indicated that there were only slight non-uniformities in the distribution of I_C in the plane of the grain boundary. The junctions were found to be stable in magnetic fields with no flux jumps observed in the $I_C(B)$ characteristics in applied fields up to approximately 500μT. Such high quality modulation characteristics are rarely reported in the literature for step-edge junctions.

This work demonstrates that by using a relatively simple fabrication procedure, high quality step-edge Josephson junctions can be produced. The performance of these junctions compares well with that of the Strathclyde bicrystals. The high $I_C R_N$ products and the demonstration of their stability in magnetic fields, suggest that the Strathclyde step-edge junctions are suitable for application in SQUIDs to be used in an unshielded environment. The performance of such devices shall be discussed in later chapters.

References

[1] A.I. Braginski in *SQUID Sensors: Fundamentals, Fabrication and Applications*, H. Weinstock (Ed.), p.235 (1996).

[2] C.L. Jia, B. Kabius, K. Urban, K. Herrmann, J. Schubert, W. Zander, A.I. Braginski and C. Heiden, Physica C 175, p.545 (1991).

[3] S. Tanaka, H. Kado, T. Matsuura and H. Itozaki, IEEE Trans. Appl. Supercond. 3, p.2365 (1993).

[4] M. Gustafsson, E. Olsson, H.R. Yi, D. Winkler and T. Claeson, Appl. Phys. Lett. 70 p.2903 (1997).

[5] K. Herrmann, G. Kunkel, M. Siegel, J. Schubert, W. Zander, A.I. Braginski, C.L. Jia, B. Kabius and K. Urban, J. Appl. Phys. 78, p.1131 (1995).

[6] C.P. Foley, S. Lam, B. Sankrithyan, Y. Wilson, J.C. Macfarlane and L. Hao, IEEE Trans. Appl. Supercond. 7, p.3185 (1997).

[7] C. Franke, M. Offner, A. Krämer, L. Mex and J. Müller, Supercond. Sci. Technol. 11, p.1311 (1998).

[8] J.A. Edwards, J.S. Satchell, N.G. Chew, R.G. Humphreys, M.N. Keene and O.D. Dosser, Appl. Phys. Lett. 60, p.2433 (1992).

[9] J.C. Nie, L. Chen, L. Li, T. Yang, M.Q. Huang, P.J. Wu, G.R. Lu and Z.X. Zhao, Supercond. Sci. Technol. 9, p.1087 (1996).

[10] J. Luine, J. Bulman, J. Burch, K. Daly, C. Pettiette- Hall and S. Schwarzbek, Appl. Phys. Lett. 61, p.1128 (1992).

[11] J.Z. Sun, W.J. Gallagher, A.C. Callegari, V. Foglietti and R.H. Koch, Appl. Phys. Lett. 63, p.1561 (1993).

[12] H.R. Yi, D. Winkler, Z.G. Ivanov and T. Claeson, IEEE Trans. Appl. Supercond. 5, p.2778 (1995).

[13] *Past visiting research at Strathclyde from the Institue of Physics, Czech Academy of Sciences, Prague.*

[14] P. Tavares, *High Temperature Superconductor Josephson Vortex Flow Transistors*, PhD thesis, University of Strathclyde, (2001).

[15] A. Eulenburg, *High Temperature Superconducting Thin Films and Quantum Interference Devices (SQUIDs) for Gradiometers*, PhD thesis, University of Strathclyde, (1999).

[16] M.S. Colclough *Presented at the UK-SQUID meeting*, Cambridge, (1998).

[17] J. Clarke and R.H. Koch, Science 242. p.217 (1988).

[18] F. Schmidl, L. Alff, R. Gross, K.D. Husemann, H. Schneidewind and P. Seidel, IEEE Trans. Appl. Supercond. 3, p.2349 (1993).

[19] M. Vaupel, G. Ockenfuss and R. Wördenweber, Appl. Phys. Lett. 85, p.3623 (1996).

[20] D. Koelle, R. Kleiner, F. Ludwig, E. Dantsker and J. Clarke, Rev. Mod. Phys. 71, p.631 (1999).

[21] K. Herrmann, Y. Zhang, H.M. Mück, J. Schubert, W. Zander and A.I. Braginski, Supercond. Sci. Technol. 4, p.583 (1991).

[22] C.P. Foley, E.E. Mitchell, S.K.H. Lam, B. Sankrithyan, Y.M. Wilson, D.L. Tilbrook and S.J. Morris, IEEE Trans. Appl. Supercond. 9, p.4281 (1999).

[23] R. Gross, P. Chaudhari, M. Kawasaki and A. Gupta, Phys. Rev. B 42, p.10735 (1990).

[24] K. Char, M.S. Colclough, S.M. Garrison, N. Newman and G. Zaharchuk, Appl. Phys. Lett. 59, p.733 (1991).

[25] J. Gao, Y. Boguslavskii, B.B. Klopman, D. Terpstra, G.J. Gerritsma and H. Rogalla, J. Appl. Phys. 72 p.575 (1992).

[26] R.B. Laibowitz, J.Z. Sun, V. Foglietti, W.J. Gallagher and R.H. Koch, Appl. Phys. Lett. 64, p.247 (1994).

[27] R. Gross. L. Alff, A. Beck, O.M. Froehlich, D. Koelle and A. Marx, IEEE Trans. Appl. Supercond. 7, p.2929 (1997).

[28] C.D Tesche and J. Clarke, J. Low Temp. Phys. 29, p.301 (1977).

[29] J.C. Gallop, *SQUIDs, the Josephson Effects and Superconducting Electronics* Adam Hilger (1991).

[30] A. Barone and G. Paterno, *Physics and Applictaions of the Josephson Effect* Wiley-Interscience (1982).

[31] P.A. Rosenthal, M.R. Beasley, K. Char, M.S. Colclough and G. Zaharchuk, Appl. Phys. Lett. 59, p.3482 (1991).

[32] E.J. Romans, T.G. Henrici, C. Carr, J.C. Macfarlane, C.M. Pegrum and G.B. Donaldson, IEEE Trans. Appl. Supercond. p.2530 (1997).

[33] D. Winkler, Y.M. Zhang, P.A. Nilsson, E.A. Stepantsov and T. Claeson, Phys. Rev. Lett. 72, p.1260 (1994).

[34] C. Carr, *High Temperature Superconducting Quantum Interference Devices for Nondestructive Evaluation* , PhD thesis, University of Strathclyde, (1997).

[35] C.P. Foley, G.J. Slogget, K.-H. Muller, S. Lam, N. Savvides, A. Katsaros and D.N. Matthews, IEEE Trans. Appl. Supercond. 5, p.2805 (1995).

[36] E.E. Mitchell, C.P. Foley, K.H. Muller, K. Leslie and D. Tilbrook, IEEE Trans. Appl. Supercond. 9, p.2997 (1999).

[37] A.H. Miklich, D. Koelle, E. Dantsker, D.T. Nemeth, J.J Kingston, R.F. Kromann and J. Clarke, IEEE Trans. Appl. Supercond. 3, p.2434 (1993).

Chapter 4

Step-edge SQUIDs

This chapter focuses on the characterisation and performance of autonomous step-edge junction SQUIDs. After describing the motivation for this work, a section details the design and fabrication of the step-edge SQUIDs, and includes discussion on the calculation of the SQUID inductance L_{SQ}. This section also describes the Josephson junction characteristics that are required for use in HTS SQUIDs, with reference to the relevant findings of Chapter 3. The following section focuses on the electrical characteristics of the step-edge SQUIDs, including details of the measured I-V and V-Φ curves, inductance measurements, the maximum voltage modulation depth ΔV and the SQUID noise performance. The final section compares the performance of the step-edge SQUIDs with that of 24° bicrystal SQUIDs fabricated at Strathclyde.

4.1 Introduction

4.1.1 Motivation

The previous chapter described the step-edge Josephson junction technology established during the early stages of the present work. The Josephson junction is the critical element of the SQUID, and in this chapter the characterisation and performance of SQUIDs incorporating step-edge junctions will be described. In the context of the work described in this thesis, this is most important from a fundamental point of view, as the intrinsic noise of an optimised SQUID typically determines the noise floor of a magnetometer or gradiometer into which it is incorporated. Autonomous SQUIDs are however still important from a practical view point, in particular for applications that require high spatial resolution such as magnetic microscopy [1].

The most widely used type of autonomous SQUID is the square washer SQUID developed by Ketchen and Jaycox [2, 3]. The best magnetic field sensitivity for an autonomous HTS SQUID was achieved using a large solid washer design by Koelle *et al.* [4] who measured a magnetic field noise of $150\text{fT}/\sqrt{\text{Hz}}$ at 1kHz. However when cooled in the Earth's field, the $1/f$ noise in such devices is generally high due to the motion of flux vortices in the large washer structure. In addition, the field sensitivity of autonomous SQUIDs is limited by the requirement to keep the SQUID inductance low in order to minimise the intrinsic magnetic flux noise (see discussion in Section 1.4 of Chapter 1).

The aim of the work described in this chapter was to develop low noise SQUID based sensors for use in an unshielded environment - the focus was not on achieving the best field sensitivity possible for an autonomous device, but instead on developing SQUIDs that are suitable for incorporation in directly coupled devices, particularly single-layer gradiometers (see next chapter). All the SQUIDs discussed in this chapter are of the conventional narrow-linewidth type (introduced in Chapter 1) which are best suited for application in directly coupled devices.

It should be noted that the SQUID data discussed in this chapter is not only from measurements of autonomous devices but also from SQUIDs incorporated into single-layer gradiometers (SLGs). All of the measurements were taken inside sufficient levels of shielding to prevent the direct pick-up of environmental interference by the SQUID (and by the pick-up loops for the SLG devices) from significantly perturbing the measurement of the intrinsic SQUID characteristics.

4.2 Design and Fabrication

4.2.1 Junction requirements

Low noise SQUIDs require high quality, non-hysteretic resistively shunted Josephson junctions. In addition the junctions should have sufficient coupling energy so the junction noise parameter $\Gamma < 0.2$ [5] (see Equation 1.8 and discussion in Chapter 1).

For HTS devices operating at 77K this implies that the junction critical current I_C should be greater than approximately 16μA. To achieve a reasonable flux sensitivity and to effectively couple the signal from the pick-up loops to the SQUID it is desirable that the SQUID inductance L_{SQ} is in the range 50-120pH. For this reason, junctions with a relatively large critical current are undesirable as the SQUID noise performance is optimised for a screening parameter ($\beta_L = 2L_{SQ}I_C/\Phi_0$) of order unity. The critical currents measured for the twenty RSJ-like junctions discussed in Chapter 3 yield a mean critical current density $J_C \approx 4.4\text{A/cm}^2$. This translates to a mean junction critical current per unit junction width of approximately 8.8μA/μm, taking the film thickness as 200nm and assuming that J_C is uniform. For junctions of width $w = 2\mu$m this implies that $I_C \approx 17.6\mu$A which is close to the minimum required to meet the condition that $\Gamma < 0.2$. More significantly the spread in I_C is such that many of the 2μm junctions discussed in the previous chapter have $I_C < 16\mu$A (see Figure 3.5(a)). For this reason the SQUID designs discussed in this chapter, developed for use with step-edges, have a junction width of 3μm, for which the data from the previous chapter implies that an average critical current of 26.4μA should be expected.

4.2.2 SQUID inductance

The inductance of a SQUID L_{SQ} is related to its geometrical structure and the film thickness. By considering the SQUID to be composed of separate elements, simple expressions can be used to estimate the inductance of the SQUID. For example, the inductance of the square washer SQUID shown in Figure 4.1(a) can be regarded as having three components $L_{SQ} \approx L_H + L_S + L_J$, where L_H is the inductance of the central square hole in the washer of side d, L_S is the inductance of the slit of length l_S and L_J is the inductance of the junction striplines of length l_J and width w. The hole inductance can be calculated using an expression given by Ketchen valid in the limit $D \gg 3d$ [6]:

$$L_H = 1.25\mu_0 d. \tag{4.1}$$

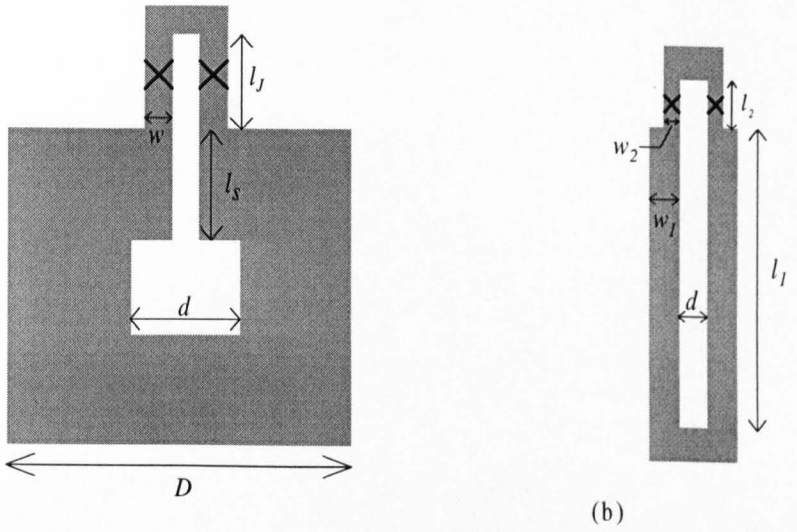

Figure 4.1: Schematic representations of (a) a square washer SQUID design and (b) a narrow-linewidth SQUID design.

The slit inductance can be approximated as [6]

$$L_{\mathrm{S}} \approx 0.6\mu_0 l_{\mathrm{S}}. \tag{4.2}$$

The large line-width of the SQUID washer results in negligible contribution to L_{H} and L_{S} from their kinetic inductances. In contrast the self inductance of the junction striplines is dominated by their kinetic inductance. The self inductance of the junction striplines, approximated as the kinetic inductance, is given by [7]

$$L_{\mathrm{J}} = 1.25 \times 10^{-6} \frac{2 l_{\mathrm{J}} \lambda_{\mathrm{L}}^2}{tw}, \tag{4.3}$$

where t is the thickness of the film and λ_{L} is the magnetic penetration depth.

The inductance of the narrow-linewidth SQUID shown in Figure 4.1(b) can be approximated as the sum of the contribution from the self inductance of the slit (of length $l = l_1 + l_2$) and the kinetic inductances. The slit's self inductance is more accurately estimated using the the standard inductance formula for co-planar striplines [8, 9]. The total slit self inductance is split into two parts $L_{\mathrm{S}} = L_1 + L_2$, where L_1 is the self inductance of slit striplines forming the lower part of the SQUID

loop of length l_1, and L_2 is the self inductance of the junction striplines of length l_2. The inductance of each of these components can then be estimated using

$$L_i = \mu_0 \frac{\mathrm{K}(k_i)}{\mathrm{K}'(k_i)} l_i, \tag{4.4}$$

where l_i is the length of each part of the slit, $k_i = d/(d + 2w_i)$ with d the distance between the superconducting striplines of width w_i and $i = 1, 2$. K is the complete elliptical integral of the first kind and K′ is the complementary function $\mathrm{K}' = \mathrm{K}(1 - {k_i}^2)$. The ratio $\mathrm{K}(k_i)/\mathrm{K}'(k_i)$ can be approximated as

$$\frac{\mathrm{K}(k_i)}{\mathrm{K}'(k_i)} = \left[\frac{1}{\pi}\ln\left(2\frac{1+\sqrt{k_{ci}}}{1-\sqrt{k_{ci}}}\right)\right]^{-1}, \tag{4.5}$$

providing that $0.7 \leq k_{ci} \leq 1$ where $k_{ci} = \sqrt{(1 - {k_i}^2)}$. The restriction on the limits of k_{ci} translates to the approximate condition that $w_i > d/2$. Note that in the case of the narrow-linewidth SQUID, the contribution from the kinetic inductance of the lower loop with strips of width w_2 is significant as well as that of junction striplines. The kinetic inductance of junction striplines and the lower loop can again be estimated using Equation 4.3.

The inductances of the SQUIDs discussed in this chapter were also modeled using the public domain finite element modeling package FASTHENRY [10] - originally developed to calculate the inductances for normal metals [11], but subsequently modified to treat superconductors [12]. FASTHENRY divides the superconductor into filaments of rectangular cross-section. The inductance of each filament is calculated and iteratively combined to compute the inductance being modeled. The computed inductance includes the kinetic inductance contributions.

One of the advantages of calculating inductances using a package like FASTHENRY, is the ability to model the effect of connections to the SQUID on its inductance. In addition mutual inductances between the SQUID and nearby superconducting tracks can be calculated. However, note that whether one calculates the

inductance using FASTHENRY, or using the simple stripline model (Equations 4.3-4.5), the calculation of the contribution from the kinetic inductance is dependent on the magnetic penetration depth $\lambda_L(T) = \lambda_L(0)/\sqrt{1-(T/T_C)^4}$. Wide variations in the quoted values of $\lambda_L(0)$ and a lack of understanding of the exact nature of λ_L at temperatures approaching T_C mean that the magnetic penetration depth can only be estimated. In addition likely variations λ_L along the edges of the sample, where damage and significant oxygen losses from the HTS film may occur, contribute to the uncertainty in the contribution from the kinetic inductance. For consistency, throughout this thesis the penetration depth has been taken as $\lambda_L(0) = 140$nm [13], which yields $\lambda_L(77) = 214$nm.

The SQUID design shown in Figure 4.2(a) was modeled using FASTHENRY. The effects of the bias (I) and voltage (V) connections, and the connections used to inject current I_M to modulate the SQUID are included in the modeled SQUID inductance L_{SQ} shown in Figure 4.2(b) as a function of the slit length l_1 for a film thickness of $t = 200$nm and penetration depth of $\lambda_L = 214$nm. The modeled SQUID inductance as a function of λ_L for a fixed slit length of $l_1 = 70\mu$m is shown in Figure 4.2(c). This illustrates how the uncertainty in estimating the penetration depth results in difficulties in accurately obtaining a value for the SQUID inductance.

4.2.3 SQUID designs

Four designs of narrow-linewidth SQUID were fabricated and tested (denoted as SQ1, SQ2, SQ3 and SQ4). All the designs were similar to that shown in Figure 4.2(a). Three of these were designed during the course of the present work (SQ2, SQ3 and SQ4). These three designs all incorporate junctions of width 3μm and have a maximum SQUID loop linewidth of 4μm to minimise the $1/f$ flux noise associated with flux penetration when the device is cooled in the Earth's field. The design (SQ1) which was developed at Strathclyde before the present work, was originally for use with bicrystal junctions. This design incorporates junctions of width 2μm (the Strathclyde bicrystal junctions have a slightly larger J_C than the step-edges)

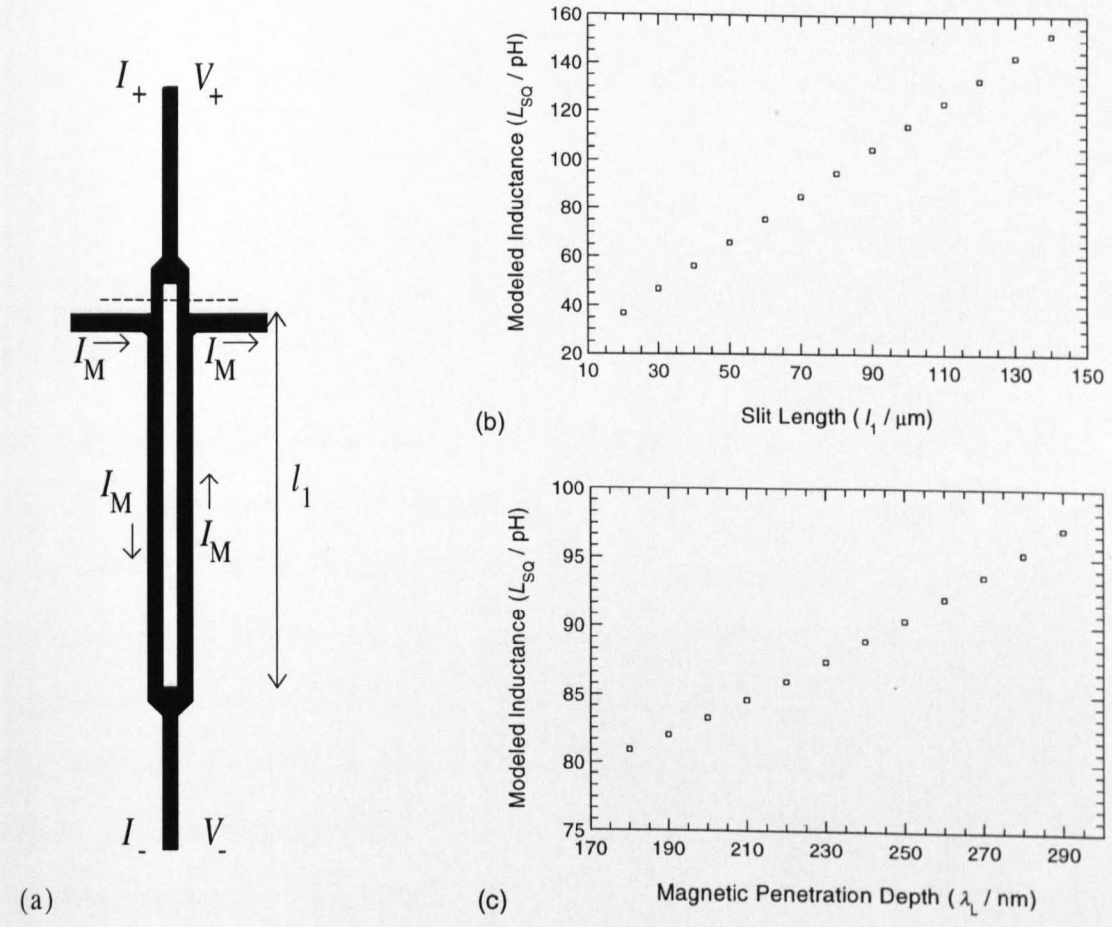

Figure 4.2: (a) The SQUID design being modeled showing the connections to the SQUID described in the main text and the path of the injected modulation current I_M. (b) The modeled SQUID self inductance as a function of l_1 for $\lambda_L = 214$nm. (c) The modeled SQUID self inductance as a function of λ_L for a $l_1 = 70\mu$m.

and has a maximum SQUID loop linewidth of 5μm. All four SQUID designs have slight variations in the structure of the IV and modulation current connections. Table 4.1 details the dimensions of each design corresponding to the labeled geometrical parameters shown in Figure 4.1(b). The values calculated for the self inductance of each SQUID design, using FASTHENRY and the stripline model (Equations 4.3-4.5) are included in the table. Note that with FASTHENRY the SQUID inductance includes any effect from the various connections to the SQUID while the stripline model neglects the effect of these connections.

4.2.4 Fabrication

The SQUIDs discussed in this chapter were fabricated from masks designed to be compatible for use with bicrystals as well as step-edges. A single straight step-edge

Design	d (μm)	w_1 (μm)	l_1 (μm)	w_2 (μm)	l_2 (μm)	L_{SQ} (S-L) (pH)	L_{SQ} (F-H) (pH)
SQ1	3	5	60	2	8	65	70
SQ2	4	4	64	3	7	67	67
SQ3	4	4	90	3	8	106	105
SQ4	4	4	100	3	8	116	114

Table 4.1: Geometrical dimensions and SQUID inductance calculated using FASTHENRY L_{SQ} (F-H) and the stripline model L_{SQ} (S-L) for the four SQUID designs. The magnetic penetration depth was taken as λ_L = 214nm.

was fabricated across the centre of each 10 × 10mm^2 single crystal STO substrate using the procedure described in Section 3.2. The step height h on each substrate was in the range of 240 to 330nm thus yielding a t/h ratio (where t = 200nm is the film thickness) within the regime required to obtain RSJ-like Josephson junctions as described in Section 3.4.1. The YBCO films were grown using PLD and patterned using standard photolithography and argon ion milling as described in Chapter 2. Gold films were deposited and patterned into contact pads before the substrates were wire bonded to PCBs to be tested.

4.3 SQUID Characterisation

The electrical properties of the step-edge SQUIDs are described in this section. For each device the I-V and V-Φ curves were measured, the SQUID bias current was optimised to measure the maximum voltage modulation depth ΔV and the SQUIDs were operated in a flux-locked loop inside shielding to measure their intrinsic flux noise. The characterisation methods and results from these measurements are considered below.

4.3.1 I-V measurements

The I-V characteristics of the SQUIDs were measured in liquid nitrogen in an aluminum dewar, inside a single mu-metal shield. The procedure used to measure the SQUID I-V curves was the same as that used to measure the step-edge junctions discussed in the previous chapter (described in Section 3.3). The SQUID's junction

	Junction width	No. of samples	Mean I_C (μA)	Mean R_N (Ω)	Mean $I_C R_N$ (μV)
SQUIDs	3	12	32.9	4.89	153
	2	11	15.6	9.13	117
Junctions	2	17	17.2	9.29	128

Table 4.2: Junction parameters measured for 12 SQUIDs with 3μm wide junctions, 11 SQUIDs with 2μm wide junctions and the 17 discrete 2μm junctions discussed in Chapter 3.

parameters I_C and R_N were taken as half and double the total SQUID critical current and normal state resistance respectively, and were extracted using the RSJ curve fitting procedure described in Section 3.3.3. The junction critical current densities and normal state resistivities for the SQUIDs are broadly similar to those measured for the step-edge junctions discussed in Chapter 3. As expected, the SQUIDs incorporating junctions of width 3μm generally had a higher I_C than was found for the junctions in the previous chapter, which mostly had a width of just 2μm. Table 4.2 shows the mean values obtained for the junction properties I_C, R_N and $I_C R_N$ of the SQUIDs incorporating 2μm and 3μm junctions and includes for comparison, the data for the 2μm junctions from the previous chapter.

The mean I_C of the eleven 2μm junction SQUIDs of 15.6μA is close to that obtained for the 2μm junctions as expected. It is however, slightly below the minimum I_C of 16μA required to maintain sufficient Josephson coupling (*i.e.* $\Gamma < 0.2$). The mean I_C of the 3μm junction SQUIDs of 32.9μA is significantly above the minimum required to obtain $\Gamma < 0.2$. Of the twelve 3μm junction SQUIDs, only one had an I_C below 16μA. As discussed in Section 4.2.1, from the junction data discussed in Chapter 3, a mean critical current of 26.4μA is expected for 3μm junctions. The fact that the mean obtained here is higher than this suggests that the critical current density is non-uniform across the junction (85% of the discrete junctions discussed in the previous chapter had a width of just 2μm). In addition, this larger than expected I_C may be a consequence of the continued refinements to the step-edge fabrication procedure resulting in a better quality of junction (the 3μm SQUIDs were generally fabricated some time after the 2μm devices) - the improved $I_C R_N$ product of the 3μm SQUIDs also supports this view.

4.3.2 V-Φ measurements

All of the SQUIDs discussed in this chapter exhibited periodic voltage modulation as a function of applied flux when at constant bias $I_B > 2I_C$. The SQUIDs were cooled in liquid nitrogen in the aluminum dewar inside a mu-metal shield, as for the I-V measurements. Flux was coupled to the SQUID by direct current injection through the SQUID loop with the modulation current I_M flowing through the lower section of the SQUID loop as shown in Figure 4.2(a). An HP-3245A universal source swept the injected modulation current I_M over a designated range. The voltage across the SQUID was amplified by a factor of 1000 and low-pass filtered with a 3dB cut-off at 30Hz using an EG&G amplifier. The amplified and filtered voltage output of the SQUID was recorded as a function of I_M using an HP-3458 multimeter and the Kuznik program (introduced in Section 3.3). The SQUID bias current I_B was varied for each sweep of I_M to obtain the maximum peak-to-peak voltage modulation depth ΔV for each device. Figure 4.3 shows the sinusoidal-like V-Φ curves obtained for one of the SQ2 design SQUIDs for various bias currents. A maximum modulation depth of $\Delta V \approx 14\mu$V was obtained for this device at a bias current of $I_B = 50\mu$A.

The inductance through which I_M couples flux to the SQUID can be measured from the V-Φ curve. For each period ΔI_M one flux quantum Φ_0 is coupled to the SQUID via the modulation coupling inductance. This modulation coupling inductance is thus given by $L_M = \Phi_0/\Delta I_M$. This inductance can also be calculated using FASTHENRY or by using the stripline model introduced in Section 4.2.2. Table 4.3 compares the mean measured value of L_M for each of the four SQUID designs with the calculated values. The inductances predicted by FASTHENRY and the stripline model are in reasonable agreement with the measured values considering the uncertainty in the estimate of λ_L. In the discussion below (and in Chapter 5 where the same SQUID designs are used in SLGs), unless otherwise stated, the quoted SQUID inductance and the value used in calculations shall be the value calculated by FASTHENRY given in Table 4.1.

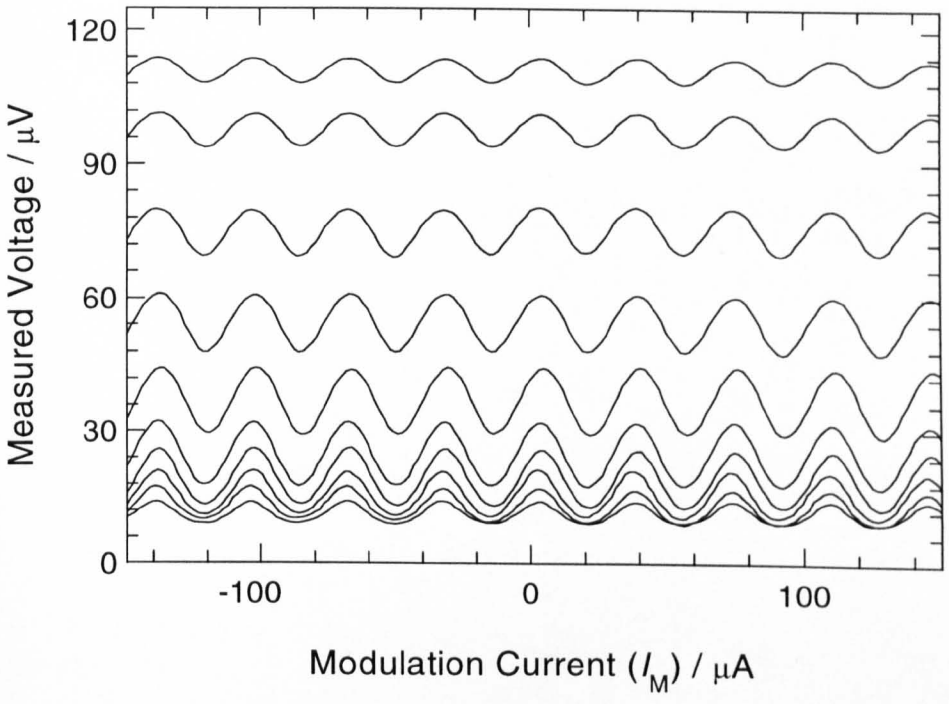

Figure 4.3: Set of V-Φ curves obtained for a step-edge SQUID (SQ2 design), for 2μA increments in the bias current starting at 40μA (lower curve).

For perfect sinusoidal modulation the SQUID transfer function V_Φ is related to the peak-to-peak modulation depth by $\Delta V = V_\Phi \Phi_0/\pi$. From Equation 1.15 it can be seen that a large modulation depth is desirable to minimise the intrinsic white flux noise of the SQUID. In addition a large voltage modulation depth improves the stability of the SQUID for unshielded operation. The analytical expression derived by Enpuku *et al.* for the maximum voltage modulation depth was given in Chapter 1 (see Equation 1.13). Figure 4.4 compares the measured value of the maximum modulation depth with the value predicted by Equation 1.13, where I_C and R_N are taken from the measured I-V curves and L_{SQ} is taken as the value calculated by FASTHENRY. A straight line fit to the data suggests a general tendency to measure

L_M /pH	SQ1	SQ2	SQ3	SQ4
Stripline	54	58	97	108
FASTHENRY	51	56	88	101
Measured	46	57	90	104

Table 4.3: Comparison between the measured values of the modulation inductance L_M for each SQUID design, and the values predicted by the stripline model and FASTHENRY.

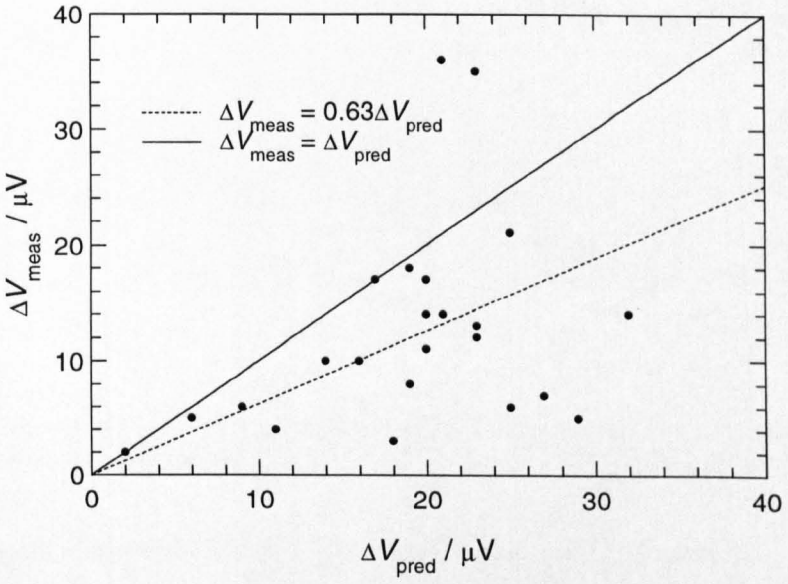

Figure 4.4: Comparison between the measured maximum voltage modulation depth ΔV_{meas} and that predicted by Enpuku et al. ΔV_{pred} (calculated using Equation 1.13), for 23 step-edge SQUIDs. The dotted line shows the best straight line fit to the data yielding $\Delta V_{\text{meas}} = 0.63\Delta V_{\text{pred}}$. The solid line shows $\Delta V_{\text{meas}} = \Delta V_{\text{pred}}$.

about 63% of the predicted value of ΔV. There is however a large spread in the data - the two designs from which nine or more SQUIDs were fabricated (SQ1 and SQ2) both have standard deviations in their mean ΔV values of approximately 9μV. Other groups observe similar behaviour for their SQUIDs (not necessarily step-edge SQUIDs), typically measuring a large spread in ΔV that is typically 40-70% of the predicted value [14] [15] as discussed in Section 1.3.2 of Chapter 1.

Given the spreads in the junction critical currents and normal state resistances discussed in Chapter 3, one significant cause of measuring a lower ΔV than expected is likely to be asymmetries between the parameters of the two junctions in the SQUID [16]. The measured V-Φ curves typically show deviations from the perfectly sinusoidal modulation assumed by Enpuku *et al.* [17] (see Figure 4.3), which is also likely to contribute to measuring a lower ΔV than expected. A significantly larger than expected voltage modulation of 35 and 36μV was measured for two of the SQUIDs, as shown in Figure 4.4. The RSJ-fit to the I-V characteristics of these devices was poor. A comparison between SQUIDs with good RSJ and poor RSJ fits is shown in Figure 4.5. Figure 4.5(a) shows a region of a RSJ-like I-V curve from

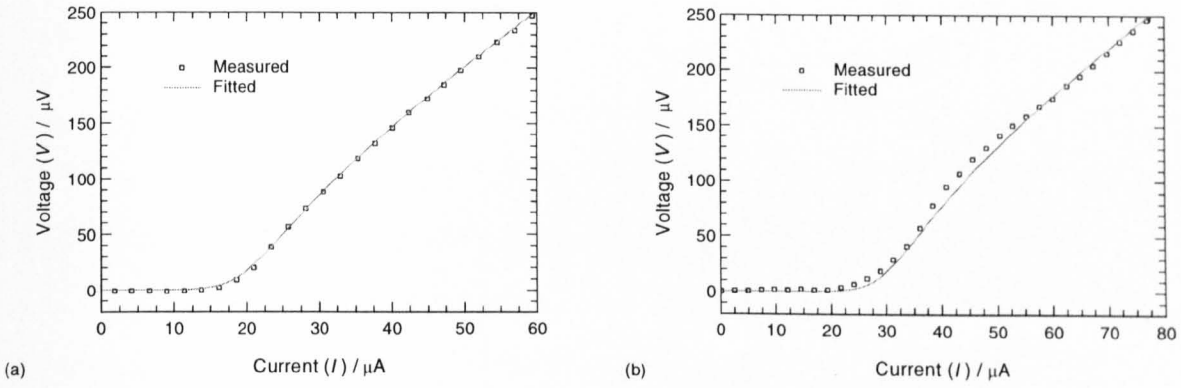

Figure 4.5: I-V curves of two step-edge junction SQUIDs showing (a) a good fit to the RSJ-model, and (b) a poor fit to the RSJ-model.

one of the typical step-edge SQUIDs - the measured data and the noise rounded RSJ-fit to the data (obtained using the program described in Section 3.3.3) are shown. There is a good fit between the measured data and the fitted RSJ curve. This device had a maximum modulation depth of $\Delta V = 13\mu$V, approximately 57% of the predicted value. Figure 4.5(b) shows the measured data and fitted noise rounded RSJ curve for one of the SQUIDs with a high ΔV. The fit to this data was poor, with the measured I-V characteristics clearly exhibiting a larger dynamic resistance $R_{\rm dyn} = \partial V/\partial I$ just above $I_{\rm C}$, than predicted by the RSJ-model - note from the curves plotted in Figure 4.5 that both SQUIDs had a similar $I_{\rm C}$. The SQUID with a poor RSJ-fit exhibited a voltage modulation of 35μV, approximately 152% of the predicted value. The larger than expected ΔV is a consequence of the SQUID having a larger than expected dynamic resistance. Similar observations were made for the SQUID which had a maximum modulation depth of 36μV. This phenomenon has been observed in bicrystal devices as well, and is most common in 30° bicrystal SQUIDs [18, 19]. The physical origin of the larger than expected $R_{\rm dyn}$ and the corresponding large ΔV is clearly related to the current transport across the grain boundary although the mechanism of this phenomenon is currently not understood.

4.3.3 Noise Measurements

To measure their intrinsic flux noise at 77K, the SQUIDs were operated in a flux locked looped (FLL) as described in Section 1.3.1 using Conductus PC-100 electronics. The devices were cooled inside three concentric layers of mu-metal (*i.e.* in nominally zero dc field), in a liquid nitrogen glass fibre cryostat. Several different probes were used to measure the SQUID noise characteristics, all incorporating RF screening and individually screened sets of twisted pairs to prevent crosstalk. The output from the (FLL) was recorded using a HP-3561 dynamic signal analyser.

Typically, the flux noise of each SQUID was measured over a 1kHz bandwidth from 1Hz using both dc and ac-bias (Section 1.3.2 explained how the use of the ac-bias scheme suppresses $1/f$ noise). With dc-bias the onset of $1/f$ noise was typically somewhere in the 10-100Hz range, and generally it was found that the lower the intrinsic white noise of the device, the higher the frequency at which $1/f$ noise became apparent as one would expect. The $1/f$ noise was generally suppressed down to the lowest measured frequency of 1Hz using ac-bias, as one would expect for a zero-field cooled narrow-linewidth SQUID fabricated from a high quality YBCO thin film. Figure 4.6 shows the flux noise spectra measured for a typical step-edge SQUID, recorded using both dc and ac-bias. The plot shows the flux noise measured between 1Hz and 100Hz - between 100Hz and 1kHz the measured flux noise was white for both ac and dc-bias.

Figure 4.7 shows the white flux noise measured for each SQUID as a function of the screening parameter β_L. Almost all of the 23 step-edge SQUIDs exhibited an intrinsic white flux noise in the 10-30$\mu\Phi_0/\sqrt{\text{Hz}}$ range. Unfortunately the large voltage modulation depth measured for the two devices with high dynamic resistances (larger than predicted by the RSJ-model) did not result in an exceptionally low flux noise - the two SQUIDs had a white flux noise of 23$\mu\Phi_0/\sqrt{\text{Hz}}$ and 25$\mu\Phi_0/\sqrt{\text{Hz}}$. This is in agreement with measurements performed on 30° bicrystal SQUIDs at Strathclyde where a larger than expected ΔV does not result in particular good noise performance [20]. Similar results have also been reported in the literature by others

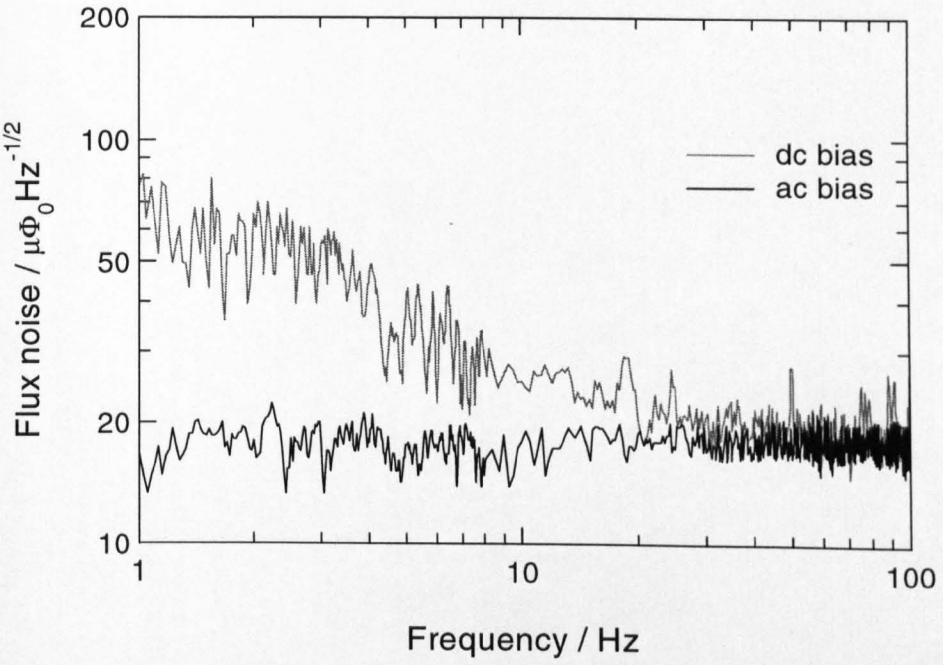

Figure 4.6: Shielded flux noise spectra recorded for a typical step-edge SQUID using ac and dc bias. The curves meet at approximately 50Hz. *With ac bias the noise is flat over the entire measured frequency range, down to* 1Hz.

[18, 21]. An exception to this is the work of Beyer *et al.* [19]. Their 30° bicrystal devices have a high ΔV and low noise performance. In contrast with the other work reported in the literature, the films used by Beyer *et al.* were grown by magnetron sputtering rather than by PLD.

Two of the step-edge SQUIDs had a considerably poorer intrinsic white flux noise than the others, measured as $50\mu\Phi_0/\sqrt{\text{Hz}}$ and $46\mu\Phi_0/\sqrt{\text{Hz}}$ respectively. The $46\mu\Phi_0/\sqrt{\text{Hz}}$ device (a 105pH SQUID) exhibited a much smaller than expected ΔV, probably a consequence of highly asymmetric junction properties, and in addition had a large I_C of 51μA which gave rise to a large β_L of 5.2. A combination of a small ΔV and large β_L contribute to the high flux noise measured for this device. The $50\mu\Phi_0/\sqrt{\text{Hz}}$ SQUID, which had an inductance of 114pH, also exhibited weak voltage modulation of $\Delta V = 2\mu$V. This was however close to that predicted by Equation 1.13. This device had a poor $I_C R_N$ of just 10μV, which resulted in the small ΔV and corresponding high noise that was measured for this device. From Figure 4.7 it can be seen that there is a very weak trend in observing a lower flux

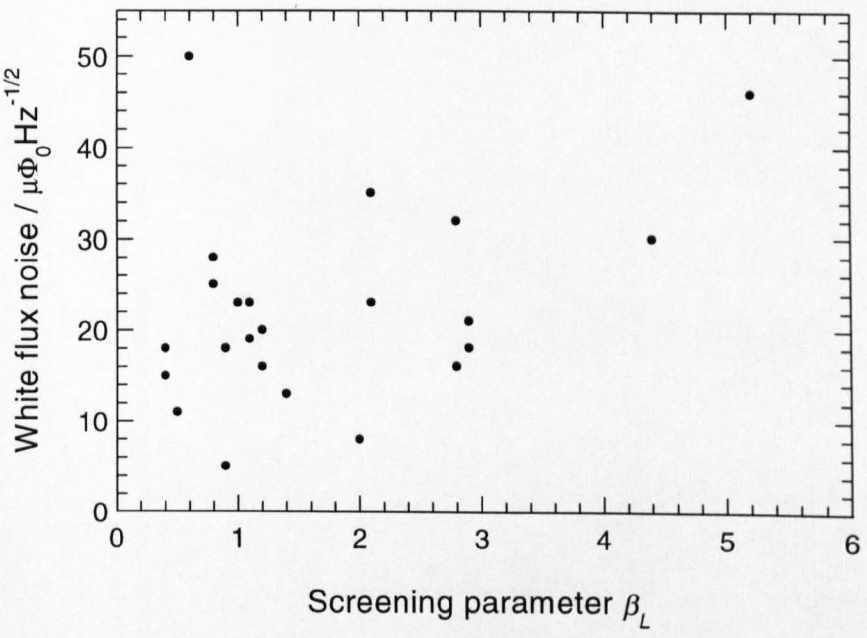

Figure 4.7: Intrinsic white flux noise measured for each of the 23 step-edge SQUIDs, shown versus the screening parameter β_L.

noise in SQUIDs with a screening parameter of $\beta_L \sim 1$. The large spread in the measured data as a function of β_L is similar to that found by Koelle *et al.* in their recent study [14]. In common with their analysis, the white noise data from the step-edge SQUIDs discussed here showed no clear correlation with the junction properties, I_C, R_N and $I_C R_N$, or with the SQUID inductance L_{SQ}.

Four of the 23 SQUIDs had an intrinsic white flux noise of $13\mu\Phi_0/\sqrt{\text{Hz}}$ or better, with the best device, a 70pH SQUID, exhibiting a white noise of just $5\mu\Phi_0/\sqrt{\text{Hz}}$. This excellent performance compares well with the lowest flux noise reported for a step-edge SQUID of similar inductance of $2.5\mu\Phi_0/\sqrt{\text{Hz}}$ [22]. The parameters of the four best step-edge SQUIDs are summarised in Table 4.4. The measured flux

L_{SQ} (pH)	I_C (μA)	R_N (Ω)	β_L	ΔV_{meas} (μV)	ΔV_{pred} (μV)	$\sqrt{S_\Phi}_{meas}$ ($\mu\Phi_0/\sqrt{\text{Hz}}$)	$\sqrt{S_\Phi}_{pred}$ ($\mu\Phi_0/\sqrt{\text{Hz}}$)
70	12.8	7.6	0.9	18	19	5	6.4
70	29.2	4.6	2.0	17	17	8	5.3
70	8.0	10.4	0.5	17	20	11	7.9
67	22.1	6.2	1.4	14	21	13	7.4

Table 4.4: Parameters of the four SQUIDs exhibiting the lowest flux noise in the white region. The predicted flux noise was calculated using Equation 1.15 with V_Φ obtained using ΔV_{meas}.

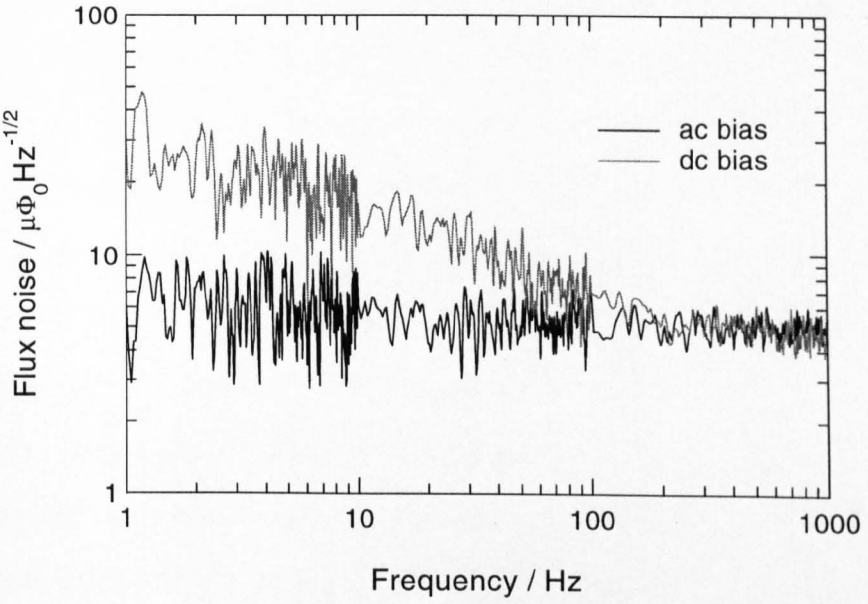

Figure 4.8: Flux noise spectra measured for the step-edge SQUID which exhibited the lowest intrinsic flux noise of approximately $5\mu\Phi_0/\sqrt{\text{Hz}}$ in the white region. Noise spectra are shown for both ac and dc bias.

noise $\sqrt{S_{\Phi\text{meas}}}$ is compared with the predicted flux noise $\sqrt{S_{\Phi\text{pred}}}$ calculated using Equation 1.15 and the measured transfer function (*i.e.* $V_{\Phi\text{meas}} = \pi\Delta V_{\text{meas}}/\Phi_0$). The flux noise spectrum measured for the best SQUID is shown in Figure 4.8.

4.3.4 Comparison with 24° bicrystals

In the previous chapter, a comparison between the Strathclyde step-edge and bicrystal junctions was given. The step-edges were found to have a higher mean $I_C R_N$ product than the bicrystal junctions. However the step-edge junctions also had a larger spread in their junction properties than the bicrystal devices. In this section a comparison is given between the step-edge and 24° bicrystal SQUIDs fabricated at Strathclyde. The bicrystal data discussed in this chapter comes from a sample of thirty SQ1 design SQUIDs of inductance 70pH incorporating junctions of width 2μm. This data will be compared with the data measured for the SQ1 design step-edge SQUIDs. Most of the bicrystal SQUIDs were fabricated and tested by A. Eulenburg, E.J. Romans and C. Carr.

As a larger mean $I_C R_N$ is obtained for the step-edge junctions, one may ex-

pect to see a correspondingly larger maximum voltage modulation depth ΔV for the step-edge SQUIDs. However, for 11 step-edge SQUIDs fabricated on 5 different substrates, a mean of $\Delta V \approx 15\mu$V with a standard deviation of 9μV is obtained, which is no better than maximum modulation depths measured for the bicrystals. For the thirty 24° bicrystals a mean of $\Delta V \approx 16\mu$V is obtained with a standard deviation of 5μV. The lack of any increase observed in ΔV can be attributed to the greater mismatch between the two junctions in the SQUID, which is a consequence of the larger spread observed in the parameters of the step-edge junctions. Comparing the measured values of the modulation depth ΔV_{meas} for the bicrystals, with the maximum modulation depth predicted by Equation 1.13 supports this. For the bicrystal SQUIDs a best fit to the data yields $\Delta V_{\text{meas}} = 0.66\Delta V_{\text{pred}}$ similar to best fit of $\Delta V_{\text{meas}} = 0.63\Delta V_{\text{pred}}$ obtained for the step-edge SQUIDs. Given that the step-edge junctions were generally found to have a higher $I_C R_N$, the similar ΔV's obtained for the bicrystal and the step-edge SQUIDs suggests that the improved $I_C R_N$ of the step-edges is generally offset by the likelihood of there being greater discrepancies between the parameters of the two junctions. The largest voltage modulation depth measured for any SQUID was for a step-edge device which had $\Delta V = 36\mu$V. The intrinsic white flux noise of the bicrystal SQUIDs was generally 10-30$\mu\Phi_0/\sqrt{\text{Hz}}$, comparable with that of the step-edges as expected given the similarities in their mean ΔV values. Both the best step-edge SQUID and the best bicrystal SQUID had a similar white flux noise performance, both approximately $5\mu\Phi_0/\sqrt{\text{Hz}}$.

4.4 Summary

The fabrication and characterisation of step-edge SQUIDs has been discussed. The electrical properties of 23 step-edge SQUIDs were measured and compared with the properties of the Strathclyde bicrystal SQUIDs.

All of the SQUIDs discussed in this chapter exhibited periodic voltage modu-

lation in the presence of an applied flux. The SQUID bias current was optimised to obtain the maximum voltage modulation depth ΔV for each SQUID. For the step-edge SQUIDs, the measured value of ΔV for the SQUIDs was found to be, on average, approximately 63% of that predicted using the analytical expression derived by Enpuku *et al.* (Equation 1.13). The most significant factor contributing to a smaller than expected ΔV is believed to be asymmetries in the electrical properties of the junctions in the SQUID. Taking into consideration the effects of thermal noise rounding on the SQUID I-V characteristics, the curves measured for almost all of the 23 devices closely matched those predicted by the RSJ-model. Two exceptions were devices which had a much larger than predicted dynamic resistance. This resulted in these SQUIDs showing an unusually large maximum voltage modulation depth, much greater than that predicted for the SQUID by Equation 1.13. However, given their large modulation depths, neither of these devices showed as good a noise performance as one may expect. This is in agreement with measurements performed on 30° bicrystal SQUIDs where the film is grown by PLD. In contrast, Beyer *et al.* measure large values of ΔV and low noise performance for their 30° bicrystal devices, where their films are grown by magnetron sputtering. The origin of the high ΔV values and the corresponding noise performance and their relation to the film growth technique and YBCO microstructure requires further investigation.

A comparison between step-edge and 24° bicrystal devices revealed that similar ΔV's and noise performances are obtained with SQUIDs incorporating both types of junction. Compared with reports in the literature for both step-edge and bicrystal devices, the 23 step-edges discussed here generally exhibited a favourable noise performance. Almost all of the SQUIDs had a white flux noise of 10-30$\mu\Phi_0/\sqrt{\text{Hz}}$ which is typical of values quoted in the literature for devices of similar inductance. The best step-edge SQUID had an excellent noise performance with a white flux noise of just $5\mu\Phi_0/\sqrt{\text{Hz}}$ which compares well with the best value reported in the literature.

References

[1] R.C. Black, A. Mathai, F.C. Wellstood, E. Dantsker, A.H. Miklich, D.T. Nemeth, J.J. Kingston and J. Clarke, Appl. Phys. Lett. 62, p.2128 (1993).

[2] J.M. Jaycox and M.B. Ketchen, IEEE Trans. Magn. MAG-17, p.400 (1981).

[3] M.B. Ketchen and J.M. Jaycox, Appl. Phys. Lett. 40, p.736 (1982).

[4] D. Koelle, A.H. Miklich, F. Ludwig, E. Dantsker, D.T. Nemeth and J. Clarke, Appl. Phys. Lett. 63, p.2271 (1993).

[5] J. Clarke and R.H. Koch, Science 242, p.217 (1988).

[6] M.B. Ketchen, IEEE Trans. Magn. MAG-23, p.1650 (1987).

[7] H. Hilgenkamp, *High-T_C DC SQUID Magnetometers*, PhD thesis, University of Twente, Netherlands (1995).

[8] K.C. Gupta, F. Garg and I.J. Bahl, *Microstrip Lines and Slotlines*, Artech House, Dedham, p.263 (1979).

[9] L.N. Smith, D.W. Jillie and H. Kroger, IEEE Trans. Magn. MAG-21, p.874 (1985).

[10] FASTHENRY Dept. of Electrical Engineering and Computer Science, M.I.T., Cambridge, MA, USA.

[11] M. Kamon, M.J. Tsuk and J.K. White, IEEE, Trans. Microwave Theory and Techn. 42, p.1750 (1994).

[12] Z. Du., S. R. Whiteley, T. Van Duzer, Ext. Abs. ISEC'97, Berlin, p.293 (1997).

[13] D. Winkler, Y.M. Zhang, P.A. Nilsson, E.A. Stepantsov and T. Claeson, Phys. Rev. Lett. 72, p.1260 (1994).

[14] D. Koelle, R. Kleiner, F. Ludwig, E. Dantsker and J. Clarke, Rev. Mod. Phys. 71, p.631 (1999).

[15] K. Enpuku, T. Minotani, F. Shiraishi, A. Kandori and S. Kawakami, IEEE Trans. Appl. Supercond. 9, p.3109 (1999).

[16] C.D. Tesche and J. Clarke, J. Low. Temp. Phys. 29, p.310 (1977).

[17] K. Enpuku, Y. Shimomura and T. Kisu J. Appl. Phys. 73, p.7929 (1993).

[18] T. Minotani, S. Kawakami, T. Kiss and K. Enpuku, Jpn. J. Appl. Phys. 36, p.L1062 (1997).

[19] J. Beyer, D. Drung, F. Ludwig, T. Minotani and K. Enpuku, Appl. Phys. Lett. 72, p.203 (1998).

[20] A. Eulenburg, *High Temperature Superconducting Thin Films and Quantum Interference Devices (SQUIDs) for Gradiometers*, PhD thesis, University of Strathclyde, (1999).

[21] P. Petersen, *Private communication*, NKT, Copenhagen, Denmark, (1999).

[22] F. Dillman, V.N. Glyantsev and M. Siegel, Appl. Phys. Lett. p.1948 (1996).

Chapter 5

SQUID Gradiometers

One of the major aims at the beginning of the work described in this thesis was to develop a step-edge Josephson junction technology and evaluate it as a viable alternative to the use of bicrystal substrates for the fabrication of SQUIDs. Chapter 3 and Chapter 4 described the development of this technology and demonstrated that step-edges represent a cost-effective alternative to the use of bicrystals. It was found that one could achieve even better performance from the step-edge junctions, although one should also expect in general, a slightly larger spread in the junction parameters. The noise performance of SQUIDs incorporating either step-edge or bicrystal junctions was found to be broadly similar.

Concurrently with the development of the step-edge devices, the second major aim of this thesis was addressed: to develop SQUID gradiometers for unshielded applications. Three generations of single-layer gradiometers (SLGs) were characterised (two designs which were fabricated on $10 \times 10\text{mm}^2$ STO substrates and one large area design fabricated on $30 \times 10\text{mm}^2$ STO substrates). Several devices of each design were fabricated and tested, incorporating either step-edge or bicrystal junctions. Having established that the intrinsic noise characteristics of the step-edge and bicrystal SQUIDs were similar, the type of junction technology is considered to be arbitrary in terms of SLG performance.

The introductory section of this chapter provides a brief background to SQUID gradiometry and describes the key parameters which characterise the performance of a SLG. A detailed account of the characterisation and performance of the three generations of SLG devices follows, including discussion on the effective area and device balance measurements and details of the best gradient field sensitivities achieved for each of the three designs. The chapter also includes details of the suitability of

the SLGs for practical measurements, with reference to some of the applications for which the SLG devices have been used, both at Strathclyde and elsewhere.

5.1 Introduction

5.1.1 Motivation

Chapter 1 explained how the field sensitivity of a SQUID is limited by the constraint that the intrinsic flux noise increases with the SQUID inductance and that to improve the field sensitivity the SQUID can be coupled to a larger pick-up loop to form a magnetometer. The intrinsic noise level of a magnetometer is typically several orders of magnitude lower than the level of magnetic interference unless they are operated in a heavily shielded environment. For many applications, such as magnetocardiography (MCG), this restricts practical operation of the devices to expensive shielded rooms, typically made from mu-metal (*e.g.* the shielded room at [1]). For SQUID applications, such as geophysical surveys or non-destructive evaluation (NDE), a shielded room is not feasible. For unshielded and moderately shielded applications SQUID gradiometry permits the discrimination of the small localised field to be measured from the ambient background field of the Earth and other relatively distant sources of electromagnetic interference. An introduction to SQUID gradiometers was given in Chapter 1. In this section the details most relevant to SLGs are expanded upon. A brief introduction to the common techniques used in SQUID gradiometry is included although more a substantial account is given in [2] and [3] for example.

A common approach to realising an HTS gradiometer is to combine electronically the signals from two or more magnetometers (or indeed autonomous SQUIDs) [4]. This technique offers considerable freedom as the separate chips can be orientated to form either axial or planar gradiometers, and higher orders of gradiometer can be made simply by using larger numbers of SQUID or magnetometer chips. The most common technique is to simply subtract the signal from two magnetometers

to form a first-order electronic gradiometer. A great advantage of this technique is that large baselines (defined as the separation between the centre of the two pick-up loops in the gradiometer) are possible. By using electronic subtraction techniques one can achieve excellent device balance (defined as the ratio of the output of the output of the whole device in response to a uniform field, to the response of the device when the same uniform field is applied to just one of the pick-up loops). However, requirements on the system linearity and the common mode rejection ratio of the subtraction system limit electronic gradiometers. In practice phase shifts and the non-linearities in the frequency response of the electronics, mean that a good electronic balance can only be achieved over a very narrow bandwidth [5, 3] making such devices impractical for most applications. In addition, in the presence of high background noise, the dynamic range and slew rate of the magnetometers becomes is a limiting factor. One of the most successful demonstrations of electronic gradiometry circumvents some of these problems although this technique requires a third reference SQUID sensor to measure the background level of magnetic interference [6]. The reference device sits between the other two sensors and directly feeds back any measured magnetic flux to the two sensors which form the gradiometer, ensuring that they do not have to respond to the background uniform magnetic interference.

An alternative approach to realising an HTS SQUID gradiometer is to couple two (or more) pick-up loops to the SQUID either inductively [7] or directly [8]. The problems associated with increased low frequency noise which arise in inductively coupled devices incorporating multiple layers of superconductor were introduced in Section 1.4. Fully integrated inductively coupled gradiometers suffer from suppressed critical currents and high $1/f$ noise as a consequence of the multilayer deposition (see [9] for example). Directly coupled SLGs consisting of two symmetric pick-up loops directly connected to a SQUID are fabricated from a single layer of HTS thin film and thus avoid the problems of weak pinning sites and excess $1/f$ noise. As discussed in Chapter 1, gradient sensitivities of 300-500fT/cm$\sqrt{\text{Hz}}$ are rou-

tinely achieved for SLGs fabricated on $10 \times 10\text{mm}^2$ substrates, where the flux noise is generally white down to frequencies of the order of 1Hz when using ac-bias (*e.g.* [8] and [10]-[13]). This is significantly better than the gradient noise reported for flip-chip gradiometers incorporating inductively coupled multi-layer flux transformers where gradient sensitivities are in the $\text{pT/cm}\sqrt{\text{Hz}}$ range at best [9, 14]. The SLG concept can be extended by flip-chip coupling a large single layer flux transformer to the SLG. Tian *et al.* [15] reported a gradient sensitivity of $73\text{fT/cm}\sqrt{\text{Hz}}$ for such a device where they flip-chip coupled a large single layer gradiometric YBCO flux transformer fabricated on a 2" silicon wafer to a SLG fabricated on a $10 \times 10\text{mm}^2$ substrate. A problem associated with all flip-chip gradiometers arises from the difficulties in accurately aligning the separate chips, which results in a relatively poor device balance. The Berkeley group have however demonstrated a flip-chip coupled device that can have its balance adjusted mechanically while its submersed in liquid nitrogen [16]. The device incorporates a single layer asymmetric flux transformer, fabricated on a 100mm long sapphire wafer with CeO_2 buffer layer, inductively coupled to a $10 \times 10\text{mm}^2$ SQUID magnetometer chip. By fine mechanical adjustment of the position of the flux transformer relative to the magnetometer a balance of approximately 1/1400 was achieved - significantly better than the typical balance of 1/100 to 1/300 achieved with $10 \times 10\text{mm}^2$ SLGs [10]-[13]. The Berkeley group have also recently extended this concept by coupling an asymmetric flux transformer with three loops to a magnetometer to form a second-order gradiometer [17]. For practical applications however, the required alignment adjustments may be a limiting factor [18]. SLGs offer good gradient sensitivity, are simple to fabricate and avoid the respective problems of excess $1/f$ noise and poor balance associated with multilayer devices and flip-chipping. For these reasons the SLG approach has been adopted here.

5.1.2 Gradiometer Characterisation

The performance of a SLG is characterised by its gradient field sensitivity and by the ability of the device to reject unwanted fields (uniform fields in the case of a first-order gradiometer). The first-order SLG's capabilities at rejecting uniform fields are characterised by the device balance b, which can be expressed as

$$b = A_{\mathrm{PAR}}/A_{\mathrm{MAG}}, \tag{5.1}$$

where A_{PAR} is the device's parasitic effective area to uniform fields and A_{MAG} is the effective area of the SLG operating with just one pick-up loop *i.e.* the device operating as a magnetometer. The sources which contribute to the parasitic effective area are discussed in detail in Chapter 6, where a novel method of reducing A_{PAR} is introduced. For now it is sufficient to regarded A_{PAR} as a combination of the uniform field response of the SQUID and any uniform field response arising from imperfections in the pick-up loop structure. The SQUID's response represents the most significant contribution to A_{PAR}, and thus for SLGs incorporating conventional SQUIDs one generally aims to increase A_{MAG} to improve the balance.

The gradient field sensitivity is a function of the device baseline l, A_{MAG} and the intrinsic flux noise $\sqrt{S_\Phi}$ of the SLG - which for a shielded SLG is generally dependent on the intrinsic flux noise of the SQUID which it incorporates. The gradient field sensitivity can be expressed as

$$\sqrt{S_{\mathrm{G}}} = \frac{\sqrt{S_\Phi}}{lA_{\mathrm{MAG}}}. \tag{5.2}$$

For the best gradient sensitivities it is desirable that the SLG incorporates a low noise SQUID and that the product lA_{MAG} is maximised. The optimum baseline of a gradiometer however is also dependent on the specific application of the device (see for instance [2, 19]). From Equation 1.20 in Chapter 1 it can be seen that A_{MAG} depends on the sensing area of the pick-up loop A_{LP} (which is related to the

actual area of the pick-up loop and the degree of flux focusing in the loop) and the inductance mismatch L_{LP}/L_M, where L_{LP} is the self inductance of the pick-up loop and L_M is the mutual inductance between the pick-up loops and the SQUID. To increase A_{MAG} one should increase A_{LP} and decrease L_{LP} for a given L_M. However for superconducting tracks of fixed linewidth, an increase in A_{LP} results in an increase in L_{LP}. Consequently one increases the linewidth of the pick-up loop tracks in an SLG to significantly reduce L_{LP} while only slightly decreasing A_{LP}.

The remainder of this chapter aims to demonstrate that with first-order SLGs incorporating high performance SQUIDs one can achieve gradiometers with excellent sensitivities that are practical devices for real applications.

5.2 Small Gradiometers

Gradiometers were fabricated on $10 \times 10\text{mm}^2$ STO substrates using two different device designs. The design and fabrication of these two types of devices and their performance, in terms of device balance and gradient sensitivity, will now be discussed. Many of the small bicrystal SLGs were fabricated by E.J. Romans and A. Eulenburg.

5.2.1 First Generation SLGs

Design and Fabrication

The layout of the first generation SLG is shown in Figure 5.1 - note that the SQUIDs incorporated in these devices are the SQ1 design introduced in Chapter 4 which have a self inductance of $L_{SQ} = 70\text{pH}$. Each SLG incorporates three separate SQUIDs. The length along the longer axis of the gradiometer, from the outer edge of one pick-up loop to the outer edge of the other, is 9mm, with 500μm left clear at the edges of the substrate to allow for photoresist edge removal (discussed in Chapter 2) and to avoid handling difficulties during the patterning of the device. The superconducting tracks of the pick-up loops have a linewidth of 0.5mm and the

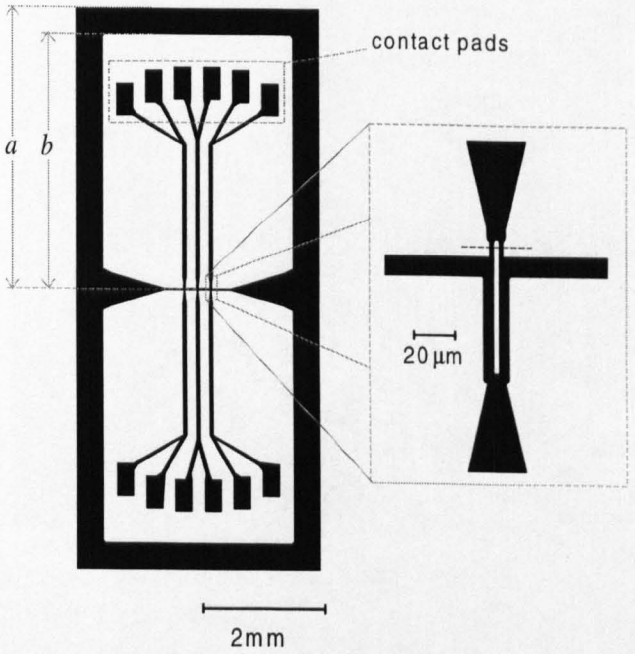

Figure 5.1: Layout of the first generation SLG with a baseline of 4.2mm. *The upper dotted box shows the location of the contact pads, where wire bonds connect the gradiometer to the PCB. The other dotted box shows a magnified view of one of the three SQUIDs in the centre of the SLG. The dotted line in the magnified view shows the location of the SQUID's junctions.*

estimated inductance of each pick-up loop is $L_{\mathrm{LP}} = 7\mathrm{nH}$. This yields a ratio for the inductance mismatch of $L_{\mathrm{M}}/L_{\mathrm{LP}} = 1/152$ taking the measured value of $L_{\mathrm{M}} = 46\mathrm{pH}$ for the SQ1 design SQUID from the previous chapter. The baseline l depends on the effective sensing area of the gradiometer pick-up loops which depends on the degree of flux focusing in each loop as well as their geometrical size. The centre of the sensing area of each pick-up loop will be approximately distance $\sqrt{ab}/2$ from the centre of the device, where a is the distance from the centre of the gradiometer to the outer edge of the pick-up loop and b is the distance from the centre of the gradiometer to the inner edge of the pick-up loop (as shown in Figure 5.1). For this device this yields a baseline of $l = \sqrt{ab} \approx 4.2\mathrm{mm}$.

The devices were fabricated on $10 \times 10\mathrm{mm}^2$ STO substrates (either bicrystal or single crystal in the case of the step-edge devices). In the case of the step-edge devices, the steps were prepared using the standard fabrication procedure introduced in Chapter 3, and milled to a height h to give the optimum t/h ratio for 200nm thin films as discussed in Section 3.4.1. The YBCO thin films were deposited using

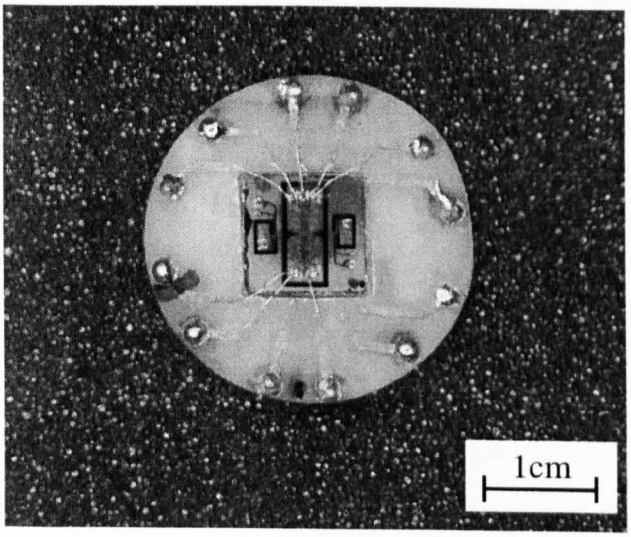

Figure 5.2: Photograph of a completed first generation SLG, wire bonded to its PCB chip-carrier ready for encapsulation. The YBCO structures either side of the SLG are test devices.

the standard PLD process described in Chapter 2 and patterned using conventional photolithography and argon-ion milling. A 200nm sputtered gold film was patterned into the device's contact pads using the same technique. The devices were then glued onto PCB chip-carriers with the contact pads ultrasonically bonded to the PCB using aluminium wire. The devices were generally encapsulated to prevent moisture damage and increase their lifetime. The device encapsulation consisted of a PCB cap glued to the PCB chip carrier, and sealed round the edges using epoxy resin. Figure 5.2 is a photograph of one of the devices mounted in the PCB chip-carrier before encapsulation.

Results and Discussion

The parasitic effective area A_{PAR} of each SLG in a uniform field was measured using a pair of calibrated 1.2m diameter Helmholtz coils. The devices were cooled in liquid nitrogen and operated in a FLL using Conductus PC-100 electronics. The modulation and feedback signals were either directly injected along the centre of the device using the connections from the neighbouring SQUIDs, or were applied inductively via an external copper coil tightly coupled to one of the gradiometer loops. An ac current was passed through the Helmholtz coils and the resulting

response of the SLG was lock-in detected. The measured effective area was initially found to have an unexpected dependence on the frequency of the ac current passed through the coils. This was believed to be a consequence of eddy currents generated in the steel beams of the floor perturbing the measurement. By raising the Helmholtz coils such that the SLG in the centre was approximately 1.5m from the floor and ensuring the system was far away from other metal structures, this dependence was reduced to within the experimental error over the typical measurement frequency range of 0-2kHz. For each device the magnitude of the Helmholtz coil current was varied to obtain applied magnetic fields with amplitudes in the range 0.5-2μT. The SLGs exhibited a linear response to the field amplitude with the parasitic effective areas of the all SLGs in the range 400-600μm^2. Two sources of imperfection in the SLG structure are likely to contribute to chip-to-chip variations in A_{PAR}: (1) as a consequence of tolerances in the fabrication procedure there is likely to be slight variations in the geometrical structure of the SLGs from chip-to-chip; and (2) the sample may suffer slight damage during fabrication which could effect the parasitic effective area of each device.

One would expect the effective area of the SQUID A_{SQ} in the SLG to lie somewhere within the range of values measured for the parasitic effective area, with the nature of the imperfections from chip-to-chip depending on whether they contribute negatively or positively to the measured value of A_{PAR}. This was confirmed using the modeling package FASTHENRY. Elements were created to represent an "infinite" wire in the direction of the z-axis and a SQUID loop in the xz-plane, at a perpendicular distance r_x from the wire. The mutual inductance M between the wire and SQUID loop was modeled. When the distance r_x between the SQUID and the wire is much greater than the dimensions of the SQUID, one can assume that the field is uniform over the SQUID loop and therefore that $A_{\mathrm{SQ}} = 2\pi r M/\mu_0$. Using this method and an assumed magnetic penetration depth of $\lambda_L = 214$nm FASTHENRY estimated $A_{\mathrm{SQ}} \approx 520\mu$m^2.

To measure A_{MAG}, and thus obtain a measure of the balance of the SLG, one

of the gradiometer's pick-up loops was cut and the effective area of the device was measured using the procedure described above. Note that it is better to simply cut rather than remove the entire pick-up loop to maintain constant flux focusing effects. This procedure was only carried out on one of the step-edge SLGs to avoid the destruction of large numbers of gradiometers. A_{MAG} was measured as $0.08\mathrm{mm}^2$. This was in reasonable agreement with the values estimated using FASTHENRY. The measured A_{MAG} means the device balance of is approximately 1/160 where A_{PAR} is taken as $500\mu\mathrm{m}^2$.

To measure the flux noise characteristics of the SLGs the devices were operated in a FLL, using ac-bias, and spectra were recorded for each gradiometer cooled inside three layers of mu-metal shielding and unshielded in the open laboratory. Like the autonomous SQUIDs discussed in the previous chapter the SLGs generally had a shielded white flux noise of less than $30\mu\Phi_0/\sqrt{\mathrm{Hz}}$. The step-edge devices had an excellent noise performance, with three of the four tested SLGs exhibiting a shielded white flux noise of $11\mu\Phi_0/\sqrt{\mathrm{Hz}}$ or better when operated with the best SQUID on each chip. The best shielded flux noise was also measured for a step-edge device which had a flux noise of approximately $5\mu\Phi_0/\sqrt{\mathrm{Hz}}$ at 1kHz, with the noise spectrum essentially flat down to 1Hz. This corresponds to a gradient sensitivity of approximately $308\mathrm{fT/cm}\sqrt{\mathrm{Hz}}$ given that $l = 4.2\mathrm{mm}$ and that A_{MAG} was measured as $0.08\mathrm{mm}^2$. The shielded and unshielded spectra measured for this device are shown in Figure 5.3. The level of magnetic interference in the laboratory results in a significant increase in the flux noise of the SLG. Measurements performed with flux-gate magnetometers suggest that the direct pick-up of environmental fields by the SLG will result in a significant increase in device's flux noise, however effects such as suppression of the junctions critical current cannot be ruled out from contributing to the measured unshielded noise spectra.

The gradient sensitivities reported here compare well with those reported in the literature for SLG fabricated on $10 \times 10\mathrm{mm}^2$ substrates where typically 300-$500\mathrm{fT/cm}\sqrt{\mathrm{Hz}}$ has been achieved. The intrinsic flux noise of these devices was

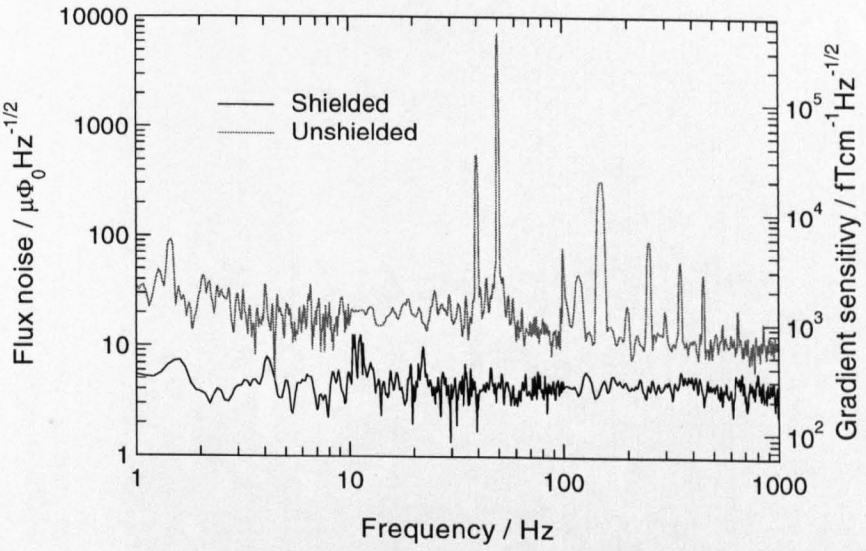

Figure 5.3: Noise spectra measured for a first generation small SLG with the SQUID operated using ac-bias. The measured flux noise and corresponding gradient field sensitivities are shown for the device cooled in the open laboratory (unshielded) and for the device cooled inside three layer of mu-metal (shielded).

generally higher than the value of $5\mu\Phi_0/\sqrt{\text{Hz}}$ achieved for the best device discussed here. An exception is the slightly better flux noise of $4.3\mu\Phi_0/\sqrt{\text{Hz}}$, measured for a SLG at 1kHz by Wunderlich *et al.* [20]. However due to their design having smaller pick-up loops, they obtain a poorer gradient sensitivity of $430\text{fT/cm}\sqrt{\text{Hz}}$.

5.2.2 Second Generation SLGs

Design and Fabrication

Figure 5.4 shows the layout of the second generation SLG. This SLG consists of two identical pick-up loops directly coupled to four identical SQUIDs in the centre. The inductance of the SQUIDs was increased compared with that of the first generation devices to improve the mutual inductance L_{M} between the pick-up loops and the SQUID - Koelle *et al.* recently showed that the optimum SQUID inductance is $L_{\text{SQ}} \sim 100\text{pH}$ for a directly-coupled device [3]. The SQUIDs in the second generation SLGs are of the SQ3 design described in Chapter 4 which have a self inductance of $L_{\text{SQ}} = 105\text{pH}$ and a coupling inductance to the pick-up loops of $L_{\text{M}} = 90\text{pH}$. Compared with the first generation devices, in this SLG design the pick-up loops

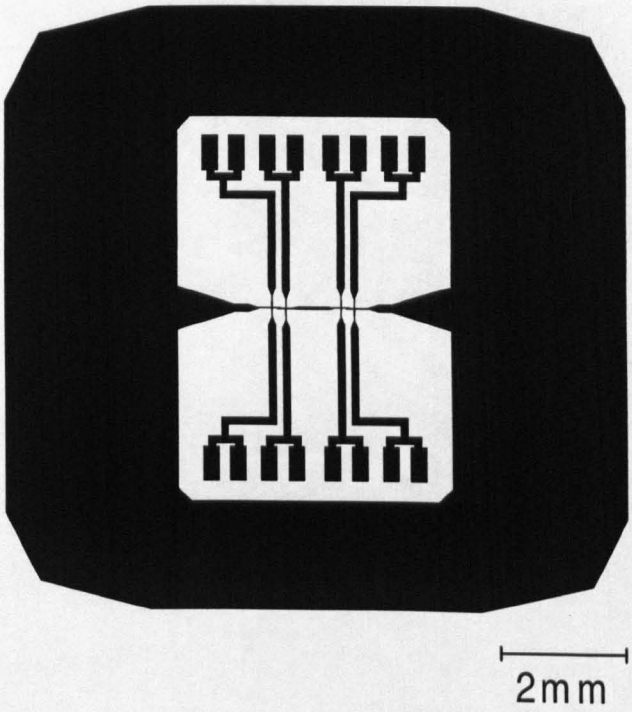

Figure 5.4: Layout of the second generation SLG which has a baseline of $l = 3.6$mm. *Each gradiometer incorporates four* 105pH *SQUIDs in the centre of the device.*

were significantly widened to increase the flux capture area, while the linewidth of the tracks of the pick-up loops was increased to minimise the loop inductance, and therefore minimise the mismatch between the pick-up loop inductance L_{LP} and L_{M}. The linewidth of the pick-up loops along the axis parallel to the baseline is 2.5mm, while the linewidth of the other sides gradiometer's pick-up loops is 1.6mm, resulting in a estimated loop inductance of $L_{\mathrm{LP}} = 10$nH. This yields an inductance mismatch of 1/111, an improvement over that of the first generation SLG. Having pick-up loops with a constant linewidth of 2.5mm would significantly decrease the baseline, but here the linewidth of 1.6mm at the ends of the gradiometer results in a baseline of $l = 3.6$mm.

The second generation SLGs were fabricated using the procedure described above for the first generation devices. A completed device is shown in Figure 5.5.

Results and Discussion

The parasitic effective areas of the second generation SLGs were measured with

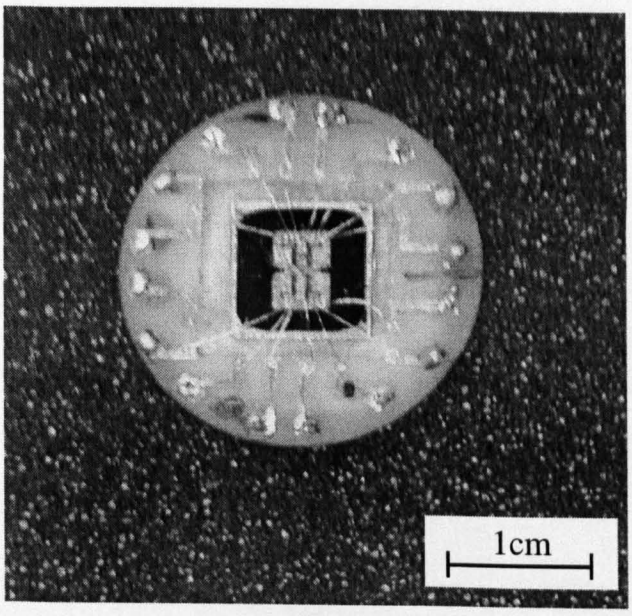

Figure 5.5: Photograph of a completed second generation SLG ready for encapsulation.

the Helmholtz coils using the procedure described above for the first generation devices. All of the SLGs tested were found to have parasitic effective areas in the range 600 to 750μm^2. Again, modeling the effective area of the bare SQUID confirmed that the measured values are of the order expected.

Given that the second generation SLGs have a significantly larger flux capture area and a better match between their inductances L_{M} and L_{LP} than the first generation SLGs, one would expect a corresponding increase in the effective area A_{MAG}. This was confirmed when one pick-up loop on a second generation gradiometer was cut and an effective area of $A_{\mathrm{MAG}} = 0.20\mathrm{mm}^2$ was measured. Given their larger A_{MAG}, the second generation devices also have a significantly improved balance in comparison with the first generation SLGs. Taking $A_{\mathrm{PAR}} = 675\mu\mathrm{m}^2$ yields an approximate balance of 1/300, a significant improvement over the balance of the first generation devices.

Given that the product lA_{MAG} is more than a factor of two larger than that of the first generation SLGs, one might also expect to observe considerable improvements in the gradient sensitivities of the second generation devices. Unfortunately this was not the case. The shielded and unshielded noise characteristics of the SLGs

were measured using the procedure described above for the first generation devices. The intrinsic flux noise of the devices, measured inside three layers of mu-metal, was generally found to be higher than that of the first generation gradiometers. While the $I_C R_N$ products of both the first and second generation gradiometers were similar, the second generation devices generally had larger I_C's. Their large I_C's combined with the larger inductance of the SQUIDs in the second generation SLGs (105pH compared to 70pH for the SQUIDs in the first generation SLGs) resulted in the devices having relatively large β_L's and consequently a relatively high intrinsic flux noise. The best noise performance was achieved with a bicrystal device, the shielded and unshielded spectra of which are shown in Figure 5.6. The shielded white noise of $22\mu\Phi_0/\sqrt{\text{Hz}}$ measured at 100Hz corresponds to a gradient sensitivity of $633\text{fT/cm}\sqrt{\text{Hz}}$, significantly poorer than the sensitivity achieved for the best first generation device - the flux noise measured for the best first generation device was approximately four times lower. The factor of two increase in lA_{MAG} over that of the first generation devices is outweighed by the factor of four increase in the flux noise of the best second generation SLG. Only three second generation SLG chips were fabricated, compared with approximately fifteen first generation gradiometers - a lower flux noise may have been achieved for the second generation devices had more samples been fabricated.

5.2.3 Small Gradiometer Applications

The sensitivities achieved with the small SLG devices make them suitable for many applications. In addition to high sensitivity, most applications also require the SQUID sensors to be extremely stable in FLL-mode to withstand changes in the external magnetic field when operated unshielded in electromagnetically noisy environments. One major application which requires stability in an industrial environment is the use of SQUID sensors in non-destructive evaluation (NDE). At Strathclyde it has been demonstrated that with simple commercially available HTS SQUIDs, with relatively poor sensitivity, one can reasonably diagnose defects and

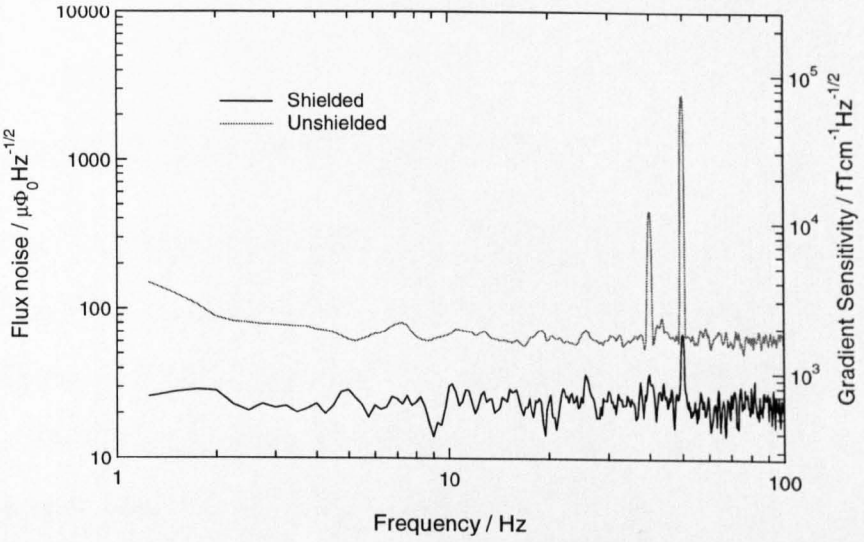

Figure 5.6: Noise spectra measured for the a second generation small SLG fabricated on a bicrystal substrate, with the SQUID operated using ac-bias. The measured flux noise and corresponding gradient field sensitivities are shown.

faults in simulated aircraft structures [21]. The SLGs discussed here have also been used for such studies, and offer an improved sensitivity over the commercial devices. The SLGs have remained stable and locked for long periods of time in the open laboratory, sufficient enough to complete scans of NDE samples over a period of an hour or more. These experiments were performed by C. Carr and are reported in [22]. In addition experiments have shown that the small SLGs operated successfully when in motion in unshielded environments [23].

The first generation SLGs have also been used in another application, as a sensor in a cryogenic current comparator, in collaboration with the National Physical Laboratory (NPL) in Teddington. The HTS current comparator constructed at NPL consists two ion beams which pass through a superconducting tube. When the two ion currents are of equal magnitude, traveling in opposite directions, the screening currents induced in the superconducting tube cancel, which results in net zero field being measured, in this case by the SLG. A difference in the magnitude of the beam currents results in non-zero screening currents which induce a field that is detected by the SLG. The use of a gradiometer was found to greatly improve the uniform field rejection thus improving the common-mode rejection of the current comparator.

These experiments are reported in detail in [24].

5.3 Large Gradiometers

One of the most significant applications for HTS SQUID devices is the measurement of biomagnetic signals, especially those arising in the heart (magnetocardiography). Other groups have carried out such measurements with considerable success using either directly coupled magnetometers (*e.g.* [25]) or small SLGs similar to the devices discussed above (*e.g.* [12]). However the demonstrations reported in the literature were carried out in mu-metal shielded rooms which strongly attenuate the Earth's dc field as well as fields of higher frequencies. Such shielded rooms are rare, and extremely expensive to build, thus hindering the commercial application of the HTS devices in such areas. For clinical applications good magnetocardiograph (MCG) signal-to-noise ratios must be achieved for devices cooled in the Earth's field. The realisation of such a device, a large area gradiometer fabricated on a $30 \times 10\text{mm}^2$ substrate, is discussed here.

Design and Fabrication

The third generation SLG was designed by A. Eulenburg and the layout is shown in Figure 5.7. Each SLG incorporates four separate SQ4 design SQUIDs which have a self inductance of $L_{\text{SQ}} = 114\text{pH}$ and coupling inductance of $L_{\text{M}} = 104\text{pH}$. Each pick-up loop has an estimated inductance of approximately 15nH, yielding a ratio for the inductance mismatch of 1/144. The linewidth along the longer axis of the gradiometers is 2.5mm, while the linewidth along the short axis of each loop is smaller at just 1.7mm to give the device a large baseline of $l = 13\text{mm}$.

The thin film deposition procedure was optimised for the growth of large area films. The growth parameters and laser optics were modified to produce an asymmetric plasma plume which is expanded significantly in one direction to give good coverage over both the longer and shorter axes of the substrate. Excellent film homogenities were achieved with at most only a 5% variation in film thickness over the

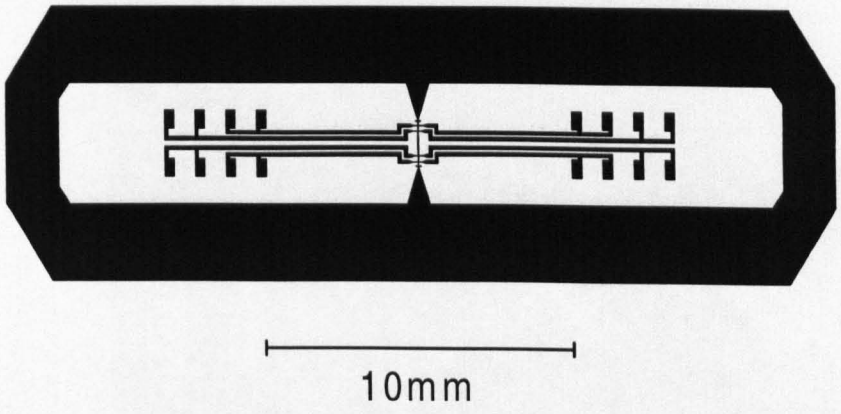

Figure 5.7: Layout of the large area SLG which has a baseline of l = 13mm. Each gradiometer incorporates four 114pH SQUIDs in the centre of the device.

$30 \times 10\text{mm}^2$ substrate. The film deposition optimisation experiments were carried out by A. Eulenburg [26].

The fabrication procedures used to pattern the large area gradiometers were identical to those used for the other two SLG designs discussed above. Figure 5.8 is a photograph showing a fully encapsulated large area gradiometer as well as a device ready for encapsulation.

Results and Discussion

Using the standard Helmholtz coils set-up, the parasitic effective areas of the third generation SLGs were measured to be in the range of approximately 600 to $800\mu\text{m}^2$. Given that the third generation gradiometers are significantly larger, and have a similar inductance mismatch one would expect the device to have a much larger A_{MAG} than the two small SLG devices. By cutting one pick-up loop an effective area of $A_{\text{MAG}} = 0.73\text{mm}^2$ was measured, corresponding to a device balance for $A_{\text{PAR}} = 700\mu\text{m}^2$ of approximately 1/1000. Again, the measured effective areas were in agreement with the values calculated using FASTHENRY. The balance of the large SLG is significantly better than the balances achieved for conventional SQUID SLGs by other groups (in the range 1/100 to 1/300 as discussed in Section 5.1.1) - all of their devices were fabricated on $10 \times 10\text{mm}^2$ substrates.

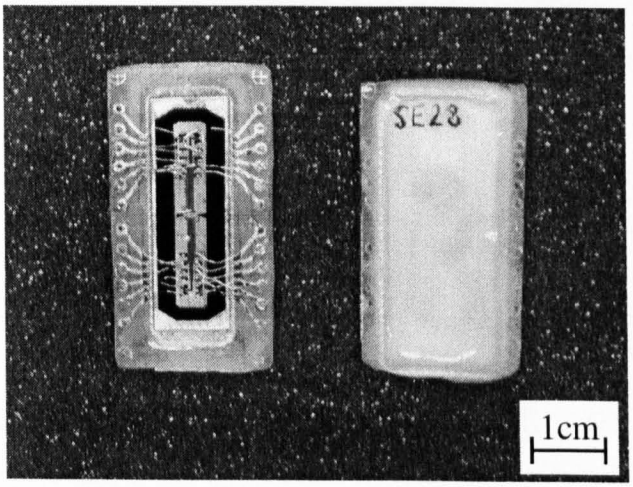

Figure 5.8: Photograph of a completed large area gradiometer wire bonded to a double sided PCB chip carrier (left), and a fully encapsulated large area SLG (right).

Unfortunately, the shielded flux noise levels measured for the large SLGs were not as good as those measured for the small substrate devices. Again this is partly a consequence of the increased SQUID inductance and relatively large values of β_L. Two bicrystal and one step-edge device were fabricated - the bicrystal devices were fabricated by A. Eulenburg. Most of the bicrystal SQUIDs had lower than expected $I_C R_N$ products, relatively weak voltage modulation depths and as a result had a high white noise levels of greater than $30\mu\Phi_0/\sqrt{\text{Hz}}$. A factor which lead to the poor device parameters was possibly the increased strain during film growth compared with that of the $10 \times 10\text{mm}^2$ bicrystal substrates. As the larger substrate expands more when heated this may have lead to a more significant strain on the weak fused bicrystal line, which may have resulted in degradation (*e.g.* oxygen losses) at the grain boundary in the overlying YBCO film. With no weak fused region, this problem is not such a significant issue for the growth of films on step-edge substrates. It was hoped that with the step-edge devices, improvements in $I_C R_N$ products and modulation depths would result in a better noise performance. Unfortunately this was not the case, with the SQUIDs on the step-edge chip exhibiting small $I_C R_N$ products and modulation depths of only a few μV. It was not clear whether this poor performance was associated with difficulties in the fabrication of step-edges on

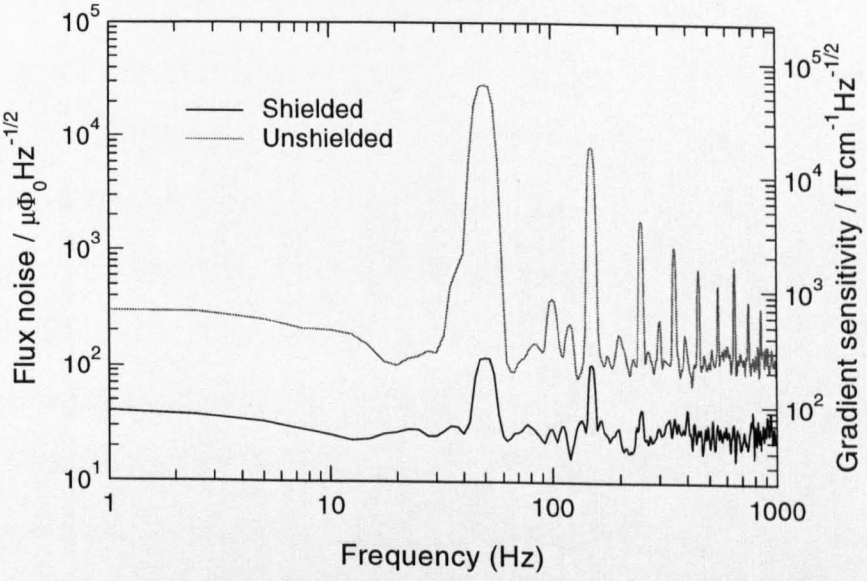

Figure 5.9: Noise spectra measured for the a large SLG fanricated on a bicrystal substrate, with the SQUID operated using ac-bias. The measured flux noise and corresponding gradient field sensitivities are shown.

large substrates, perhaps due to the variation in the mill-rate over the large area, or whether the problems were just with this one sample and not directly associated with the fabrication procedures. Further investigations are currently being undertaken by R. Palai. Despite the poor flux noise characteristics of the third generation step-edge SLG, the measured shielded white flux noise of $50\mu\Phi_0/\sqrt{\text{Hz}}$ translates to a gradient sensitivity of approximately $110\text{fT/cm}\sqrt{\text{Hz}}$. This is significantly better than any field sensitivities reported for SLGs fabricated by other groups.

The best bicrystal device had lower flux noise than the step-edge device. The best shielded noise measured was approximately $23\mu\Phi_0/\sqrt{\text{Hz}}$ at 1kHz which corresponds to a gradient sensitivity of $50\text{fT/cm}\sqrt{\text{Hz}}$, the best value reported in the literature for an HTS SLG [27]. In addition the field sensitivity is superior to the $79\text{fT/cm}\sqrt{\text{Hz}}$ achieved for the large baseline flip-chip gradiometer of Tian *et al.* discussed in Section 5.1.1. The shielded and unshielded noise spectra measured for this device are shown in Figure 5.9. An approximate five-fold increase was observed in the measured flux noise when the device was cooled in the open laboratory.

5.3.1 Large Gradiometer Applications

Trials were conducted to measure an adult magnetocardiograph (MCG) using the large SLGs. The experiments were performed in an aluminium screened room at the Wellcome Biomagnetism Unit at the Southern General Hospital in Glasgow. This facility is used regularly by the Strathclyde group for biomagnetism purposes using LTS devices. The aluminium shielded room provides considerable eddy-current screening at higher frequencies (down to a cut-off of approximately 2Hz), although in contrast with the MCG demonstrations cited above, there is no attenuation at dc, so the measurements were performed with the devices operating in the full Earth's field. Compared with the fully shielded noise measurements discussed above, when cooled in this environment the large area SLGs showed an increase in their white flux noise as one may expect for a device cooled in the Earth's field. The output from the SQUID was low-pass filtered with a cut-off frequency of 30Hz and recorded on a dynamic signal analyser.

A realtime MCG recorded using the best large area gradiometer is shown in Figure 5.10(a). In the screened room a signal-to-noise ratio for the main peak of approximately 6 was achieved. Figure 5.10(b) shows the realtime data in (a) averaged over 10 peaks. The QRS complex of the magnetic field signal from the heartbeat is clear, as indicated in the figure, while the T-wave component of the heartbeat can also be clearly identified in the realtime data. The improved characteristics of the large area gradiometer were sufficient to record an MCG in a completely unshielded environment. Such a realtime trace, for an adult heart measured with the device operating in the open laboratory is shown in Figure 5.10(c), where a signal-to-noise ratio of approximately 2 was achieved.

5.4 Summary

Three designs of gradiometers have been fabricated and tested - two designs $10 \times 10\text{mm}^2$ substrates and one design on $30 \times 10\text{mm}^2$ substrates. The balance

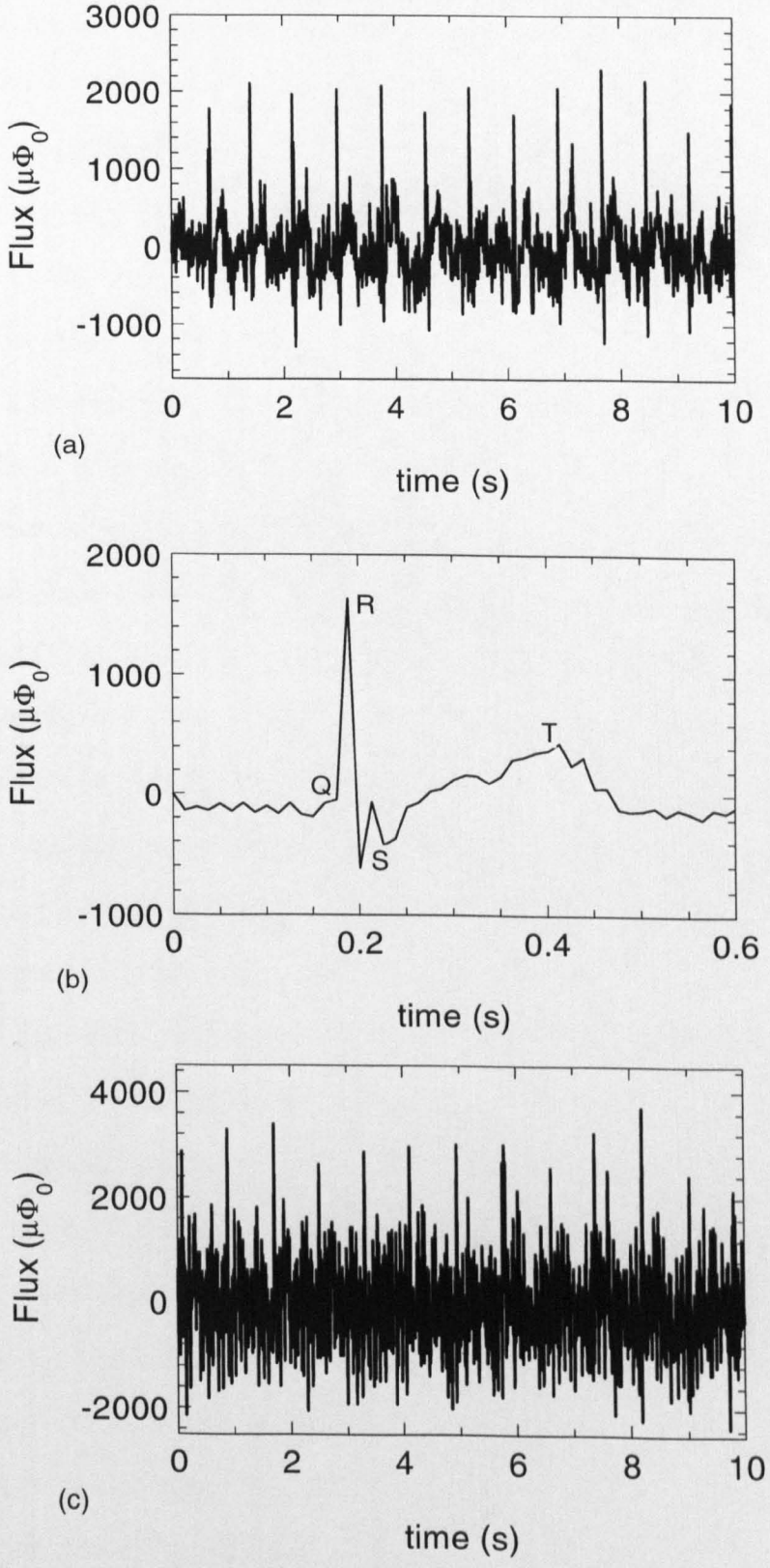

Figure 5.10: Biomagnetic data recorded from a healthy adult heart. (a) Realtime trace recorded with the SLG operated in the aluminium screened room. (b) The data in (a) averaged over ten peaks to show the QRST structure of the recorded trace. (c) Realtime trace recorded with the SLG operated with no shielding in the open laboratory.

and gradient sensitivities of the two generations of small SLGs fabricated on the $10 \times 10\text{mm}^2$ substrates, compared favourably with the performance of similar devices fabricated by other groups. The low intrinsic flux noise of many of small SLGs resulted in excellent gradient sensitivities, with the best gradient sensitivity of $308\text{fT/cm}\sqrt{\text{Hz}}$, measured for a step-edge device. Such a sensitivity is among the best reported in the literature for a small SLG. Given the excellent sensitivities of the small SLGs these devices proved extremely useful for application in NDE at Strathclyde. The stability of these gradiometers was also excellent, an important requirement for a NDE sensor. The excellent sensitivities and relative inexpense of the small substrates (particularly the single crystals used for step-edge devices), make the small SLGs reported here attractive devices for many applications.

The large SLGs fabricated on the $30 \times 10\text{mm}^2$ were designed to offer the sensitivities required for the application of HTS devices in biomagnetism. Although the larger substrates are significantly more expensive than the standard $10 \times 10\text{mm}^2$ substrates, the increase in area is required to enable an increase in the device baseline l and an increase in the effective area of the pick-up loops A_{MAG}. Although the flux noise measured for the large devices was generally poorer than expected, the large l and A_{MAG} of the gradiometers resulted in record gradient sensitivities for devices fabricated from a single superconducting layer. The best step-edge device had a gradient sensitivity of $110\text{fT/cm}\sqrt{\text{Hz}}$, better than any value reported in the literature for a step-edge SLG. One of the bicrystal SLGs had a lower flux noise and thus had a better gradient sensitivity of $50\text{fT/cm}\sqrt{\text{Hz}}$ - the best ever achieved for an HTS SLG. The excellent sensitivities offered by the large SLGs made them suitable for application in the measurement of the biomagnetic signals of the adult heart. MCGs were recorded from healthy adult volunteers, either completely unshielded or with moderate shielding. Inside the aluminium room a signal-to-noise ratio of approximately 6 was achieved, while, with the devices cooled unshielded in the open laboratory a signal-to-noise ratio of approximately 2 was achieved. In the moderately shielded case the signal-to-noise ratios were sufficient to clearly see the

QRST structure of the heart signal when the data was averaged.

References

[1] *Physikalisch-Technische Bundesanstalt, Institute Berlin, Berlin.*

[2] J. Vrba in *SQUID Sensors: Fundamentals, Fabrication and Applications*, H. Weinstock (Ed.), Kluwer Academic Publishers, Dordrecht, (1996).

[3] D. Koelle, R. Kleiner, F. Ludwig, E. Dantsker and J. Clarke, Rev. Mod. Phys. 71, p.631 (1999).

[4] Y. Tarvin, Y. Zhang, M. Mück, A.I. Braginski and C. Heiden, IEEE Trans. Appl. Supercond. 3, p.2477 (1993).

[5] M.A. Epsy, R.H. Kraus, E.R. Flynn and A. Matlashov, Rev. Sci. Instrum. 69, p.123 (1998).

[6] R.H. Koch, J.R. Rozen, J.Z. Sun and W. Gallagher, Appl. Phys. Lett. 63, p.403 (1993).

[7] W. Eidelhoth, R. Oh, R.P. Robertazzi, W.J. Gallagher and R.H. Koch, Appl. Phys. Lett 59, p.3473 (1991).

[8] S. Knappe, D. Drung, T. Schurig, H. Koch, M. Klinger and J. Hinken, Cryogenics 32 p.881 (1992).

[9] L.R. Bär, G.M. Daalmans, K.H. Barthel, L. Ferchland, M. Kühnl and D. Uhl, Supercond. Sci Technol. 9, p.A87 (1996).

[10] G.M. Daalmans, L. Bär, M. Kühnl, D. Uhl, M. Selent and J. Ramos, IEEE Trans. Appl. Supercond. 5, p.3109 (1995).

[11] E. Il'ichev, L. Dörrer, F. Schmidl, V. Zakosarneko, P. Seidel and G. Hildebrant, Appl. Phys. Lett. 68, p.708 (1996).

[12] S. Wunderlich, F. Schmidl, H. Specht, L. Dörrer, H. Schneidwind, U. Hübber and P. Seidel, Supercond. Sci. Technol. 11, p.315 (1998).

[13] V. Schultze, R. Stolz, R. Ijsselsteijn, V. Zakosarenko, L. Fritzch, F. Thrum, E. Il'ichev and H.G. Meyer, IEEE Trans. Appl. Supercond. 7, p.3473 (1997).

[14] M.N. Keene, J.S. Satchell, S.W. Goodyear, R.G. Humphreys, J.A. Edwards, N.G. Chew and K. Lander, IEEE Trans. Appl. Supercond. 5, p.2923 (1995).

[15] Y.J. Tian, S. Linzen, F. Schmidl, L. Dörrer, R. Weidl and P. Seidel, Appl. Phys. Lett. 74, p.2197 (1998).

[16] E. Dantsker, O. Froehlich, S. Tanaka, K. Kouznetsov, J. Clarke, Z. Lu, V. Matijasvic and K. Char, Appl. Phys. Lett. 71, p.1712 (1997).

[17] K.A. Kouznetsov, J. Borgmann and J. Clarke, Appl. Phys. Lett. 75, p.1979 (1999).

[18] K.A. Kouznetsov, J. Borgmann and J. Clarke, Rev. Sci. Instrum. 71, p.2873 (2000).

[19] J.P. Wikswo, Jr. in *SQUID Sensors: Fundamentals, Fabrication and Applications*, H. Weinstock (Ed.), Kluwer Academic Publishers, Dordrecht, (1996).

[20] S. Wunderlich, F. Schmidl, L. Dörrer, H. Schneidewind and P. Seidel, IEEE Trans. Appl. Supercond. 9, p.71 (1999).

[21] C. Carr, A. Cochran, J. Kuznik, D. McA. Mckirdy and G.B. Donaldson, Cryogenics 36, p.691 (1996).

[22] C. Carr, E.J. Romans, J.C. Macfarlane, A. Eulenburg, C.M Pegrum and G.B. Donaldson, Proceedings from the Third European Conference on Applied Superconductivity, Inst. Phys. Conf. Ser. 158 p.747 (1997).

[23] C. Carr, E.J. Romans, A.J. Millar, A. Eulenburg, G.B. Donaldson and C.M. Pegrum, IEEE Trans. Appl. Supercond. 11, p.1367 (2000).

[24] L. Hao, J.C. Macfarlane, D.A. Peden, R.A.M. Lee, J.C. Gallop and C. Carr, IEEE Trans. Appl. Supercond. 11, p.635 (2001).

[25] F. Ludwig, A.B.M. Jansman, D. Drung, M.O. Lindström, S. Bechstein, J. Beyer, J. Flokstra and T. Schurig, IEEE Trans. Appl. Supercond. 11, p.1315 (2001).

[26] A. Eulenburg, *High Temperature Superconducting Thin Films and Quantum Interference Devices (SQUIDs) for Gradiometers*, PhD thesis, University of Strathclyde (1999).

[27] A. Eulenburg, E.J. Romans, C. Carr, A.J. Millar, G.B. Donaldson and C.M. Pegrum, Appl. Phys. Lett. 75, p.2301 (1999).

Chapter 6

The Gradiometric SQUID

Chapter 5 detailed the performance of three designs of conventional narrow-linewidth SQUID single-layer gradiometer (SLG). The shielded gradient sensitivities of the best devices were excellent in comparison with the figures reported in the literature for SLGs fabricated by other groups. When cooled in the open laboratory the flux noise of the gradiometers was found to increase, typically by a factor of 3-5, as a consequence of the direct pick-up of environmental interference. This chapter describes the gradiometric SQUID (G-SQUID) - a device which utilises the topological freedom of the step-edge technology, and is designed for incorporation into SLGs to improve their characteristics in unshielded environments. Two generations of G-SQUID devices were fabrictated and tested.

The first section of this chapter outlines the response of a first-order gradiometer, and includes an overview of some of the techniques that have been reported in the literature to improve the characteristics of the gradiometer response for unshielded operation. The remaining sections in the chapter describe the two generations of G-SQUID devices and their improved characteristics for unshielded use.

6.1 Introduction

6.1.1 SQUID gradiometer response

An ideal first order gradiometer is sensitive only to field gradients of first and higher order. However for conventional directly coupled SQUID gradiometers, an unwanted uniform field response limits the unshielded performance of the device. This response is a characterised by the device's parasitic effective area A_{PAR}. For the SQUID gradiometer shown in Figure 6.1, the electronic response of the device

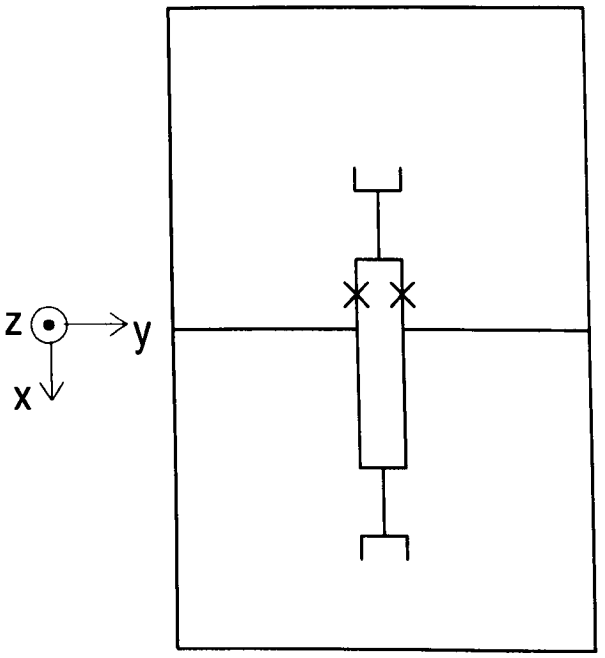

Figure 6.1: Schematic diagram showing a conventional single-layer SQUID gradiometer with reference co-ordinates. The SQUID in the centre of the device is enlarged for clarity.

to the static field $B_z(x, y)$ can be expressed as

$$V \propto l\frac{\partial B_z}{\partial x}A_{\mathrm{GRAD}} + B_z A_{\mathrm{PAR}} \tag{6.1}$$

where l is the baseline of the gradiometer, A_{GRAD} is the effective area of the device to first order fields, $\partial B_z/\partial x$ and B_z are the first-order field gradient and uniform field respectively and second and higher-order terms have been neglected. The parasitic effective area can be considered to have two components

$$A_{\mathrm{PAR}} = A_{\mathrm{SQ}} + A_{\mathrm{DEF}} \tag{6.2}$$

where A_{SQ} is the uniform field effective area of the SQUID and A_{DEF} is the uniform field effective area arising from any defects or imperfections in the device structure that may occur during fabrication. For conventional single-layer SQUID gradiometers, $A_{\mathrm{SQ}} \gg A_{\mathrm{DEF}}$, and Equation 6.2 can be approximated as $A_{\mathrm{PAR}} \approx A_{\mathrm{SQ}}$.

6.1.2 Improving gradiometers for unshielded operation

Gradiometers incorporating conventional SQUIDs of inductance 50-100pH typically have parasitic effective areas in the range 500-1000μm^2 [1]-[4]. An ideal first-order gradiometer should have $A_{PAR} = 0$ and thus a response that is proportional only to the $\partial B_z/\partial x$ term of Equation 6.1. In practice, with conventional narrow-linewidth SQUIDs, this is not possible as $A_{PAR} \approx A_{SQ}$ and $A_{SQ} \propto L_{SQ}$. With such SQUIDs reducing L_{SQ} and therefore A_{PAR} generally also reduces the mutual inductance between the pick-up loops and the SQUID L_M. A reduced L_M will result in a device with a smaller A_{MAG} (the effective area of the device operating with just one pick-up loop) and therefore a device with a poorer gradient sensitivity. This constraint, that by reducing A_{PAR} one generally reduces A_{MAG}, limits the balance ($b = A_{PAR}/A_{MAG}$) for conventional narrow-linewidth SQUID gradiometers - the non-zero uniform field response of the SQUID leads to an intrinsic device imbalance limiting the characteristics of the SLG for use in unshielded environments.

Several techniques have been developed which reduce the uniform field response of the SQUID. With low temperature superconductors (LTS), gradiometric SQUIDs [5] can be incorporated into gradiometers to improve the device balance (*e.g.* [6]). LTS gradiometric SQUIDs consist of a double-looped washer inductively coupled to the pick-up loops by a multiturn flux transformer. The double washer configuration results in the SQUID having a net zero response (ideally) to uniform fields. A similar device has been demonstrated in HTS with a flux transformer flip-chip coupled to a double washer gradiometric SQUID [7]. However due to difficulties in alignment associated with the flip-chip technique, and since multiple layers of YBCO films were required for the flux transformer, the balance and noise performance of this HTS device were poor. For single layer HTS devices, an electronic 2-SQUID coupling scheme has been used to improve gradiometer balance [8]. The device layout is such that, when added together the magnetometric signals of the two SQUIDs cancel. The signals are added electronically with the magnitude of the response from each SQUID weighted to optimise the balance. Some of the disadvantages of

this technique include the added complexity of using more than one SQUID channel, the need for additional room temperature electronics and that the intrinsic noise of the system is increased as a result of adding the outputs from the two SQUIDs. More significantly, as with the electronic gradiometers described in Chapter 5, the balance of the electronically combined signals is limited to a small frequency range. Further investigation showed that it is difficult to maintain optimum balance when the system is operated in an unshielded environment [9].

The G-SQUID developed during the course of this work, improves the gradiometer balance intrinsically and does not have the problems associated with the techniques that have been used in HTS described above: the G-SQUID requires only a single layer of superconductor thus avoiding the problems associated with multi-layer devices and the flip-chip technique, and only a single SQUID channel is required without the need for any additional electronics which impose restrictions on the bandwidth over which high balance levels can be achieved.

6.2 First Generation G-SQUIDs

In this section the realisation of a HTS first-order gradiometric SQUID made from a single layer of superconductor is described. The design, fabrication and measured electrical properties of the first generation of gradiometric SQUID (G-SQUID) devices are described. Both uncoupled (autonomous) G-SQUIDs and G-SQUIDs coupled to single-layer gradiometers were characterised.

6.2.1 Design

A completed G-SQUID is shown in Figure 6.2(a), and for clarity the layout of the superconducting layer is shown in Figure 6.2(b). The G-SQUID has two identical loops connected in parallel across two step-edge Josephson junctions. The symmetric two loop structure of the superconducting layer of the G-SQUID results in the device theoretically having no response to uniform fields (*i.e.* $A_{PAR} = 0$). The

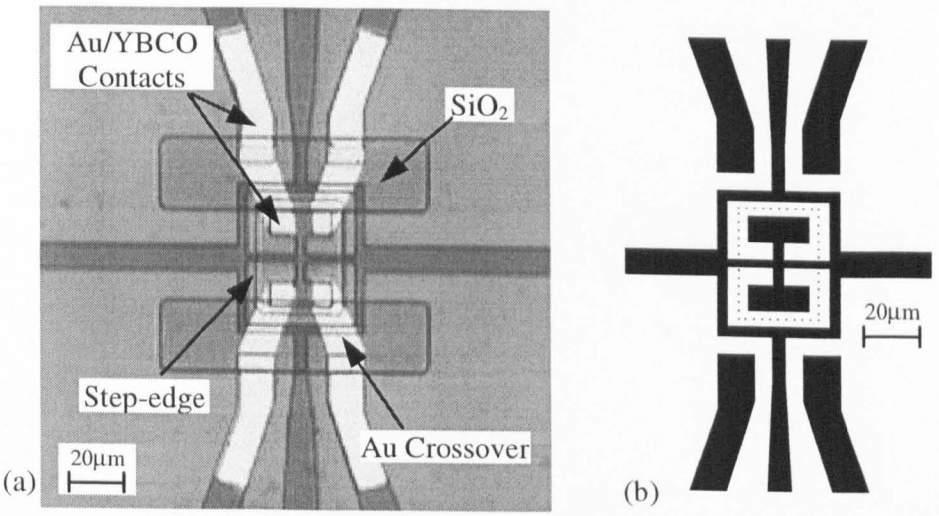

Figure 6.2: (a) An optical micrograph of a completed G-SQUID showing the gold cross-over structure with SiO_2 insulating layer. (b) The symmetric layout of the YBCO layer of the G-SQUID. The dotted line indicates the location of the step-edge.

linewidth of the G-SQUID was restricted to 4μm to prevent flux penetration when the device is operated unshielded [10]. The junctions have a width of 3μm. The horizontal track of superconductor connected to the G-SQUID is the signal injection path coupling the pick-up loops to the G-SQUID - in the case of the autonomous G-SQUID it allows direct modulation by current injection. Connections to the centre of the device are realised by gold cross-overs with a SiO_2 insulating layer to prevent contact to the G-SQUID loops. Not all of the contacts to the G-SQUID are required for four-terminal measurements; the chosen layout, with redundant contacts, maintains perfect symmetry in the design of the superconducting layer, ensuring that theoretically $A_{\mathrm{PAR}} = 0$.

A single-layer gradiometer was designed, incorporating three G-SQUIDs. The layout of the gradiometer shown in Figure 6.3 is similar to that of the first generation gradiometer design used with the conventional SQUIDs described in Chapter 5. The gradiometer has a baseline of $l = 4.2$mm and pick-up loops with a linewidth of 500μm giving an estimated loop inductance of $L_{\mathrm{LP}} = 7$nH.

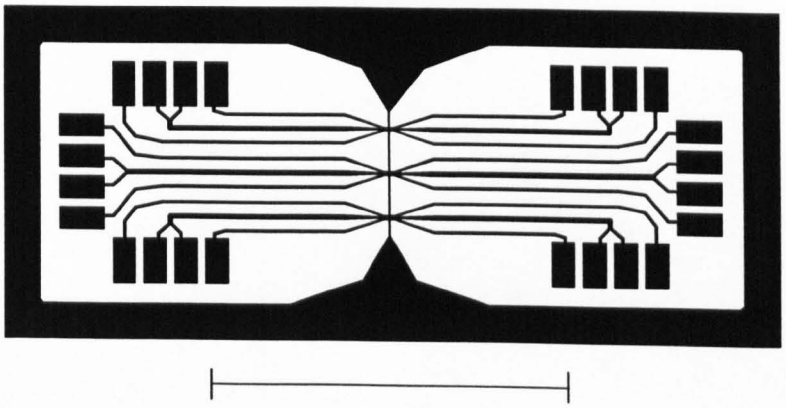

Figure 6.3: The layout of the YBCO layer of the single-layer gradiometer with three identical directly coupled G-SQUIDs in the centre. Note that this figure is rotated through 90° with respect to Figure 6.2.

6.2.2 Fabrication

The G-SQUID devices were fabricated on $10 \times 10\text{mm}^2$ STO substrates with the step-edges prepared as described in Section 3.2. The mill time was controlled to produce steps of height $h = 300 \pm 30\text{nm}$ to maximise the yield of RSJ-like devices as discussed in Chapter 3. Each STO chip consisted of 5 G-SQUID devices: 3 coupled to a single-layer gradiometer and 2 autonomous devices with connections for direct current injection. YBCO films of thickness 200nm were grown on the step-edge substrates, followed immediately by the deposition of a dc sputtered *ex-situ* gold film of thickness 200nm. The chips were then annealed at a temperature of 475°C in 0.8atm O_2 for 1hr to improve the contact resistance. The Au/YBCO bi-layer was patterned using standard photolithography and argon ion-milling in two stages: the first to form the YBCO structure of the device (Figure 6.4(a)), the second to remove the excess gold leaving just the contact pads for the cross-overs (Figure 6.4(b)). SiO_2 films of thickness 300nm were then deposited by rf sputtering and patterned using lift-off to form the insulating layer, using the procedures described in Chapter 2. Finally, a second layer of gold was deposited on each chip and patterned into cross-overs to allow contact to the central pads of each G-SQUID (Figure 6.4(c)). Figure 6.4(d) is an SEM image of the corner of a loop of a G-SQUID device showing

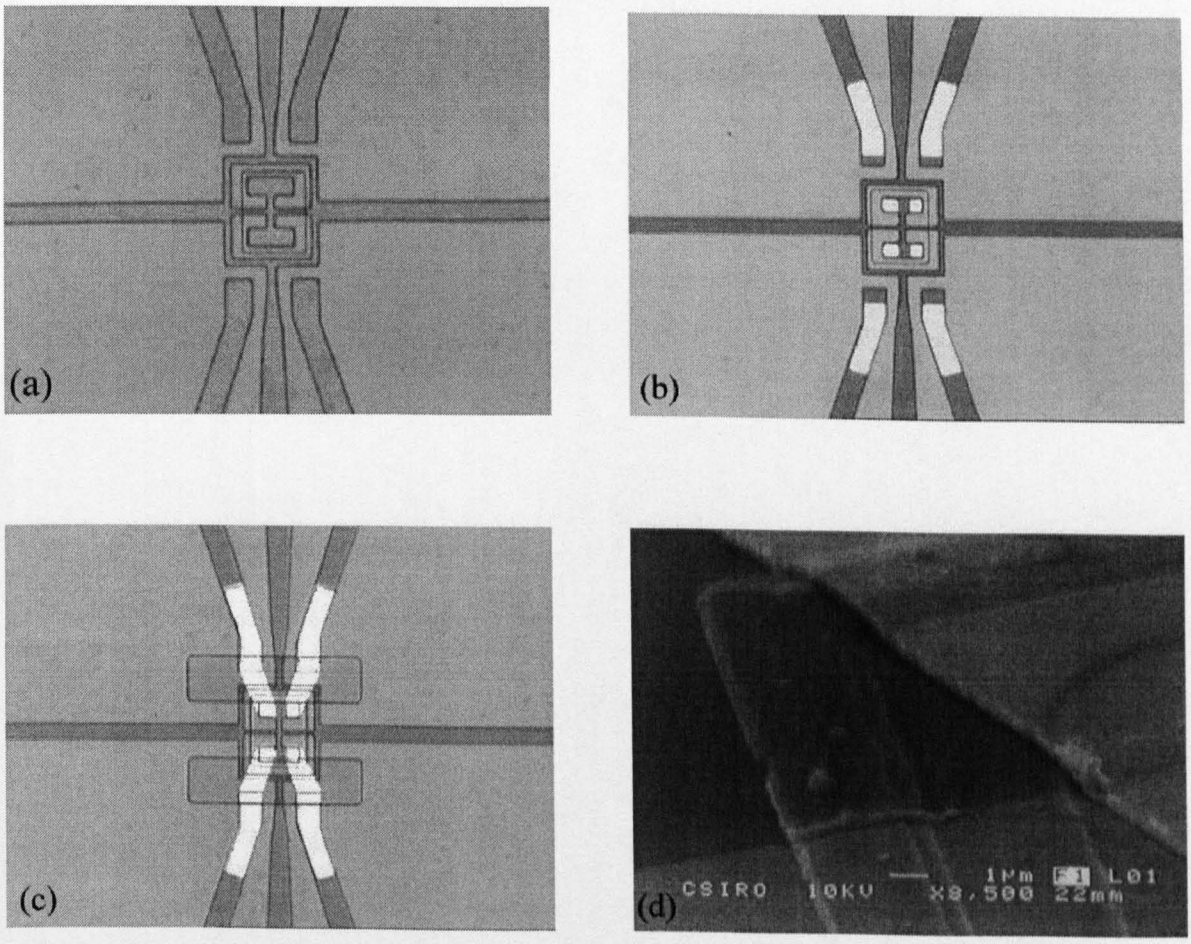

Figure 6.4: Optical micrographs showing the stages of fabrication for a G-SQUID device: (a) The Au/YBCO bi-layer is patterned to form the YBCO structure; (b) the excess gold is removed; (c) the SiO_2 insulating layer and gold cross-over structure is patterned. (d) An SEM image of the corner of a G-SQUID loop showing the patterned YBCO track with SiO_2 insulating layer and gold cross-over (top-right section of the image). The step-edge can be seen in the bottom-right corner of the micrograph. This image was taken at CSIRO with assistance from Dr Cathy Foley.

the YBCO loop with SiO_2 insulator and gold cross-over layer.

Preliminary measurements showed that the immediate *ex-situ* deposition of gold after the growth of the YBCO film and the subsequent annealing result in a contact resistance of better than $10^{-6}\Omega cm^2$. Using the two gold layers as described above, rather than simply patterning a single gold layer after the SiO_2 lift-off process, allowed the fabrication of cross-overs of sufficiently small resistance $\leq 1\Omega$ such that they make no significant contribution to the measured flux noise of the G-SQUIDs.

To ensure that the overlying SiO_2 had no detrimental effects on the YBCO of the G-SQUID loop underneath, several test YBCO microbridges were fabricated and then patterned with a covering SiO_2 strip. There was no discernible change in the T_C or J_C of the microbridges after patterning the SiO_2 layer, in agreement with reports in the literature [11, 12].

6.2.3 Device inductances

The equivalent circuit of the G-SQUID is shown in Figure 6.5. The inductance of the G-SQUID is given by

$$L_{SQ} = \frac{L_A}{2} + L_B, \tag{6.3}$$

where $L_A = L_{A1} = L_{A2}$.

The mutual inductance L_M between the G-SQUID and the pick-up loops of a directly coupled single-layer gradiometer is calculated as follows. If one considers fluxoid quantisation around each of the two G-SQUID loops then the phase differences δ_1 and δ_2 across the two junctions must satisfy the condition that

$$\delta_1 - \delta_2 = 2\pi\frac{\Phi_1}{\Phi_0} + 2m\pi = -2\pi\frac{\Phi_2}{\Phi_0} + 2n\pi, \tag{6.4}$$

where Φ_1 and Φ_2 are the total fluxes in each loop, Φ_0 is the flux quantum and m and n are integers. Note that for a conventional single loop SQUID the integral multiples of 2π in Equation 6.4 can be discarded as having no physical meaning, but in this case they signify the condition that the total flux $(\Phi_1 + \Phi_2)$ in the G-

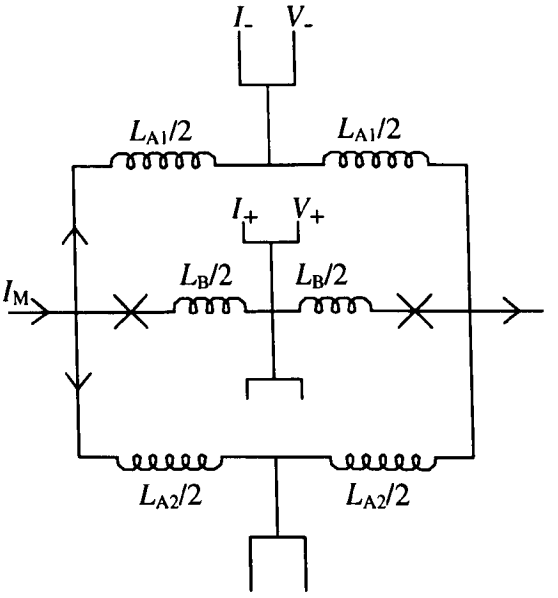

Figure 6.5: Equivalent circuit of the G-SQUID. Each of the inductors described in the main text, L_{A1}, L_{A2} and L_B, is shown split into two equal elements so that the position of the electrical connections can be indicated clearly.

SQUID is quantised. A SQUID has a response which varies as $\cos((\delta_1 - \delta_2)/2)$. From Equation 6.4 and since $\cos(x + 2m\pi) = \cos(-x + 2n\pi)$ it follows that the G-SQUID response can be considered a periodic function of *either* Φ_1 or Φ_2 with periodicity Φ_0. Thus only the flux in one loop of the G-SQUID need be considered to calculate L_M. The net current I_M from the pick-up loops (indicated in Figure 6.5) divides equally through L_{A1} and L_{A2}, so that equal and opposite fluxes are added to the two loops, thus preserving the total flux quantisation condition in the G-SQUID. So the flux injected in the upper loop is

$$\Phi = \frac{I_M}{2}(L_{A1} - M_A) - I_M M_I, \tag{6.5}$$

where M_A is the mutual inductance between between L_{A2} and the upper loop and M_I is the mutual inductance between the input line from the pick-up loops and the upper loop. Thus the effective mutual inductance L_M between the pick-up loops and the G-SQUID is given by

$$L_M = \frac{1}{2}(L_A - M_A) - M_I. \tag{6.6}$$

Parameter	L_A	L_B	M_A	M_I	L_{SQ}	L_M
Inductance (pH)	67	33	6	2	67	25

Table 6.1: modeled and calculated inductances of the G-SQUID.

The modeling package FASTHENRY was used to estimate the various inductances discussed above. Table 6.1 lists the modeled values and the subsequently calculated inductances L_{SQ} and L_M.

6.2.4 Results and Discussion

Electrical Characterisation

Two chips were fabricated and tested, each consisting of two autonomous devices and one gradiometer incorporating three G-SQUIDs. On one of the chips (SE37), two of the G-SQUIDs were damaged during fabrication. Of the remaining eight tested four exhibited RSJ-like I-V characteristics and showed voltage modulation; there was no observable supercurrent in the other four G-SQUIDs. The poor yield of G-SQUIDs was not entirely unexpected given the significant increase in the number of patterning stages in the fabrication process compared to the fabrication of a conventional SQUID device. Damaged to the YBCO and oxygen losses in the film that may occur during the fabrication process are likely to contribute to the poor relatively poor yield of working G-SQUIDs.

The measured electrical properties of the four working devices are shown in Table 6.2. The junction parameters I_C, R_N and I_CR_N for each G-SQUID were extracted from I-V curves measured inside a single layer of mu-metal shielding using the set-up described in Section 3.3. Only G-SQUID SE38-B exhibited an I_CR_N product much lower than the mean value of 130μV that was achieved for the step-edge junctions discussed in Chapter 3. The maximum voltage modulation depth ΔV was measured for each G-SQUID using direct modulation, inside a single layer of mu-metal shielding. From the measured periodicity $\Delta I_M = 90\mu$A of the

Device Number	Autonomous /Coupled	I_C (μA)	R_N (Ω)	$I_C R_N$ (μV)	ΔV (μV)	White Noise ($\mu\Phi_0/\sqrt{\text{Hz}}$)
SE37-A	Autonomous	16	8.0	128	19	10
SE37-B	Coupled	50	2.1	105	3	50
SE38-A	Autonomous	32	3.2	102	5	22
SE38-B	Coupled	5	11	55	16	–

Table 6.2: The measured electrical properties of four G-SQUID devices. The white noise of SE38-B was not measured.

V-Φ curves shown in Figure 6.6(a), the coupling inductance was found to be $L_M = \Phi_0/\Delta I_M \approx 23$pH which is in good agreement with the modeled value of 25pH. To measure the intrinsic noise of the G-SQUIDs, the devices were cooled inside 3 layers of mu-metal shielding and operated in a flux-locked loop (FLL) as described for the conventional SQUID devices in Chapter 4. The figures shown in Table 6.2 for the noise measured at 1kHz using dc bias are broadly similar to those measured for the conventional SQUIDs of similar inductance discussed in the previous chapter. The lowest measured flux noise ($10\mu\Phi_0/\sqrt{\text{Hz}}$) was observed for autonomous device SE37-A, which had a I_C of 16μA and thus a screening parameter approximately equal to the optimum value of $\beta_L \approx 1$ [13] (taking the inductance of the G-SQUID as the modeled value of $L_{SQ} = 67$pH). Figure 6.7 shows the flux noise spectral density measured for SE37-A between 10Hz and 1000Hz measured using dc bias. The flux noise increases from approximately $10\mu\Phi_0/\sqrt{\text{Hz}}$ in the white noise region to approximately $22\mu\Phi_0/\sqrt{\text{Hz}}$ at 10Hz. $1/f$ noise makes a significant contribution to the noise below 200Hz which is not unexpected when using the dc-bias mode of operation.

Autonomous G-SQUID Effective Area

To measure the effective area of the G-SQUIDs, the devices were operated in FLL mode and placed in the centre of the 1.2m diameter Helmholtz coils used to measure the effective areas of the devices discussed in Chapter 5. A root-mean square magnetic field of approximately 1μT was generated by passing an ac current through the coils with the resulting SQUID output lock-in detected. The frequencies

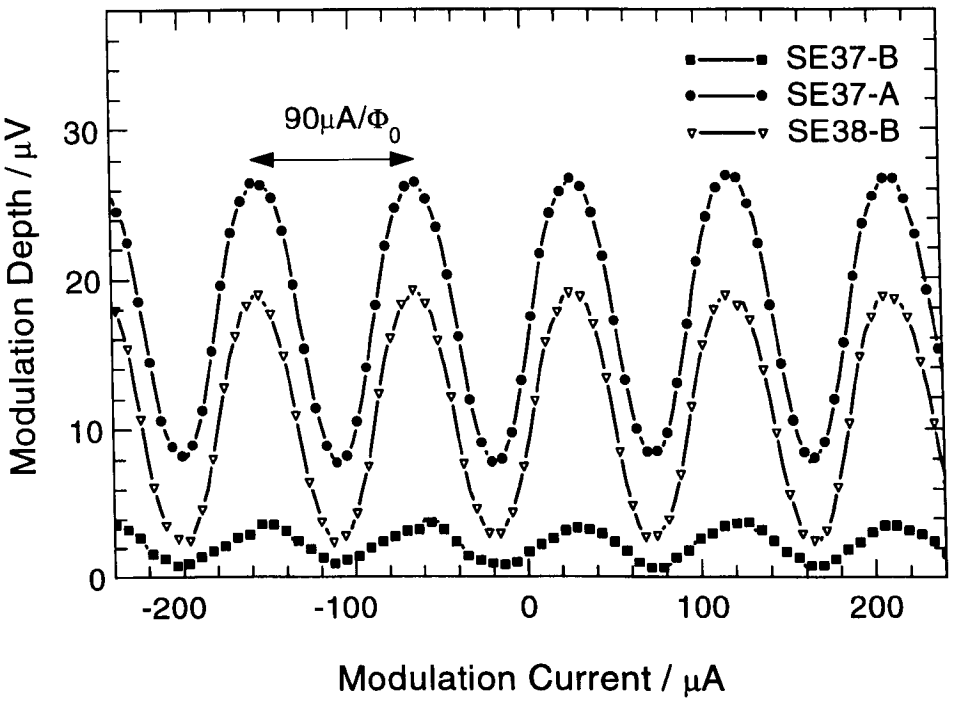

Figure 6.6: The V-Φ curves measured for three of the G-SQUIDs using direct modulation, showing the maximum peak-to-peak modulation obtained for each device. The position of the minima of each curve has been aligned and have been shifted on the y-axis to clearly show the periodicity and maximum voltage modulation of each curve.

used were between 120Hz and 320Hz.

Repeated testing of the two autonomous G-SQUIDs, through multiple cool-downs, resulted in measured effective areas of $A_{SQ} \sim 2\mu m^2$. Although ideally the G-SQUID should have zero response to uniform fields, the measured value is not unreasonable given the scale of imperfections likely in the photolithography and the consequent difference we might expect between the areas of the two G-SQUID loops.

Gradiometer Performance

For the G-SQUID coupled to the SLG (device SE37-B) a parasitic effective area of $A_{PAR} \approx 95\mu m^2$ was measured, more than five times smaller than the parasitic effective areas reported in the literature for conventional narrow-linewidth SQUID SLGs. On cutting one of the G-SQUID gradiometer pick-up loops, an effective area for the single pick-up loop was measured as $A_{MAG} \approx 0.04mm^2$ thus yielding a device balance of $b = A_{PAR}/A_{MAG} \approx 1/300$ - a factor of three better than was achieved for

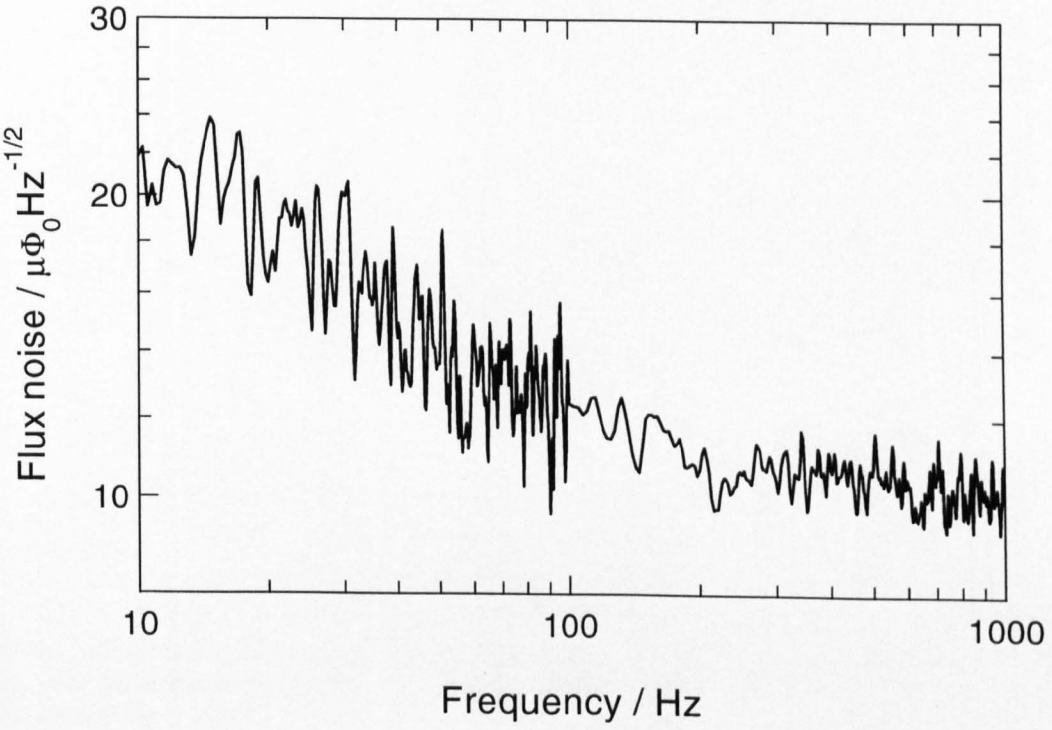

Figure 6.7: (a) The flux noise spectral density of G-SQUID SE37-A measured inside three layers of mu-metal using dc bias mode.

the first generation small SLG in Chapter 5 that had pick-up loops of similar design and incorporated conventional SQUIDs with a similar self inductance to that of the G-SQUID.

The effective area A_{PAR} measured for the coupled G-SQUID is significantly larger than the effective area A_{SQ} measured for the autonomous G-SQUIDs. This suggests the source of imbalance is related to the gradiometer pick-up loops (*i.e.* Equation 6.2 reduces to $A_{\mathrm{PAR}} \sim A_{\mathrm{DEF}}$). This could be accounted for by differences in the areas of the two gradiometer pick-up loops due to photolithography tolerances and/or any imperfections due to damage caused during fabrication. This was confirmed by cutting the remaining pick-up loop the G-SQUID SLG device (SE37-B) and measuring an effective area of $A_{\mathrm{SQ}} \sim 2\mu\mathrm{m}^2$.

The flux noise of the G-SQUID gradiometer was recorded both with the device inside three layers of mu-metal shielding and with the device cooled in the open laboratory. The resulting noise spectra obtained with the FLL electronics operating in ac-bias mode are shown in Figure 6.8. The noise spectra were flat from 1kHz

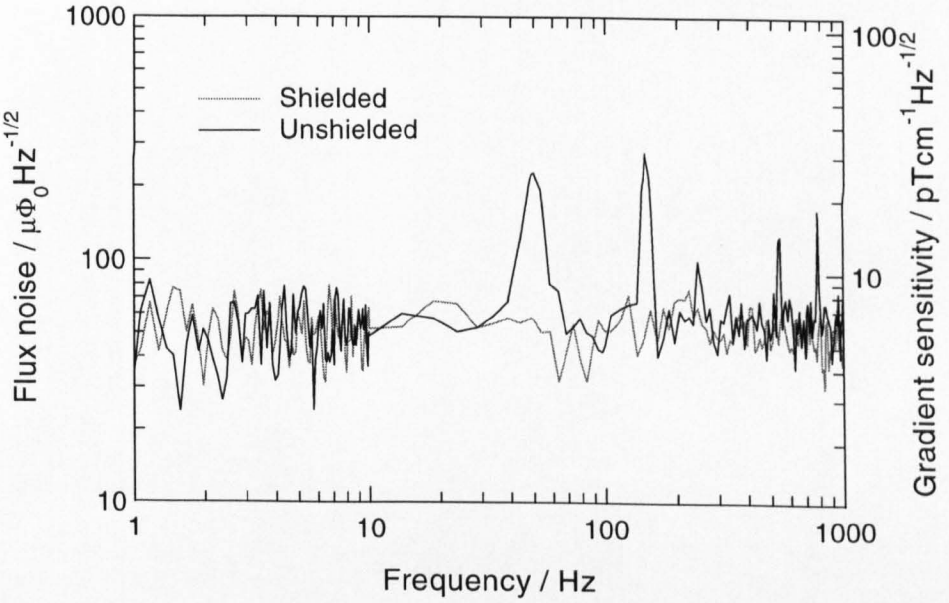

Figure 6.8: The flux noise spectral density measured for G-SQUID gradiometer SE37-B. The spectra were recorded using 64kHz *ac bias. Both shielded (three layers mu-metal) and unshielded spectra are shown.*

down to 1Hz, with the flux noise approximately $\sqrt{S_\Phi} = 50\mu\Phi_0/\sqrt{\text{Hz}}$ for both the shielded and unshielded cases. This corresponds to a gradient sensitivity of $\sqrt{S_\text{g}} = \sqrt{S_\Phi}/lA_\text{MAG} \approx 6\text{pT/cm}\sqrt{\text{Hz}}$.

In contrast to the noise spectra of the conventional SQUID gradiometers discussed in Chapter 5, for the G-SQUID gradiometer there is no discernible increase in flux noise for the device cooled in the open laboratory. The 50Hz mains peak in the unshielded spectra is significantly suppressed in the G-SQUID gradiometer compared with the unshielded spectra of the conventional SQUID SLGs discussed in Chapter 5. These improved unshielded noise characteristics are a consequence of the reduced uniform field response of the G-SQUID device.

6.3 Second Generation G-SQUIDs

Although the first generation G-SQUID SLGs exhibited small parasitic effective areas, their gradient sensitivity and balance was limited by the device's small A_MAG - a consequence of the poor inductance mismatch and the relatively small geometrical

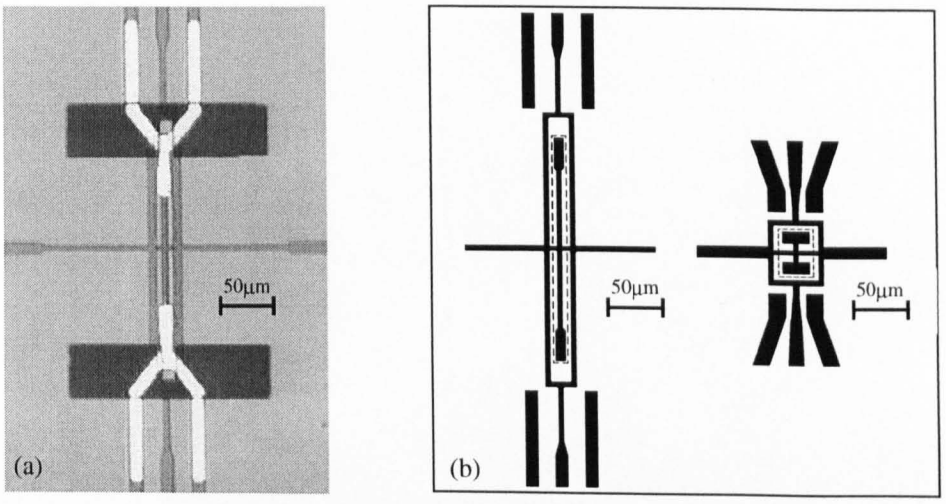

Figure 6.9: (a) An optical micrograph of a completed second generation G-SQUID. (b) The layout of the symmetric YBCO layer of the second generation G-SQUID (left), with the layout of the first generation device (right) shown to the same scale, for comparison. The dotted lines indicate the location of the step-edges.

area of the SLG pick-up loop (note that the pick-up loop area of the first generation SLG was restricted to allow room for the autonomous devices). In this section design and performance of the improved second generation of G-SQUID SLGs is described. The fabrication of the second generation devices used identical processes to those described in Section 6.2.2 used for the first generation devices. The second generation G-SQUIDs were also fabricated on $10 \times 10\text{mm}^2$ substrates, with each chip consisting of an SLG incorporating three G-SQUIDs - no autonomous second generation G-SQUIDs were fabricated.

6.3.1 Design

The relatively small mutual inductance between the pick-up loops and the G-SQUID hindered the performance of the first generation devices. Figure 6.9(a) is an optical micrograph of a completed second generation G-SQUID, with the layout of the superconducting layer of both the first and second generation G-SQUIDs, shown for comparison in Figure 6.9(b). The second generation device was designed with a longer and thinner structure to reduce the mutual inductances M_{A} and M_{I}, thus increasing L_{M}. To further increase L_{M}, the inductance L_{A} was increased, result-

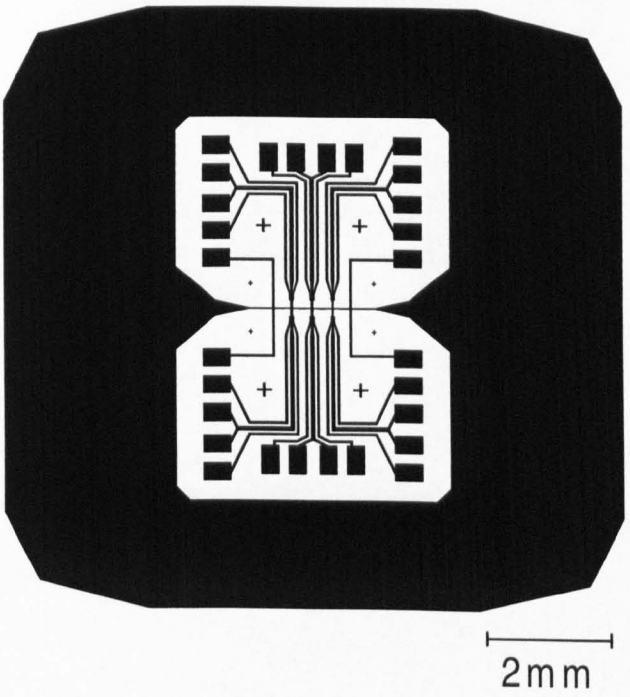

Figure 6.10: The layout of the YBCO layer of the second generation G-SQUID SLG with three identical directly coupled second generation G-SQUIDs in the centre.

ing in an increased SQUID inductance L_{SQ}. For the second generation G-SQUID FASTHENRY yields a mutual inductance of $L_M = 74$pH and SQUID inductance of $L_{SQ} = 98$pH resulting in ratio of $L_M/L_{SQ} \approx 76\%$. This is a significant improvement over the first generation design for which the modeled inductances yielded $L_M/L_{SQ} \approx 37\%$. The longer and thinner design of the second generation G-SQUID resulted in an increased fraction of the total SQUID inductance being coupled to the pick-up loops.

In addition to redesigning the G-SQUID, the pick-up loops of the SLG were also redesigned as shown in Figure 6.10. This design is similar to the that of the second generation conventional SQUID SLGs discussed in Chapter 5. The geometrical area of the gradiometer is significantly larger than the first generation G-SQUID SLG, and has increased linewidth to reduce the inductance of the pick-up loops. This design has a baseline of $l = 3.6$mm and an estimated pick-up loop inductance of $L_{LP} = 10$nH, resulting in an inductance mismatch of $L_M/L_{LP} = 1/135$. This is more than a factor of two of an improvement over the first generation G-SQUID SLGs

Device Number	I_C (μA)	R_N (Ω)	$I_C R_N$ (μV)	ΔV (μV)	White Noise ($\mu\Phi_0/\sqrt{\text{Hz}}$)
SE51-A	27	4.2	113	7	55
SE51-B	11	8.6	95	3	58

Table 6.3: The measured electrical properties of the two second generation G-SQUID devices.

which had an inductance mismatch of $L_M/L_{LP} = 1/280$.

6.3.2 Results and Discussion

The methods used to characterise the second generation G-SQUID were identical to those used for the first generation devices. On the second generation chip, two of the three G-SQUIDs had RSJ-like I-V characteristics and exhibited periodic voltage modulation as a function of applied flux. The bias current of each SQUID was optimised to obtain the maximum voltage modulation depth ΔV, and both SQUIDs were operated in a FLL inside three layer of mu-metal shielding to measure their intrinsic white flux noise. The measured electrical properties of the second generation G-SQUIDs are shown in Table 6.3.

The V-Φ curves of the two G-SQUIDs, measured for optimum bias using direct current injection are shown in Figure 6.11. The periodicity of the curves is approximately $\Delta I_M = 28\mu$A, which implies a mutual coupling inductance of $L_M = \Phi_0/\Delta I_M \approx 77$pH, which is in good agreement with the modeled value of 74pH.

The second generation G-SQUIDs had measured effective areas of $A_{PAR} \approx 30\mu\text{m}^2$, and $A_{MAG} \approx 0.15\text{mm}^2$, thus yielding a device balance of $b \approx 1/5000$. Due to the small parasitic effective area of the device, the second generation G-SQUID SLG has a balance that is more than an order of magnitude better than the values of approximately 1/100 to 1/300 typically achieved for conventional SQUID SLGs fabricated on $10 \times 10\text{mm}^2$ substrates.

As with the first generation devices, there was no evidence of any increase in the flux noise of the second generation G-SQUID gradiometers when cooled in the

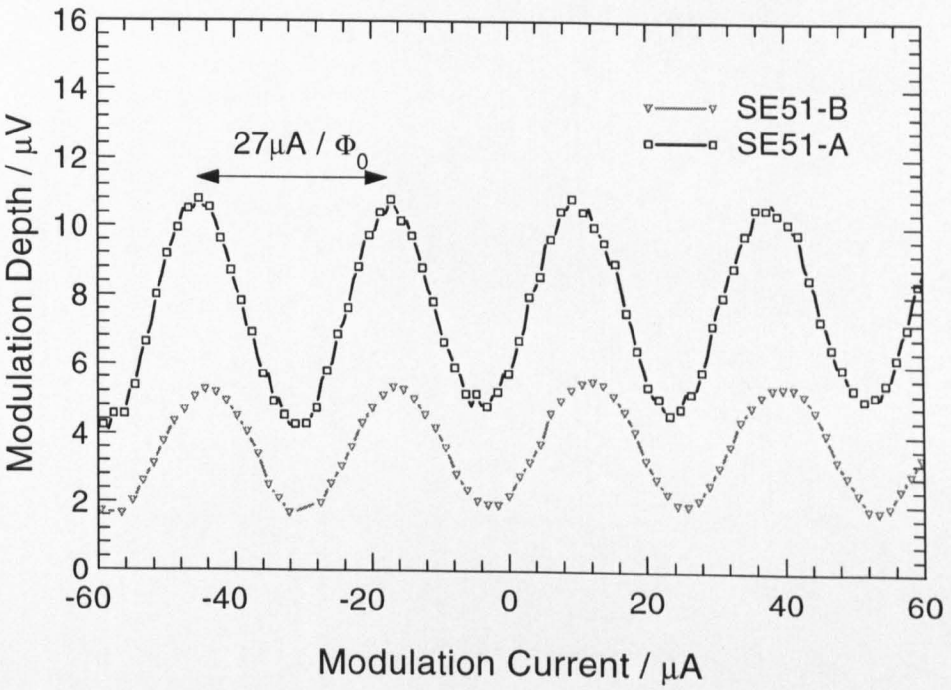

Figure 6.11: The V-Φ curves measured for the two second generation G-SQUIDs using direct modulation, showing the maximum peak-to-peak modulation obtained for each device.

open laboratory - as one might expect for a device which such a level of intrinsic balance. Figure 6.12 shows the shielded and unshielded flux noise spectra measured for a second generation G-SQUID SLG. Given the baseline of $l = 3.6\text{mm}$ and the measured $A_{\text{MAG}} = 0.15\text{mm}^2$ of the second generation device the white flux noise for both the shielded and unshielded cases of approximately $\sqrt{S_\Phi} = 55\mu\Phi_0/\sqrt{\text{Hz}}$, corresponds to a gradient sensitivity of $\sqrt{S_\text{G}} \approx 2\text{pT/cm}\sqrt{\text{Hz}}$.

6.4 Summary

This chapter described the development of a novel SQUID with improved characteristics for incorporation in SLGs. The design, fabrication and calculation of the G-SQUID inductance L_{SQ} and L_{M} were described. The G-SQUID is fabricated from a single layer of YBCO and is designed such that theoretically it has no parasitic effective area. Two generations of G-SQUID devices were fabricated and characterised. With the first generation devices an effective area of $A_{\text{SQ}} \sim 2\mu\text{m}^2$ was

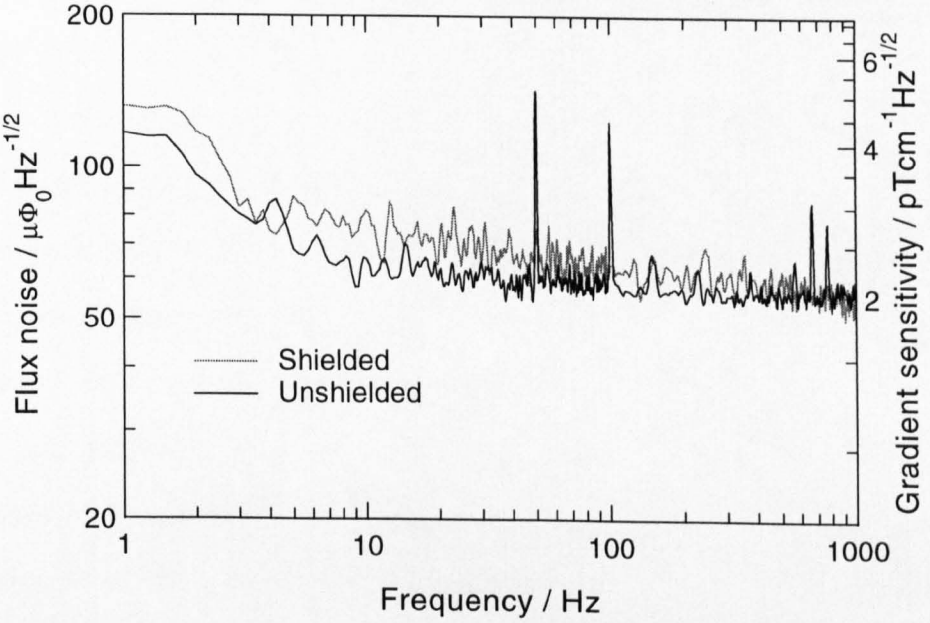

Figure 6.12: The flux noise spectral density measured for the second generation G-SQUID SLG (device number SE51-A). Both shielded and unshielded spectra were measured using dc bias.

measured, more than two orders of magnitude smaller than the effective areas one would expect to measure for an autonomous conventional SQUID of similar inductance. The residual uniform field response measured almost certainly arises from imperfections in the fabrication procedure. For a SLG incorporating a first generation G-SQUID an effective area of $A_{\mathrm{PAR}} = 95\mu\mathrm{m}^2$ was measured, approximately five times smaller than the values measured for SLGs incorporating conventional SQUIDs of similar inductance. By cutting the gradiometer's pick-up loops and measuring an effective area similar to that of the autonomous G-SQUID, it was confirmed that this uniform field response must originate in the pick-up loops. The G-SQUID's very small effective area is such that the SQUID in the centre of a SLG no longer need limit the balance of the device.

The second generation G-SQUIDs had several improvements in their design. By making the G-SQUIDs loops longer and thinner, and by increasing the SQUID inductance, the ratio of $L_{\mathrm{M}}/L_{\mathrm{SQ}}$ was significantly increased. The second generation G-SQUID gradiometer had a larger flux capture area and given the increase in L_{M} this resulted in a significantly larger A_{MAG} than that measured for the first genera-

tion devices. Due to the small parasitic effective area of the G-SQUIDs, the second generation G-SQUID SLG had a device balance of 1/5000, more than an order of magnitude better than the balance of SLGs fabricated on $10 \times 10\text{mm}^2$ substrates incorporating conventional SQUIDs. Given that similar a white flux noise was measured for both generations of G-SQUID SLGs, the increase in A_{MAG} resulted in an improved gradient sensitivity for the second generation device. The measured sensitivity of $2\text{pT/cm}\sqrt{\text{Hz}}$ was however slightly disappointing - a consequence of the high flux noise of the device. Relatively small $I_{\text{C}}R_{\text{N}}$ products and high flux noise values were a problem with many of the G-SQUID devices - most likely due to degradation of the sample during the long fabrication process. The white flux noise of $10\mu\Phi_0/\sqrt{\text{Hz}}$ measured for one of the G-SQUIDs does indicate that a low flux noise can be achieved, although clearly improvements are required in the fabrication process if such performance levels are to be achieved routinely. Despite the disappointing flux noise performance of the G-SQUID SLGs, in contrast with SLGs incorporating conventional SQUIDs, there is no increase in the flux noise when the devices are operated unshielded - a consequence of their small parasitic effective areas.

References

[1] E. Dantsker, O. Froehlich, S. Tanaka, K. Koiznetsov, J. Clarke, Z. Lu, V. Matijasevic and K. Char, Appl. Phys. Lett. 71, p.1727 (1997).

[2] Y.J. Tian, S. Linzin, F. Schmidl, L. Dörrer, R. Weidl and P. Seidel, Appl. Phys. Lett. 74, p.1302 (1999).

[3] C. Carr, A. Eulenburg, E.J. Romans, C.M. Pegrum and G.B. Donaldson, Supercond. Sci. Technol. 11, p.1317 (1998).

[4] C.M. Pegrum, A. Eulenburg, E.J. Romans, C. Carr, A.J. Millar and G.B. Donaldson, Supercond. Sci. Technol. 12, p.766 (1999).

[5] J.E. Zimmerman, J. Appl. Phys. 42, p.4483 (1971).

[6] G. Lang, D. Hutson, R. Weston, R.J.P. Bain, P. Maas, C.M. Pegrum. U. Shahani, A.I. Weir and G.B. Donalson, Proceedings of the Second European Conference on Applied Superconductivity, Inst. Phys. Conf. Ser. 148, p.1573 (1995).

[7] M.N. Keene, N.G. Chew, S.W. Goodyear, J.A. Edwards, R.G. Humphreys, K. Lander and J.S. Satchell, Physica C 230, p.110 (1994).

[8] A. Eulenburg, E.J. Romans, C. Carr, A.J. Millar, G.B. Donaldson and C.M. Pegrum, Appl. Phys. Lett. 75, p.2301 (1999).

[9] C. Carr, E.J. Romans, A.J. Millar, A. Eulenburg, G.B. Donaldson and C.M. Pegrum, IEEE Tran. Appl. Supercond. 11, p.1367 (2001).

[10] E. Dantsker, S. Tanaka and J. Clarke, Appl. Phys. Lett. 70, p.2037 (1997).

[11] M. Ban, K. Suzuki and Y. Enomoto, Physica C 290, p.345 (1997).

[12] J. Du, K.E. Leslie, C.P. Foley, G.L. Harding, B. Sankrithyan and D.L. Tilbrook, Supercond. Sci. Technol. 12, p.1027 (1999).

[13] C.D. Tesche and J. Clarke, J. Low Temp. Phys. 29, p.301 (1977).

Chapter 7

Conclusions and Future Work

The two main objectives of this work were to develop step-edge junctions as an alternative to the use of bicrystal substrates and to develop SQUID gradiometers with an emphasis on improving their characteristics for operation in unshielded environments. The main achievements that have been described in earlier chapters to meet these goals shall now be summarised. Following this, suggestions are given for future directions related to the work described in this thesis.

7.1 Step-Edge Devices

Chapter 3 described the fabrication and properties of step-edge junctions with reference to the characteristics of bicrystal junctions. Using the controlled fabrication process described, the yield of RSJ-like junctions was comparable to that of the Strathclyde bicrystal junctions and to the yields achieved for step-edge junctions by other groups. The $I_C R_N$ products of the step-edge junctions were generally better than those of bicrystals, with a mean $I_C R_N$ of 130μV achieved for the step-edge junctions in comparison with a mean of 100μV obtained for the bicrystals. However, both the on-chip and the chip-to-chip spreads in the step-edge junction parameters were found to be slightly higher than those of bicrystal junctions. From $I_C(B)$ curves, the step-edge junctions were found to generally have excellent uniformity and characteristics suitable for incorporation in SQUIDs to be cooled in an unshielded environment.

Chapter 4 described the characteristics of step-edge junction SQUIDs. Four similar designs of narrow-linewidth SQUID, each with a different self inductance, were fabricated. The maximum voltage modulation depth of each SQUID was generally found to be significantly smaller than the theoretical values predicted by Enpuku

et al. (Equation 1.13 in Chapter 1). The main factor associated with measuring a smaller ΔV than predicted is believed to be asymmetries between the parameters of the two junctions in the SQUID. The intrinsic flux noise properties of the step-edge SQUIDs were similar to those reported by others. The white noise of all but two of the twenty-three step-edge SQUIDs was below $35\mu\Phi_0/\sqrt{\text{Hz}}$. The best step-edge SQUID had an intrinsic white flux noise of just $5\mu\Phi_0/\sqrt{\text{Hz}}$ which compares well with that of the best step-edge SQUID reported in the literature.

A comparison between the performance of step-edge and bicrystal junction SQUIDs of the same design was included in Chapter 4. Despite the larger $I_C R_N$ values obtained for the step-edge junctions, there was in general no improvement in SQUID noise performance compared with that of the bicrystals. The lack of any improvement in the intrinsic noise of the step-edge SQUIDs over the bicrystals, is most likely associated with the larger spread observed in the junction parameters - the better $I_C R_N$ products of the step-edge devices are generally offset by the increased likelihood of greater asymmetries in the parameters of the two junctions incorporated in the SQUID.

In contrast to the common misconception that step-edge devices are a poor alternative to bicrystal devices, the work described in this thesis clearly demonstrates that for single junctions and for SQUIDs no loss in performance need be expected.

7.2 Gradiometers

Chapter 5 described the performance of small SLGs, fabricated on $10 \times 10\text{mm}^2$ substrates, and larger SLGs fabricated on $30 \times 10\text{mm}^2$ substrates. The small SLGs exhibited gradient sensitivities comparable with the best reported for devices fabricated on $10 \times 10\text{mm}^2$ substrates. The best gradient sensitivity, measured with the device cooled in a shielded environment, was $308\text{fT/cm}\sqrt{\text{Hz}}$ with the device having a balance of 1/160. A better balance was achieved for another small SLG design, for which a value of 1/300 was measured. The small SLGs have suitable characteristics

for many applications. Examples discussed in Chapter 5 include their use in the Strathclyde NDE programme, and their use in the cryogenic current comparator developed at NPL.

The large area gradiometers were designed to offer the sensitivities required for the application of HTS SQUID sensors in biomagnetic measurements. The large area SLGs had a balance of 1/1000, with the best device having a gradient sensitivity of $50\text{fT/cm}\sqrt{\text{Hz}}$ - better than any gradient sensitivity reported in the literature for a SLG. The large area SLGs were used to record MCGs from healthy adult volunteers, both inside the aluminium screened room at the Wellcome Biomagnetism Unit and completely unshielded with the devices operated in the open laboratory.

A problem inherent in all conventional SQUID SLGs is the increase in flux noise, and corresponding decrease in gradient sensitivity, when the device is cooled in an unshielded environment - the most significant source of this increase being direct pick-up of environmental noise and the Earth's field by the SQUID in the centre of the device. A novel type of SQUID, the G-SQUID, was introduced in Chapter 6. The G-SQUID was designed such that it has no intrinsic uniform field response from the SQUID. Autonomous G-SQUIDs were tested and found to have a small uniform field response (more than two orders of magnitude smaller than one would expect for a conventional narrow-linewidth SQUID of similar inductance). This small uniform field response is believed to originate from slight imperfections in the device fabrication resulting in the two loops of the G-SQUID having slightly different areas. Due to their small parasitic effective areas, the incorporation of a G-SQUID in an SLG greatly improves the device balance. The best design of G-SQUID SLG had an intrinsic device balance of 1/5000, more than an order of magnitude better than the balances reported for similar SLGs fabricated on $10 \times 10\text{mm}^2$ substrates incorporating conventional SQUIDs. Given their small parasitic effective areas, with the G-SQUID devices there was no observable increase in the flux noise when the device was cooled in an unshielded environment - *i.e.* any direct pick-up by the device is negligible. This work demonstrated that the SQUID in the centre of a

SLG no longer need limit the balance of the device.

7.3 Future Work

In the short term, there are two areas directly associated with the work described in this thesis which require attention. The first is the relatively poor flux noise observed for the large area gradiometer devices described in Chapter 5. Several bicrystal devices were fabricated, all of which generally showed a relatively poor intrinsic flux noise. This is perhaps a consequence of there being greater stress on the bicrystal grain boundary during film growth on the large area substrate. It was hoped that with step-edges this would not be the case and there would be improvements in the device flux noise. Only one step-edge device was fabricated, and this too exhibited a poor flux noise. It was not clear whether this was related to the problems with the fabrication of the step-edge on a large area substrate or perhaps just due to problems that occurred with this one sample. The problem of high flux noise could also perhaps be related to a high intrinsic flux noise in the large area film itself. Further investigation of the film growth process on large area substrates is required.

The second issue which requires further attention is the high intrinsic flux noise measured in the G-SQUID devices. This is most likely related to degradation of the thin film during the many photolithography and ion milling procedures required. Further optimisation of the fabrication procedure, to prevent any overmilling of the samples and reduce the time the sample is in contact with water may reduce damage to the film and result in improvements in the device flux noise. To further improve the gradient sensitivity of the G-SQUID devices, a G-SQUID incorporated in a large area SLG should be fabricated. These devices have already been designed with the second generation G-SQUID from Chapter 6 incorporated in a third generation large area SLG design from Chapter 5. Given the flux noise of the second generation G-SQUIDs (the best measured was $50\mu\Phi_0/\sqrt{\text{Hz}}$), their mutual inductance L_M and the

performance of the large area conventional SQUID SLG, one could perhaps expect to achieve a shielded/unshielded gradient sensitivity of approximately $150\text{fT/cm}\sqrt{\text{Hz}}$ for the large area G-SQUID SLG. Should improvements in the fabrication procedure result in G-SQUIDs with a lower flux noise (*e.g.* device's routinely exhibiting a flux noise close to the best measured for a G-SQUID of $10\mu\Phi_0/\sqrt{\text{Hz}}$) then one could hope to perhaps achieve shielded/unshielded gradient sensitivities as good as $15\text{fT/cm}\sqrt{\text{Hz}}$.

A more long term project to using the sensors described in this thesis, is to form a software gradiometer from two or more separate devices. Software gradiometry has emerged as a particularly promising technique avoiding many of the problems associated with the electronic subtraction of signals. The signals from two or more separate devices are post-processed to obtain gradiometric signals and/or remove environmental noise. To improve the signal-to-noise ratio for biomagnetism applications, a possible scheme being developed by E.J. Romans and P. Brousov, is to use two large area gradiometers (or possibly two large area G-SQUID gradiometers) to form a second order gradiometer to detect the signal to be measured. In conjunction with the gradiometer chips, three separate magnetometers measure the environmental noise along each axis of the system. Using software processing and filtering techniques, the signals from the two gradiometers are combined to give the second order response with the environmental noise measured by the magnetometers subtracted from the signals measured by the gradiometers. With this system it is hoped that high quality MCGs, with signal-to-noise ratios sufficient for clinical applications, can be recorded in a completely unshielded environment.

Appendix

List of Publications

C.M. Pegrum, A. Eulenburg, E.J. Romans, C. Carr, A.J. Millar and G.B. Donaldson, "*High-temeperature single-layer SQUID gradiometers with long baseline and parasitic effective area compensation*", Supercond. Sci. Technol. 12, p.766 (1999).

A. Eulenburg, E.J. Romans, C. Carr, A.J. Millar, G.B. Donaldson, and C.M. Pegrum, "*Highly balanced long-baseline single-layer high-T_c superconducting quantum interference device gradiometer*", Appl. Phys. Lett. 75, p.2301 (1999).

C. Carr, E.J. Romans, A. Eulenburg, A.J. Millar, G.B. Donaldson and C.M. Pegrum, "*A second-order HTS electronic gradiometer for nondestructive evaluation with room-temperature differencing*", Inst. Phys. Conf. Ser. No 167, vol. II, p.453 (1999).

A. Eulenburg, C. Carr, A.J. Millar, E.J. Romans, G.B. Donaldson and C.M. Pegrum, "*Single layer high-T_c SQUID gradiometer with large baseline*", Inst. Phys. Conf. Ser. No 167, vol. II, p.569 (1999).

A.J. Millar, E.J. Romans, C. Carr, A. Eulenburg, G.B. Donaldson, P. Maas and C.M. Pegrum, " *High-T_c gradiometric superconducting quantum interference device and its incorporation into a single-layer gradiometer*", Appl. Phys. Lett. 76, p.2445 (2000).

E.J. Romans, A. Eulenburg, C. Carr, A.J. Millar, G.B. Donaldson amd C.M. Pegrum, " *NBCO Bicrystal Josephson Junctions and SQUIDs operating at 77K*", IEEE Tran. Appl. Supercond. 11, p.1347 (2000).

A.J. Millar, E.J. Romans, C. Carr, A. Eulenburg, G.B. DOnaldson and C.M. Pegrum, "*Step-edge Josephson Junctions and their use in HTS Single-Layer Gradiometers*", IEEE Tran. Appl. Supercond. 11, p.1351 (2000).

C. Carr, E.J. Romans, A.J. Millar, A. Eulenburg, G.B. Donaldson and C. M. Pegrum, "*First-order high-T_c single-layer gradiometers: parasitic effective area compensation and system balance*", IEEE Tran. Appl. Supercond. 11, p.1367 (2000).

E.J. Romans, A.J. Millar, C. Carr, R. Palai and C.M. Pegrum, "*High-T_c single layer gradiometers: device optimisation for full portability in an unshielded environment*", accepted for publication in Physica C.